KATHOLIEKE UNIVERSITEIT
LEUVEN

Faculteit Wetenschappen

Departement Natuurkunde & Sterrenkunde
Celestijnenlaan 200 D
3001 Leuven (Heverlee)

Magneto-optical properties of semiconductor nanostructures

Promotoren:

Prof. Dr. Victor Moshchalkov
Prof. Dr. Manus Hayne

Proefschrift voorgedragen tot het behalen van de graad van doctor in de Wetenschappen, 2009

Door:

Thomas Nuytten

ISBN 978-90-8649-234-3
D/2009/10.705/12

A full color version of this thesis can be found on
http://www.kuleuven.ac.be/doctoraatsverdediging/cm/3E05/3E050582.htm

KATHOLIEKE UNIVERSITEIT LEUVEN

Faculteit Wetenschappen

Departement Natuurkunde & Sterrenkunde
Celestijnenlaan 200 D
3001 Leuven (Heverlee)

Magneto-optical properties of semiconductor nanostructures

Promotoren:
Prof. Dr. V. V. Moshchalkov
Dr. M. Hayne

Proefschrift ingediend tot
het behalen van de graad van
doctor in de wetenschappen
Door:

Thomas Nuytten

2009

Dankwoord

Eindelijk is het dan zover. Na ontelbare keren tevergeefs uitgelegd te hebben wat ik nu precies doe aan de KULeuven, ligt hier het tastbare resultaat van vier jaar werk. Gedurende die vier jaar zijn heel wat mensen, op professioneel of persoonlijk vlak, belangrijk geweest voor mij, en dit is dan ook het uitgelezen moment om hen te bedanken.

Eerst en vooral wil ik mijn beide promotoren bedanken: Prof. Dr. Victor Moshchalkov die mij de kans geboden heeft om te doctoreren en om deel uit te maken van zijn onderzoeksgroep. Dr. Manus Hayne, for his invaluable tuition and patient guidance. Even after moving from the KULeuven to Lancaster University, his great enthusiasm and clever understanding of the physics of semiconductors have meant a massive contribution to this work.

I would like to thank the members of the jury for the evaluation of my work and the interesting discussions during the preliminary defence: prof. Peter Lievens, prof. Johan Vanacken, prof. Koen Clays, prof. Mario Capizzi and prof. Valeri Afanasiev.

De boeiende sfeer op de werkvloer is te danken aan de vele collega's die komen en gaan, maar allen bijdragen tot een prettige omgeving: bedankt Bhavtosh Bansal, Stefanie Godefroo, Nele Schildermans, Jochen

Maes, Damien Saurel, en alle anderen. Bedankt ook aan de techniekers, en in het bijzonder P. Mispelter voor de onmisbare hulp bij technische problemen.

Ik ben dank verschuldigd aan de wetenschappers die mij hun samples ter beschikking stelden en hebben bijgedragen tot de wetenschappelijke uiteenzettingen in dit werk: L. Seravalli en S. Franchi (Parma, Italië), M. Henini (Nottingham, UK) en M. Hopkinson en H. Y. Liu (Sheffield, UK). Verder wil ik ook graag de vele wetenschappers bedanken die door de interessante discussies een beter inzicht mogelijk maakten: D. Mowbray, T. Badcock, M. Goiran, J. Leotin, Q. D. Zhuang, E. Nabavi, M. Ahmad Kamarudin en vele anderen.

Vervolgens wil ik ook alle mensen bedanken zonder wie het maar een saaie boel zou zijn geweest gedurende die vier jaar: de vrienden uit *de thuisbasis*: Matthias, Bruno, Frédéric en alle anderen voor de avonturen in Kuurne en Biscarrosse. Alle vrienden uit de achtjarige studententijd, en Lore in het bijzonder, die het hier in Leuven zo plezant maken. Peter, Kristof en Wouter voor de onnozelheden in *the crib* en daarbuiten. Bedankt voor de steun, het enthousiasme en vooral de vele heerlijke momenten die voor de nodige afleiding zorgden.

Als laatste wil ik ook mijn familie bedanken voor de steun tijdens de voorbije vier jaar. Hierbij denk ik in het bijzonder aan Mama en Papa, die me niet alleen de kans gegeven hebben om te studeren en te doctoreren, maar ook altijd klaarstaan in mooie en minder mooie tijden. Niets was mogelijk zonder jullie, en daar ben ik ontzettend dankbaar voor.

Bedankt voor alles!!

Thomas Nuytten
Maart 2009

Contents

Introduction

With the ever growing computerisation of our everyday life, the need to transport large amounts of information in a fast and reliable manner has never been so important. In order to guarantee an efficient transmission of data via optical fibres, light sources that emit in the optical windows with the lowest attenuation, namely around 1.3 and 1.55 μm, are required (Figure 1).

A sound candidate for this long wavelength emission are InGaAsP/InP heterostructures, and lasers based on this system are currently most widely used in long distance fibre optical communication systems. However, the small conduction band offset between the active and surrounding material in these structures ($\Delta E=0.4\Delta E_g$ with ΔE_g the band-gap energy) leads to a very strong temperature dependence of the threshold current density[1] [2], the thermal and electrical conductivities are too low and an insufficient refractive index contrast[2] between the constituting layers makes the fabrication of high quality lasers based on this system very challenging. Additionally, the need for low cost manufacturing favors the use of GaAs substrates over InP [3].

Two valuable approaches for reaching long wavelength emission with

[1] The threshold current density is the amount of current that needs to be injected in the device. Below this limit, internal losses are too high to produce sufficient gain for lasing to occur.

[2] A sufficient refractive index contrast between the constituting layers is necessary to confine the generated laser light to within the lasing cavity.

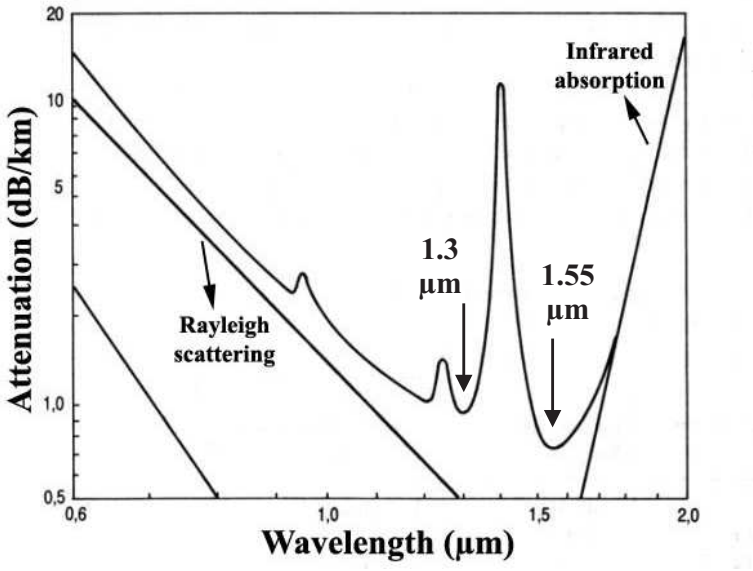

Figure 1: Attenuation in optical fibres as a function of wavelength of the light source, showing the local minima around 1.3 and 1.55 μm as indicated by the arrows. The large extrinsic absorption around 1.4 μm is due to the fundamental absorption at 2.7 μm by Si-OH bonds in the fibre [1].

GaAs-based materials are (i) the incorporation of a small amount of N in the InGaAs system to form GaInNAs/GaAs quantum wells (QWs), and (ii) metamorphic growth of self-assembled InAs/GaAs quantum dot (QD) nanostructures. In the present work we will explore these two approaches. More precisely, the aim of this work is to investigate carrier distributions and exciton confinement in semiconductor nanostructures. Additionally, since thermal stability is extremely important for technological applications, a better understanding of the temperature-dependence of the exciton properties will be pursued.

The **first Chapter** will provide a description of the main technique that was used to study the excitonic properties in our semiconductor nanos-

tructures; magneto-photoluminescence (magneto-PL). This unique tool combines the investigation of the possible optical transitions with the ability to confine the charge carriers to within the nanostructure using strong magnetic fields. This combination allows for the determination of fundamental excitonic properties like the exciton wave-function extent and exciton effective mass. The influence of a magnetic field on the energy of an exciton will be discussed, and the excitonic model, used to analyse the magneto-PL data, will be described. Subsequently, the **second Chapter** is focused on the Pulsed Fields facility at the KULeuven, where the measurements were carried out. The magneto-PL equipment and new software to facilitate data analysis will be presented.

Although the influence of a magnetic field on the individual energy levels of a semiconductor material can be accurately understood, the application of a strong magnetic field can have interesting effects on the exciton confinement in semiconductor *nanostructures*. The **third Chapter** reports such behaviour, where the magnetic field actively assists in the confinement of charge carriers in InAs QDs. Additionally, a pronounced distinction between two temperature regimes will be discussed.

In the **fourth Chapter** the localisation effects that are present in dilute nitride QWs are studied in two different samples, one of which the optical and structural properties are expected to be rather poor, and another sample where the growth conditions have been optimised to improve its optical quality. All our results unambiguously confirm these expectations, and it is shown that temperature dependent magneto-PL can be used to estimate the scale of these optimisations, even to the extent of enabling a phenomenological description of the potential landscape in both samples.

The **fifth Chapter** deals with the excitonic properties of InAs QDs grown on metamorphic confining layers. In these strain-engineered structures, the composition and thickness of the confining layer are used as two degrees of freedom to tune the room-temperature emission. We show that the reduction in QD strain and band discontinuities to reach long-wavelength emission is initially accompanied by an increase in importance of the lateral confinement, up to a point where the QD can no longer confine the carriers, and the exciton bursts out of its quantum box.

In a final **sixth Chapter**, the fabrication of a new system for Optical Detected Magnetic Resonance will be presented. The implementation of this new equipment provides a unique tool to study magnetic resonance in pulsed fields. Under infrared laser excitation, certain energy levels become resonant at a specific strength of the applied magnetic field. Simultaneous PL measurements will show characteristic changes and thus allow identification of the resonant energy levels.

Finally, we will summarise the results and formulate general concluding remarks.

Chapter 1

Magneto-photoluminescence of semiconductor nanostructures

In this first Chapter, we will outline the theoretical background required to understand the experiments in this work. This thesis is focused on the use of the photoluminescence (PL) technique in high magnetic fields, generated by either a pulsed magnet (up to 50 T) or a superconducting DC magnet (up to 12 T). We will give an introduction to PL of semiconductor nanostructures, describe the influence of a magnetic field on the energy levels of the exciton, and discuss the excitonic model that is applied to investigate the electronic properties of the studied material.

1.1 Low dimensional semiconductor structures

1.1.1 Reduced dimensionality

A perfect three-dimensional semiconductor crystal consists of a periodic arrangement of ions with the electrons orbiting around them. The en-

ergy levels of such a crystal are grouped into two continuous energy bands, the conduction and valence band, that are separated by a band-gap with energy E_g. Correspondingly, the density of states is continuous and has a square-root dependence on energy (Figure 1.1). An electron in the crystal can be described as a free particle with effective mass m_e^* and with energy

$$E_{3D} = \frac{\hbar^2}{2m_e^*}(k_x^2 + k_y^2 + k_z^2) \tag{1.1}$$

where $\hbar$ is the reduced Planck constant and k_x, k_y and k_z are the charge wavenumbers. When the motion of the carriers is spatially limited to a length l_z of the order of the de Broglie wavelength or smaller in one dimension, for instance by growing a thin layer of a low band-gap semiconductor between higher band-gap material, the energy in that dimension (e.g. the growth direction, z) has to be described quantum-mechanically. The resulting energy of an electron in a so-called *quantum well* (QW) is then given by:

$$E_{2D} = \frac{\hbar^2}{2m_e^*}(k_x^2 + k_y^2) + E_{n,z} \tag{1.2}$$

with $E_{n,z}$ the energy of sub-band n:

$$E_{n,z} = \frac{\hbar^2}{2m_e^*}(\frac{n\pi}{l_z})^2. \tag{1.3}$$

The next step in complexity is to limit another dimension so that free motion is possible along only one direction. The same approach of adding the energies of the three dimensions together following the superposition principle gives the energy of an electron in a *quantum wire*:

$$E_{1D} = \frac{\hbar^2 k_x^2}{2m_e^*} + E_{m,y} + E_{n,z} \tag{1.4}$$

with $E_{m,y}$ the energy of sub-band m for the y-direction. Finally, the motion of carriers can be limited in all three dimensions, yielding a

completely discrete energy spectrum for a *quantum dot* (QD):

$$E_{0D} = E_{l,x} + E_{m,y} + E_{n,z}, \tag{1.5}$$

again with $E_{l,x}$ the energy of the l sub-band for the x-direction.

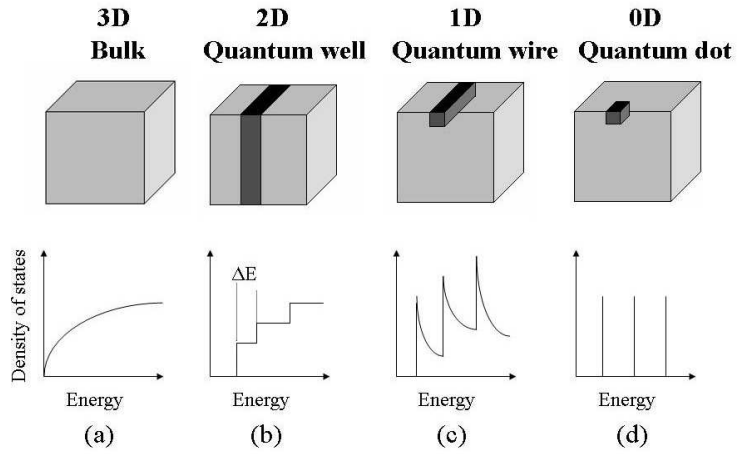

Figure 1.1: Density of states for ideal structures when reducing the dimensionality: (a) bulk, (b) a quantum well, (c) a quantum wire and (d) a quantum dot. The upper schematics represent the structures in real space.

As a consequence of the discretisation of the energy, the density of states profile evolves from a square-root dependence for bulk material to distinct plateaus (QW), peak functions with a high energy tail (quantum wire) and eventually a collection of delta functions whose energies depend on the physical size of the quantum dot (Figure 1.1). For an ideal ensemble of dots uniform in size, all the electrons (and holes) in the ground state have the same energy, and thermal broadening is impossible. Therefore, quantum dots are often referred to as *artificial atoms* [4], and they are an excellent candidate for gain material in opto-electronic devices such as lasers and detectors.

1.1.2 Self-assembled growth

Molecular Beam Epitaxy

The applicability of nano-engineered semiconductor structures is directly related to the ability of growing such structures in a controlled way. Much of the success of the research on low-dimensional semiconductors is due to the breakthrough of a very versatile technique for growing thin epitaxial layers called *Molecular Beam Epitaxy* (MBE) [5]. Being realised in an ultrahigh vacuum (UHV) environment (10^{-7} Pa and less), MBE has the advantage of allowing *in situ* diagnostic techniques for controlling the growth process such as Reflection High Energy Electron Diffraction (RHEED)(Figure 1.2). Here, a RHEED-gun emits high energy electrons ($\sim$10 keV) that arrive at the sample at a very small incident angle, and are reflected to eventually hit a phosphor screen. From the RHEED image, information of the sample morphology during the growth process can be obtained. Additionally, the conditions of MBE growth are much more flexible compared to other techniques such as *e.g. Metalorganic Vapour Phase Epitaxy*. Hence, it is a better research tool since the conditions under which the growth takes place can be changed much more easily.

A molecular or atomic beam of the constituent elements is obtained by heating the source material in a so-called Knudsen-cell with a small opening. Each of the (typically four) effusion cells contains a single and pure material such as In, As, Ga, P, Si or Be, and the flux from each cell is controlled by its temperature. By selectively opening and closing the shutters, semiconductor heterostructures with sharp interfaces can be constructed. Because of the UHV growth conditions, the mean free path of the molecules is larger than the physical dimensions of the deposition chamber, enabling ballistic transport toward the substrate. The temperature of the substrate can be accurately controlled, and rotation at a fixed angular velocity enhances the thickness and composition homogeneity. Growth of patterned structures can be achieved through the use of pre-patterned substrates, or by disabling the rotation of the

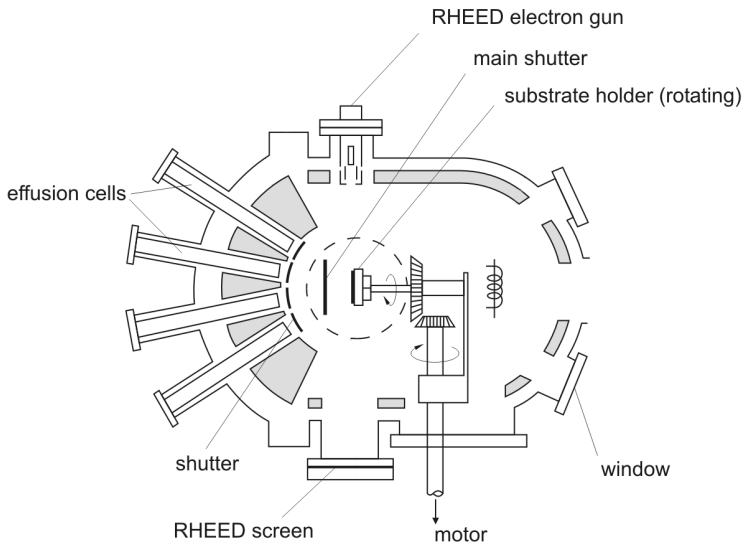

Figure 1.2: Schematic representation of a typical MBE deposition chamber. Different Knudsen cells for effusion of the different constituents are present, each with a separate shutter. A motor-driven rotating substrate holder, a RHEED setup, a main shutter and an inspection window are also indicated.

substrate, creating modulations in composition and thickness across the sample.

Self-assembly of semiconductor nanostructures

For device applications, a large number of defect-free and densely-packed nanostructures with a good size homogeneity is needed. The self-assembly process, that is based on strain relaxation during heteroepitaxial growth of lattice mismatched systems, provides an easy way to construct such structures. Depending on the forces between the constituting elements and the difference in lattice parameter, there are three different growth modes which can occur during the epitaxial growth of a material A onto a substrate B:

- Two-dimensional or Frank van der Merwe growth

Here, material A and substrate B are closely lattice-matched, and the atoms A aggregate to form expanding monolayer islands, eventually forming the first monolayer.

- Three-dimensional or Volmer-Weber growth

  When the interface energies between A and B are sufficiently large, deposition of material A onto substrate B results in the immediate formation of three dimensional islands.

- Stranski-Krastanow growth mode

  With only a small lattice mismatch between A and B, an initial two-dimensional wetting layer is formed, on top of which three-dimensional islands are formed that relieve the accumulated strain during epitaxial growth to a considerable amount (∼50%).

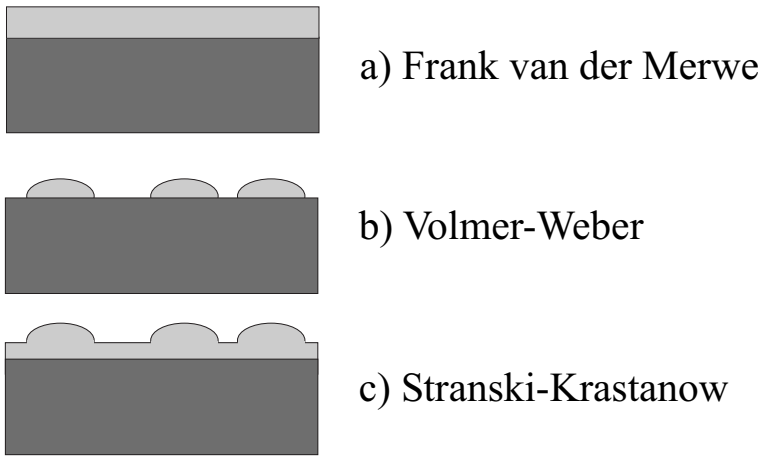

Figure 1.3: The three different modes for epitaxial growth: (a) Frank van der Merwe, (b) Volmer-Weber and (c) Stranski-Krastanow growth mode.

The quantum dot (QD) structures studied in this work are fabricated following the Stranski-Krastanow growth mode, which produces dislocation-free (for small amounts of deposition) dots that are relatively uniform in size. A common technique for maintaining the position of

the dots is to overgrow the QDs with additional substrate material. Although this so-called capping layer preserves the quality of the dots, it is also known to modify the size and shape of the QD structures, as was evidenced by microscopy studies on capped and uncapped dots [6].

1.2 Photoluminescence of semiconductors

PL is one of the most common techniques to determine the possible optical transitions in the band structure of semiconductors. It is based on the collection of the optical response of a material after optical excitation. In the case where the studied material is a *direct* band-gap semiconductor, *i.e.* the conduction band minimum and valence band maximum appear at the same point in k-space; the Γ-point, the PL process is relatively straightforward. For the purpose of this thesis, we will only consider this type of process, since all of the studied materials are direct band-gap semiconductors, and hence no additional momentum needs to be carried away.

The first step in the PL process is the excitation of the semiconductor material via laser light of frequency ν, such that the incident photons carry an energy $h\nu$ (Figure 1.4). When this energy is larger than the band-gap energy of the material, an electron from the valence band can be excited into the conduction band, leaving a vacancy in the valence band. Since the momentum of the photon is negligible, the excited electron has the same k-vector as before the excitation. After the excitation, both the electron and the hole will relax to their respective equilibrium positions through non-radiative phonon emission to account for the change in momentum and energy.

After relaxation, the electron sits at the minimum of the conduction band, while the hole is at the maximum of the valence band. The electron and hole are free and can move independently through the semiconductor, but their Coulomb interaction can also result in the formation of a quasi-bound particle, the *exciton*. The energy levels of an exciton are similar to those of a hydrogen atom and are formed below the bottom

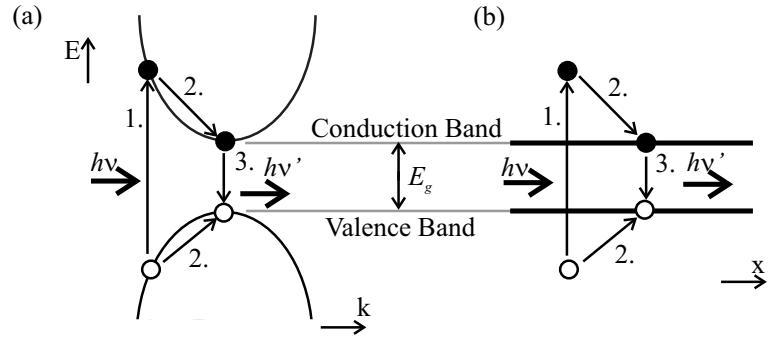

Figure 1.4: The three steps in the PL process in (a) momentum space and (b) real space: 1. An electron is excited toward the conduction band via an incident photon, leaving a hole in the valence band. 2. Both the electron and the hole relax to their position of minimal energy through phonon processes. 3. The electron and hole recombine, emitting a photon that can be detected.

of the conduction band, however with a dispersion that is different from that of the conduction band.

The energy levels of the exciton can be written as the sum of the electron and hole energies, E_e and E_h respectively, minus the binding energy:

$$E_n = E_e + E_h - \frac{\mu Ry}{\varepsilon^2 m_0} \cdot \frac{1}{n^2} \tag{1.6}$$

where $Ry = 13.6$ eV is the Rydberg energy, μ is the exciton effective mass relative to the electron rest mass m_0, ε is the dielectric constant of the semiconductor material in which the exciton is located and n is an integer representing the number of the energy level.

Once created, a non-radiative decoupling of the exciton may occur, leaving the electron and hole free to move through the lattice independently. More interestingly however, the electron can recombine with the hole, releasing a photon of energy $h\nu'$ (Figure 1.4) that is dependent on the band-gap energy, the band structure, the exciton binding energy, the applied fields, *etc.* Detection and analysis of this emitted light is an important source of information on the optical properties of the studied

material, and is the aim of the PL technique.

1.3 Influence of a magnetic field

Although an exciton is essentially a neutral particle and a magnetic field will have no influence on the motion of the centre of mass of a bound electron-hole pair, the wave-function of the exciton is deformed due to the Lorentz-forces acting on the charges it is built up of. As a result, the energy levels of the exciton will be altered, but depending on the strength of the applied field, a distinction between a low field and a high field regime can be made.

1.3.1 Fock-Darwin Model

A number of models have been used in the past to describe the magnetic field dependence of the PL of semiconductor nanostructures, the first of which is the Fock-Darwin model, which was developed independently by Fock [7] and Darwin [8]. This model essentially describes the energy levels of an electron in a two-dimensional harmonic potential of energy $\hbar\omega_c$ with a magnetic field applied perpendicular to the system (ω_c is the cyclotron frequency). This treatment provides a decent approximation of the energy states in a semiconductor nanostructure under the influence of a magnetic field, as is extensively discussed by *e.g.* Raymond and co-workers [9] for InGaAs/GaAs QDs.

1.3.2 Excitonic models

An alternative approach treats the system from an excitonic point of view and hence does not neglect the Coulomb interaction between the electron and the hole, which the Fock-Darwin analysis does not implicitly include. Such a model divides the effect of a magnetic field B on an exciton into a low and high field regime, and a useful parameter to distinguish between the two regimes is the relation between the magnetic

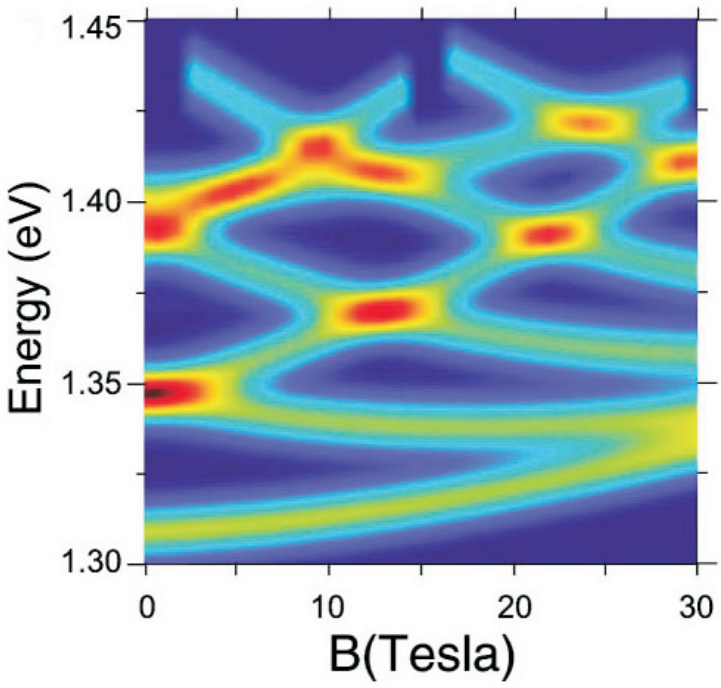

Figure 1.5: Calculation of the excitonic states in an $In_xGa_{1-x}As$ QD using an 8-band k.p model. Regions with a high (low) density of states are indicated by red (blue) colour. The Fock-Darwin spectrum, with the lifting of the energy of the lowest s-shell electron-hole pair as we observe it in our magneto-PL studies (see *e.g.* Figure 2.8), is well reproduced [9].

length $l_B = \sqrt{\frac{\hbar}{eB}}$ and the exciton wave-function extent at zero magnetic field $\langle\rho^2\rangle^{\frac{1}{2}}$.

Low field regime At low magnetic fields, where the influence of B is smaller than the influences from spatial limitations due to quantum confinement or Coulomb attraction ($\langle\rho^2\rangle^{\frac{1}{2}} << l_B$), the magnetic field can be treated as a small perturbation, and a diamagnetic shift of the

exciton energy levels occurs [10, 11] (see Figure 1.5):

$$\Delta E = \frac{e^2\langle\rho^2\rangle}{8\mu}B^2 \tag{1.7}$$

where e is the charge of the electron.

High field regime In the high field regime, however, the magnetic confinement dominates the spatial confinement of the excitons ($\langle\rho^2\rangle^{\frac{1}{2}} >> l_B$), and we have a situation equivalent to having "free" electrons and holes recombining from their respective Landau levels [12], such that the energy levels of the exciton are quantised according to

$$E_n = (n + \frac{1}{2})\hbar\omega_c \qquad with \qquad \omega_c = \frac{eB}{\mu} \tag{1.8}$$

Hence, the PL energy shift is linear with field and is no longer dependent on the exciton radius. When assuming that only the ground state (n=0) has to be taken into account, this gives for ΔE:

$$\Delta E = \frac{e\hbar}{2\mu}B \tag{1.9}$$

In between these two limits exists an intermediate regime, and in an effort to interpolate between the two regimes, Janssens and co-workers [13] constructed an empirical relation that is in excellent agreement with their numerical calculations for the field dependence of the exciton energy in a quantum disk:

$$\Delta E = \frac{\beta B^2}{1 + \alpha B} \tag{1.10}$$

where α and β are fitting parameters, that can be determined bearing in mind that Equation 1.10 must reduce to (1.7) and (1.9) in the low and high field limit, respectively, yielding

$$\beta = \frac{e^2\langle\rho^2\rangle}{8\mu} \tag{1.11}$$

$$\frac{\beta}{\alpha} = \frac{\hbar e}{2\mu} \tag{1.12}$$

Although this function is valid for the entire field range, and it reduces to the expressions given above for the low and high field regime, respectively, it has no real physical basis. Therefore, Hayne and co-workers had previously [14,15] followed an approach that is different in the sense that rather than attempting to fit the entire field dependence into one single equation, it maintains the bipartite concept of a low and high field regime, but passes from one regime to the other without any discontinuity in the magnetic field dependence of the energy or its derivative. The transition between the two regimes occurs at a crossover field B_c, and the expressions for the high and low field regime are combined in a single field-dependent function, with five parameters;

$$E = a_1 + a_2 B^2 \qquad for \qquad B < B_c \tag{1.13a}$$

$$E = a_3 + a_4 B \qquad for \qquad B > B_c \tag{1.13b}$$

A relation between the parameters can be found by imposing the boundary condition that the both the field-dependent energy and its derivative must be continuous functions at the crossover field B_c:

$$a_1 + a_2 B_c^2 = a_3 + a_4 B_c \tag{1.14}$$

$$2a_2 B_c = a_4 \tag{1.15}$$

and so

$$a_1 - a_2 B_c^2 = a_3 \tag{1.16}$$

giving for Equation 1.13b:

$$E = a_1 - a_2 B_c^2 + 2a_2 B_c B \qquad for \qquad B > B_c \tag{1.17}$$

A comparison between Equations 1.13a and 1.17 and the expressions for

the high and low field regime 1.9 and 1.7, gives:

$$a_2 = \frac{e^2\langle\rho^2\rangle}{8\mu} \qquad and \qquad B_c = \frac{2\hbar}{e\langle\rho^2\rangle} \tag{1.18}$$

which finally gives for the field-dependence of the centre of mass energy:

$$E = E_0 + \frac{e^2\langle\rho^2\rangle}{8\mu}B^2 \qquad for \qquad B < \frac{2\hbar}{e\langle\rho^2\rangle} \tag{1.19a}$$

$$E = E_0 - \frac{\hbar^2}{2\mu\langle\rho^2\rangle} + \frac{e\hbar}{2\mu}B \qquad for \qquad B > \frac{2\hbar}{e\langle\rho^2\rangle} \tag{1.19b}$$

leaving only three parameters; the zero-field PL energy E_0, the exciton wave-function extent $\langle\rho^2\rangle^{\frac{1}{2}}$ and the exciton effective mass μ. The exciton binding energy is given by $\frac{\hbar^2}{2\mu\langle\rho^2\rangle}$ and is the second term on the right of Equation 1.19b.

There are a number of arguments in favour of choosing this excitonic model to discuss and analyse our results. For instance, it has the practical advantage that it enables to directly retrieve the essential parameters that govern the opto-electronic behaviour of a semiconductor nanostructure system and it has a correct and accurate physical basis. The excitonic model is a natural choice for the interpretation of PL experiments in low-dimensional structures, since it involves the recombination of an exciton (quasi-bound state). Additionally, it is independent of the dimensionality of the problem, and thus its applicability is not limited to quantum dots. Hence, we have chosen this model to analyse the magneto-PL of our semiconductor nanostructures. Moreover, it is worth mentioning that both the Fock-Darwin model and the excitonic models are equivalent in the low and high field limits.

Chapter 2

Pulsed fields facility

As was pointed out in the previous Chapter, useful information on the confinement of carriers and excitonic properties can be extracted from field-dependent measurements of the PL energy. When studying semiconductor nanostructures, which are a few nanometers in size, a sufficiently large magnetic field is needed to observe both field regimes discussed above (to achieve a magnetic length of 5 nm, a field of 26 T is required). Although *hybrid* magnets, consisting of a combination of a superconducting and a resistive coil, reaching 45 T do exist (NHMFL, Talahassee), they are extremely power consuming and require a sophisticated cooling system. Pulsed fields however provide non-destructive and power-efficient access to these high fields, and most of the experiments in this work have been carried out at the KULeuven pulsed field facility, where fields of up to 50 T are readily available [16]. Although such high fields provide a unique tool for different studies, the short pulse duration of about 20 ms limits their applicability. For less optically active samples, where longer integration times are necessary, a 12 T superconducting coil can be used.

2.1 The capacitor bank

The high currents needed for the creation of strong magnetic fields are achieved by the release of a large amount of energy stored in a home-built oil-filled capacitor bank. It allows reversing of the polarity, and is equipped with a mechanical switch and an optically triggered thyristor discharge switch (see (7) and (8) in Figure 2.1) to discharge the bank. A pneumatic switching system allows up to 4 different coils to be connected to the bank (10), which enables the simultaneous running of 4 different experiments. The maximum charge voltage is 5 kV, and the capacity can be modified up to 40 mF while the maximum energy of the bank is 600 kJ, and the system uses automatic inductance (L)/resistance (R) measurements for coil monitoring (9).

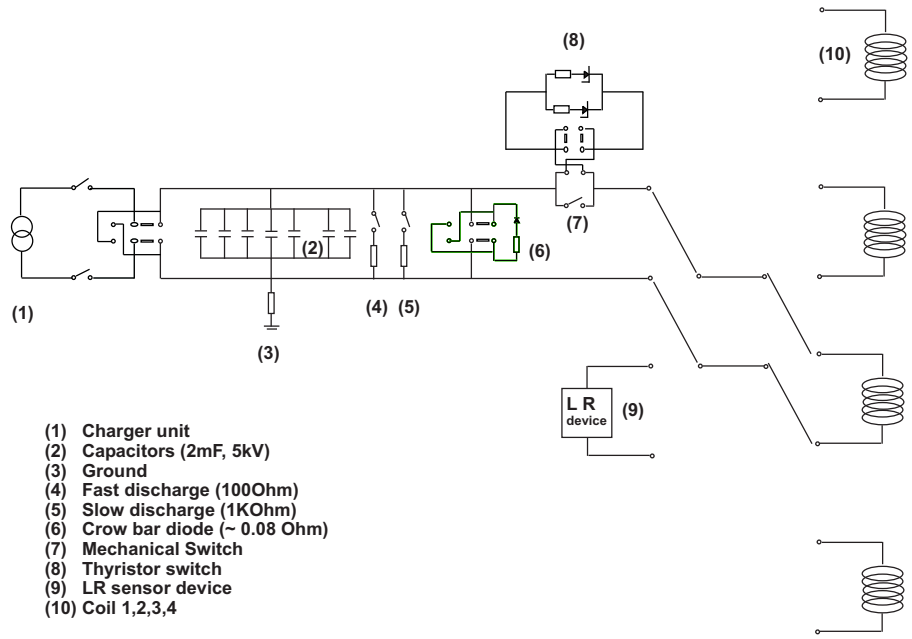

Figure 2.1: Scheme of the KULeuven 5 kV capacitor bank.

When performing a high field experiment, the charger unit (1) charges the capacitor bank (2) to a user-set voltage between 200 and 5000 V.

Once the required voltage is reached, the charger unit is disconnected and the bank can discharge into one of the connected coils (10). A collection of severe safety precautions are implemented. All measuring rooms are locked with door switches that dump the accumulated energy of the bank to the ground (3) through a 100 Ω resistor (4) as soon as a door is opened. Additionally, the central computer controls the interlocks and inhibits the charging of the bank until all safety conditions are met. For instance, the resistance and inductance of the connected magnet coil have to fall within a predetermined range to ensure that the coil has sufficiently cooled down after the preceding pulse, all doors to measuring rooms with connected coils need to be locked, and the condition of the hardware to operate the bank needs to be verified. A slow reduction of the charged voltage can be achieved through discharging over a 1 $k\Omega$ resistor (5).

Since the capacitor bank, the coil and the wiring form an RLC-circuit, an oscillation of the voltage over the bank would occur after discharging. To suppress these oscillations, a crowbar diode (6), which is a 0.08 Ω resistor in series with a diode, is added to the circuit. At the same time, it prevents high reverse voltages that could damage the unipolar capacitors. Another advantage of the crowbar diode is the reduction of the current dissipation in the coil, resulting in a shorter cool-down time and an extension of the field pulse by 50%. After each pulse, the coil is reconnected to the LR measuring device, which monitors the resistance and inductance until the coil has recovered for a next pulse. During this cool-down time ($\sim$ 45 minutes for a 50 T pulse), the bank can be switched to other coils, allowing multi-user operation.

2.2 Pulsed field coil design

During a 50 T-pulse, currents of up to 25 kA flow through the pulsed field coil, subjecting the wiring to very strong Lorentz forces. Additionally, a substantial amount of the injected energy is dissipated as heat into the coil. Therefore, the coils are designed to sustain a maximal mechanical

and thermal load, and are immersed in liquid nitrogen for efficient pre-pulse cooling. The coil itself consists of copper wires internally reinforced with glass-fibre composite layers, placed inside a stainless steel cylinder. Finally, a carbon-fibre composite layer is wound around the cylinder to provide additional durability.

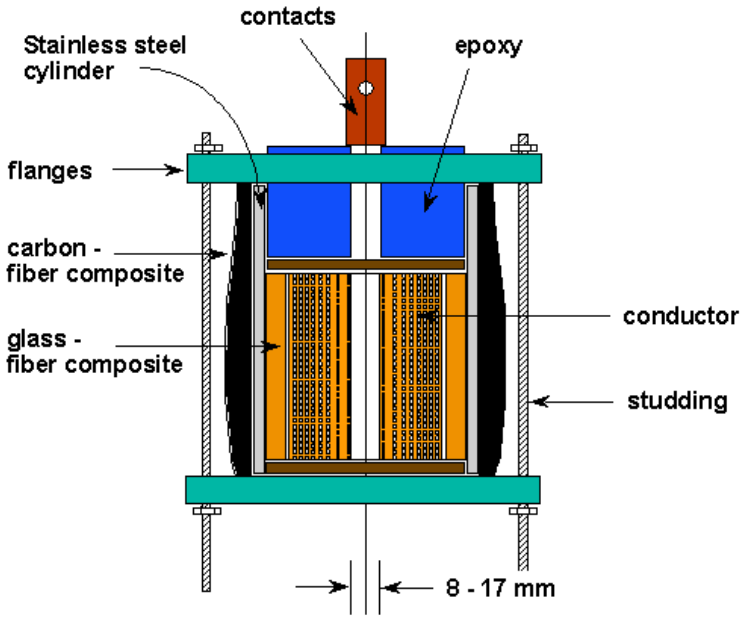

Figure 2.2: Vertical cross-section of a typical pulsed field coil with various reinforcements. The sample is placed in the bore of the pulsed field coil, which has a diameter of 8 to 17 mm, depending on the design.

Every coil to be used in the experimental setup is extensively tested in a special test-box. Coils that survive the test-cycle have proven to be usable for several years and deliver an average of ∼1000 high field shots.

2.3 Field detection and timing

When applying a DC field, the resulting magnetic field can easily be determined by measuring the current through the coil. Such an oper-

ation is impossible in pulsed fields due to the high current and short pulse duration, and an indirect measuring technique is used instead. The sample stick holding the optical fibres (see Section 2.5) and sample holder is equipped with a pick-up coil that detects the magnetic field as an induced voltage. The integration of this pick-up voltage over time gives the effective magnetic field through Faraday's law:

$$V_{pick-up}(t) = -S_{eff}\frac{dB(t)}{dt} \tag{2.1}$$

where S_{eff} is the area of the pick-up coil, typically a few hundreds of mm^2. A digital recorder measures the voltage over the pick-up coil and through numerical integration, the PC calculates the field profile, the result of which can be seen in Figure 2.3.

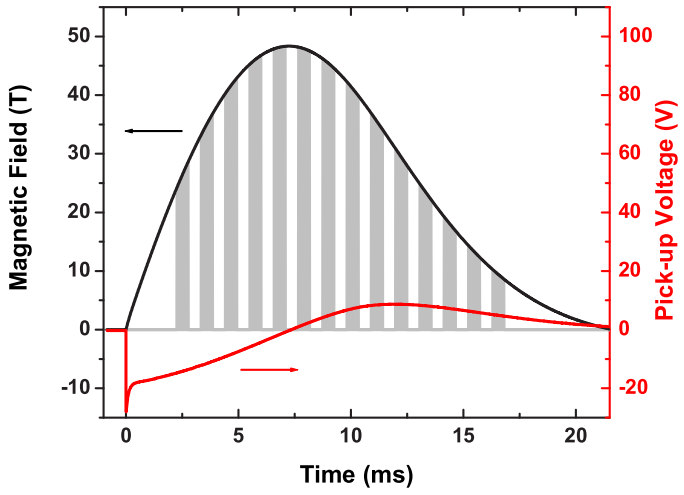

Figure 2.3: The magnetic field (left ordinate axis) and pick-up voltage (right ordinate axis) profile for a 50 T pulse. 14 shutters of 0.5 ms exposure time each are indicated by grey bars.

Depending on the PL brightness of the sample and the pulse duration of the specific coil, one exposure of 5 ms or up to more than 100 exposures

of integration times down to 200 μs can be used. Bearing in mind the long cool-down time of the pulsed field coils, a maximum of exposures within each pulse is pursued. However, to avoid artificial broadening of the PL signal, the shutter sequences are designed in such a way that the field variation within each acquisition never exceeds 5 %. If the variation of the magnetic field during the exposure is too large, the centre of mass and linewidth of the PL peak can no longer be determined in a reliable way.

Apart from enabling the calculation of the magnetic field during the pulse, the pick-up signal serves as a trigger for the optical section of the magneto-PL experiment. Once the current flows through the coil and the magnetic field is created, the digital recorder starts to record the pick-up signal, and an optical TTL signal is sent to the bank controller PC. Subsequently, the shutter sequence is sent from the PC to the detector. While the detector acquires the PL signal with the desired integration time and number of exposures, the actual shutter sequence as it is being recorded by the detector is sent back to the bank controller PC as a reference to the shutter sequence that was sent. As a result, both the desired exposure profile and the actual acquisition sequence as it was recorded by the detector are always available, together with the average magnetic field during each exposure as well as the corresponding field variations.

2.4 DC fields

When the PL signal for a certain sample is too weak to be studied in pulsed fields and longer integration times are needed requiring a continuous field, a DC set-up for fields of up to 12 T is available. An additional advantage of this technique is the absence of mechanical vibrations, and hence an increased uniformity in the actual area of the sample under excitation.

The field is created with a superconducting Nb_3Sn magnet from Magnex immersed in liquid helium (see Figure 2.4). Isolation from am-

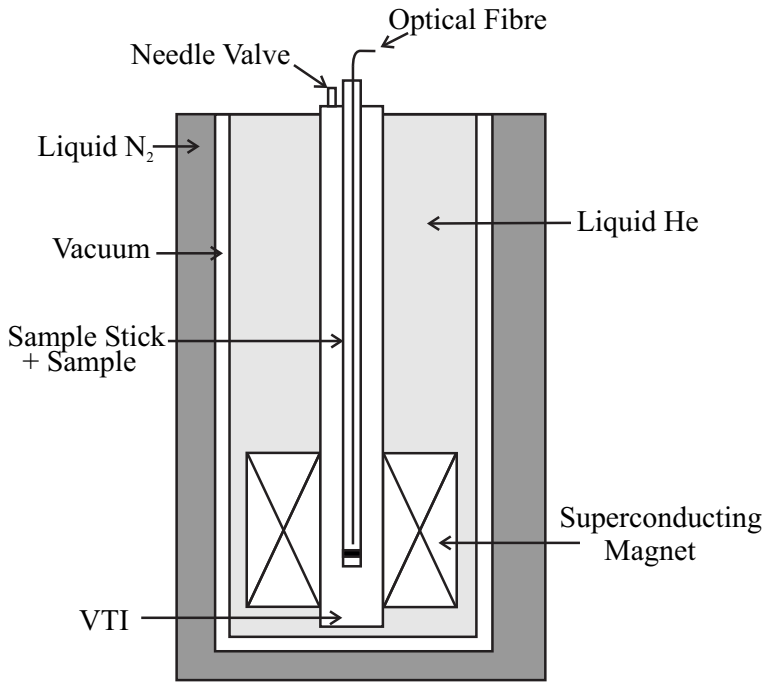

Figure 2.4: The 12 T DC field set-up.

bient temperatures is provided through a vacuum space and a liquid nitrogen mantle. The current through the magnet coil and the corresponding field in its bore are determined by measuring the voltage over a calibrated resistor in series with the coil. The sample is mounted on a brass sample holder that can be heated and is attached to a sample stick which also directs the excitation and collection fibres (see Section 2.5) toward the sample. The sample stick is inserted in a *Variable Temperature Insert* (VTI) that allows a variable helium gas flow from the magnet space through a sensitive needle valve to cool down. Additionally, a Lakeshore temperature controller monitors the temperature in the VTI and at the sample space, and adapts the current through the heating wire correspondingly. As a result, the sample temperature can be accurately set at any point between 4.2 and 300 K. Excitation and detection of the laser light and PL occurs in a similar way as in pulsed

field measurements, however, a precise timing arrangement is no longer necessary.

2.5 Photoluminescence set-up

At the core of the pulsed field facility is the bank controller PC (see Figure 2.5), which initiates the field pulse and optical detection of the PL. Depending on the desired experimental conditions, a helium *bath cryostat* or *flow cryostat* can be used. The former uses a bath of liquid helium to cool the sample, and allows temperatures between 2.2 and 4.2 K using a helium pump. The flow cryostat combines a heater and a helium gas flow to reach temperatures anywhere between 4.2 K and room temperature. The magnet coils under each cryostat are interchangeable and the connection between the magnet and the capacitor bank is made by a collection of heavy duty copper cables.

The separate optics room houses the excitation sources, spectrometers and detectors. Three different lasers for excitation are available, covering a large wavelength range:

- A high power solid state laser which uses neodymium yttrium vanadate (Nd:YVO_4) as gain medium, and is pumped by a 40 W fibre-coupled infrared laser diode bar. The Nd:YVO_4 lases at 1064 nm, and a lithium triborate doubling crystal produces the visible 532 nm. The *Millennia Vs J* from Spectra-Physics we have used produces powers up to 5 W continuous wavelength. However, the use of powers exceeding 1 W must be avoided because they produce too much heat upon scattering and would damage the optical fibres.

- A second diode-pumped frequency-doubled neodymium yttrium-aluminium garnet (Nd:YAG) solid state laser generating ∼100 mW of green light at 532 nm.

- An Ar-ion gas laser with a collection of lines from ultraviolet to green (351.1 to 514.5 nm). The maximum power varies between

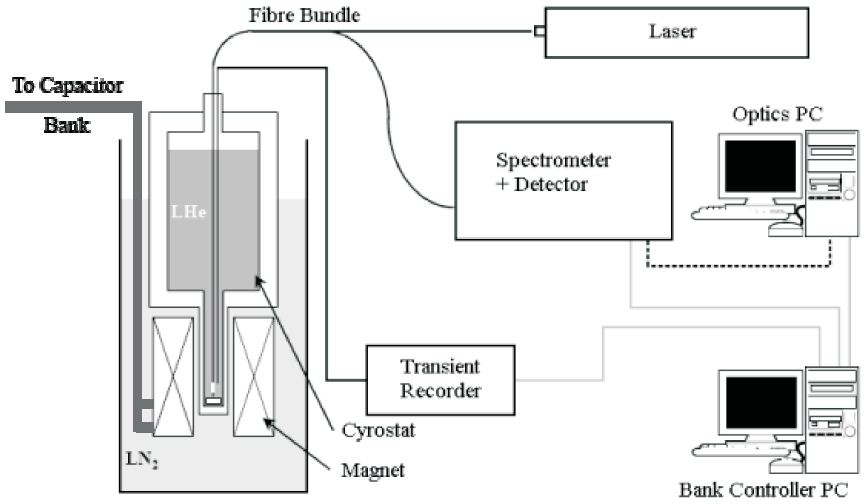

Figure 2.5: Schematic representation of the equipment and connections in the pulsed field facility, although the optical set-up, the cryostat and the bank controller pc are in three different rooms. A bath cryostat is shown in the drawing, and the full grey lines represent optical connections, while the dashed line is an electronic connection.

100 mW and 6 W depending on the desired wavelength. Some visible lines, such as at 488 nm, are available in single-line operation, while UV excitation can only occur through multi-line operation.

The excitation light from the lasers is transported to the sample in the cryostat via a 200 μm core high-OH multimode silica fibre, while the PL signal is collected with a 500 μm core low-OH fibre. Since the cryostat and detection equipment are in separate rooms, $\sim$25 m of optical fibre is needed to reach the sample. To calculate the excitation power density at the sample, one should bear in mind that a slight absorption of the laser light occurs in the silica fibres used in our set-up. The transmission for 532 nm laser light is 99.5 % per meter, which gives 88 % transmission over 25 m. To avoid re-collection of excitation light reflected off the sample surface, a special geometry for the fibres is used,

where the excitation fibre is aimed at the sample under a 15° angle with respect to the collection fibre, such that as little as possible reflection signal is collected in the collection fibre (see Figure 2.6).

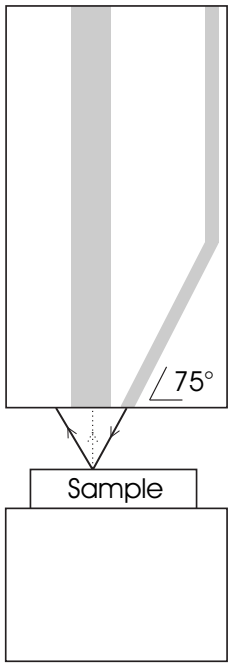

Figure 2.6: Special geometry of excitation fibre to avoid re-collection of excitation light (full line) reflected off the sample surface. The grey areas indicate the location of the fibres. The angle is exaggerated to clarify the effect.

After being collected, the PL signal is brought to an Acton SpectraPro-300i monochromator via the 500 μm collection fibre. The monochromator has a focal length of 300 mm and is equipped with three different gratings (300, 600 and 1200 grooves/mm). It achieves its maximal resolution of 0.1 nm at 435.8 nm and has micrometer adjustable slits that can be set at any width between 10 μm and 3 mm.

Since the samples in this study are designed for long-wavelength emission, near-infrared detection is needed to study the magneto-PL. The silicon used in *Charge Coupled Device* (CCD) cameras cannot pro-

vide photosensitivity beyond 1.1 μm, and therefore a different material is required to work in the near-infrared. The monochromator is connected with a Princeton Instruments OMA V InGaAs photodiode array detector. The detector is cooled with liquid nitrogen to decrease the number of dark counts, which is of particular interest for longer integration times. By cooling the detector, the dark charge is halved for every 10°C decrease in temperature, while the red edge for long wavelengths of the quantum efficiency curve moves by 0.8 nm/°C. As such, the detector can be used as a tunable filter to narrow the device's sensitivity, while screening out unwanted background.

It should be noted that for detection in the ultraviolet and visible range, a very sensitive *Electron Multiplying CCD* is also available, although we have not used it for our experiments, since all of the studied samples emit in the infrared.

2.6 Analysis of results

The detector records the PL signal by measuring the intensity at a specific wavelength, over the wavelength range that depends on the chosen grating. When multiple spectra are taken with each field pulse (See Section 2.3), the analysis of a data-set, which contains a number of field pulses at different strengths of the magnetic field, can become a very time-consuming procedure. In many cases however, the spectrum contains a single Gaussian-like peak and hence it is easy to write software to determine the centre of mass position following

$$E_{cm} = \frac{\int I(E)EdE}{\int I(E)dE} \tag{2.2}$$

Additionally, the new program determines the line-width of the peak as the full width at half maximum (FWHM), and calculates the magnetic field associated with each spectrum. A cut-off feature in percent or absolute intensity is available to account for unwanted background scatter.

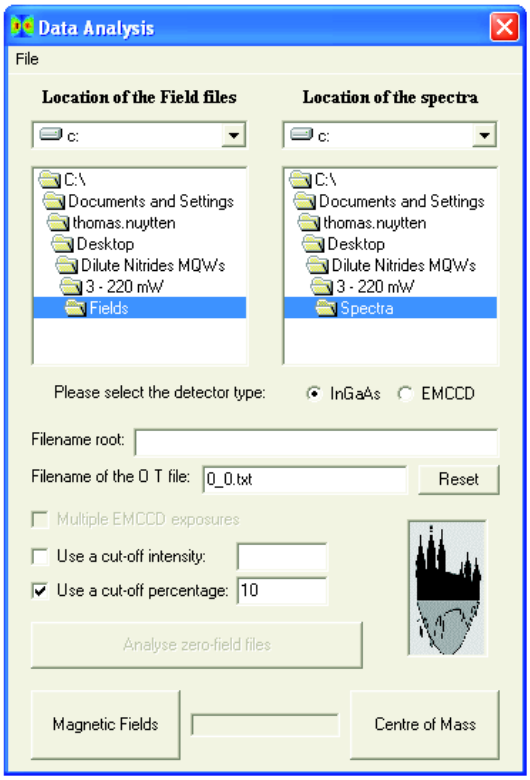

Figure 2.7: Screenshot of the pulsed fields data analysis program.

The program can be used to analyse data outputs of both detectors, and uses the files from the digital recorder to calculate the correct mean magnetic field values for each exposure. A screenshot of the program's main screen is shown in Figure 2.7.

As was discussed in Section 1.3.2, the important information that emerges from the magneto-PL experiments is contained within the shift of the PL energy as a function of magnetic field. The output of the program contains a list of the centre of mass energy and the corresponding magnetic field for each exposure. Once all data are analysed by the program, a plot of the centre of mass energy versus magnetic field can be produced. The fitting procedure that is based on Equation 1.19a

and 1.19b, uses three free parameters (one of which is the cross-over field B_c) that can be used to determine the exciton effective mass μ, radius $\langle\rho^2\rangle^{\frac{1}{2}}$ and energy shift ΔE_{cm}. A typical result of this analysis is shown in Figure 2.8 for sample i1341, which is an InAs QD sample studied in Chapter 5.

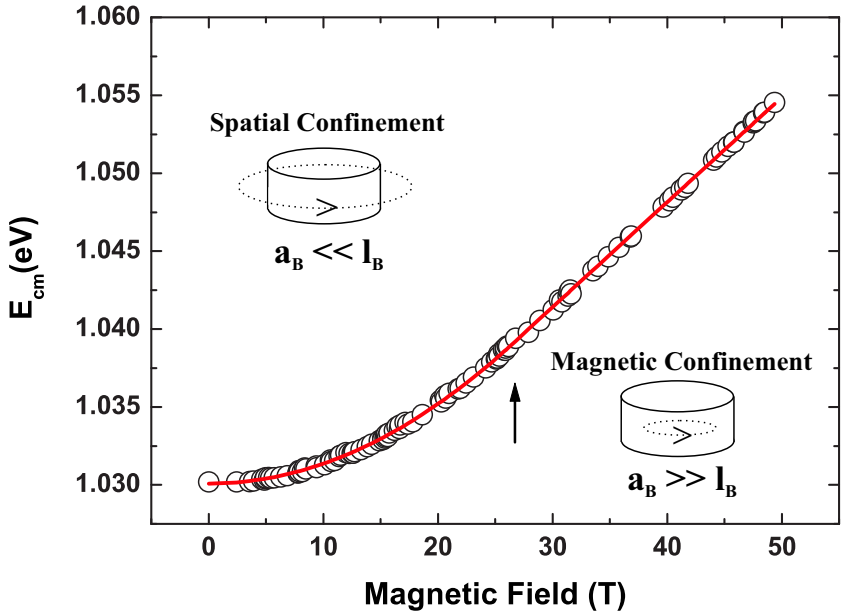

Figure 2.8: A typical plot of the centre of mass energy (E_{cm}) versus magnetic field for sample i1341 (InAs QD sample, see Chapter 5) at 4.2K. The circles are data points while the full line is the fit using the excitonic model described in Section 1.3. At low magnetic fields, the spatial confinement of the nanostructure is more important than the magnetic confinement. The arrow indicates the cross-over field to the high field regime, where the magnetic confinement dominates the spatial limitations of the nanostructure, and the exciton is compressed to a size smaller than the physical dimensions of the QD.

The quadratic and linear regime as discussed in Section 1.3 can clearly be distinguished in Figure 2.8, and the cross-over between both regimes occurs at ~ 26 T, as indicated by the arrow. The binding energy can be graphically determined as the difference between the zero-field

PL energy and the intersection between the linear part of the fitting curve and the left ordinate axis, or from the hydrogenic model:

$$E_B = \frac{\hbar^2}{2\mu a_B^2} \tag{2.3}$$

which is the second term on the right of Equation 1.19b. For a very loosely bound exciton the binding energy is very small, which translates into a completely linear behaviour of $E_{cm}(B)$, a quadratic regime is absent, and we can no longer use Equation 1.19a to determine the exciton wave-function extent. The exciton effective mass however can still be calculated from the slope of the linear regime using Equation 1.19b.

Chapter 3

Temperature dependence of the photoluminescence of self-assembled InAs/GaAs quantum dots

As discussed in Section 1.1, an ensemble of self-assembled quantum dots is characterised by spatial confinement of the carriers in all three dimensions. Ideally, such an ensemble has an energy spectrum consisting of discrete energy levels, of which the density of states profile is a collection of delta-like functions, which makes them an outstanding candidate for the integration in novel optoelectronic devices [17–19]. However, for devices such as lasers, the occupancy of these levels is ideally temperature independent for $T \leq 360$ K, but such ideal behavior is not observed in practice. Hence, a thorough understanding of the effect of temperature is essential for device fabrication. In this Chapter, we will investigate the temperature dependence of the magneto-PL of self-assembled InAs/GaAs quantum dots.

3.1 Sample characterisation and experimental details

The samples were kindly supplied by Prof. M. Henini from the University of Nottingham and were prepared using solid-source molecular beam epitaxy. A 0.5 μm thick GaAs layer was grown on top of a semi-insulating (100) GaAs substrate. Subsequently, 1.8 monolayers (ML) of InAs were deposited at a temperature of 480°C. During this phase, quantum dots were formed following the Stranski-Krastanow growth mode (see Section 1.1.2). Finally, the sample was capped with 25.2 nm of GaAs. Magneto-PL experiments were carried out in a helium bath cryostat at low temperatures (4.2 K) and a helium flow cryostat for temperature-dependent measurements (see Section 2.5). The sample was excited by green laser light (532 nm) with a power density of about 5 Wcm^{-2}.

3.2 Experimental Results

3.2.1 Zero-field photoluminescence

When increasing the temperature of bulk semiconductor material, the crystal lattice expands, phonon-assisted processes are activated and the interatomic bonds are weakened. Hence, the band-gap energy decreases as a function of temperature, and its behaviour can be described by the empirical Varshni law [20]:

$$E_g(t) = E_g(T = 0) - \frac{\alpha T^2}{T + \beta} \tag{3.1}$$

where $E_g(T = 0)$ is the band-gap energy at 0 K and α and β are the adjustable parameters, typical for each semiconductor material. For InAs, they are given by [21]:

$$\alpha(\Gamma) = 0.276\frac{\text{meV}}{\text{K}} \tag{3.2a}$$

$$\beta = 204\text{K} \tag{3.2b}$$

at the Γ -point of the Brillouin-zone ($k = 0$). For the temperature dependence of InAs quantum dots, a similar behaviour is expected.

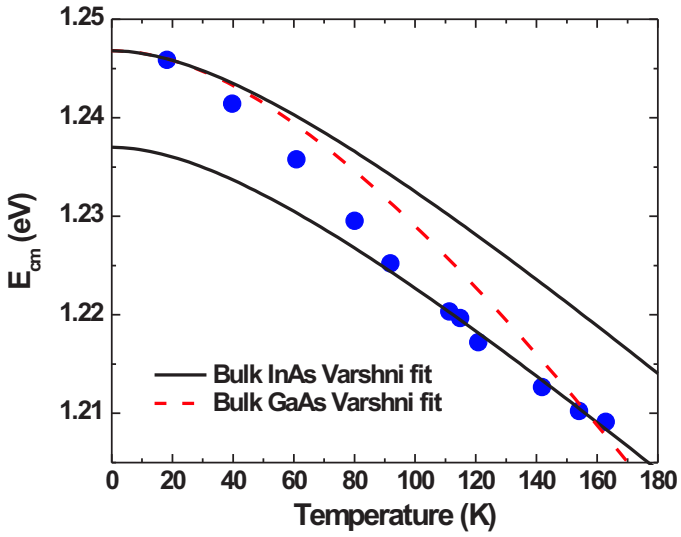

Figure 3.1: Temperature dependence of the centre of mass PL energy. The full lines represent Varshni fits for the InAs band-gap, while the dashed line is for the bulk GaAs. At low temperatures, the decrease of the PL energy is faster than predicted by the Varshni [20] relation for both the InAs and GaAs band-gap, while at high temperatures, a typical band-gap red shift is observed. The Y-intercepts of the Varshni dependence are shifted up and down to account for the difference in energy between the QD and bulk ground states.

Figure 3.1 depicts the zero-field centre of mass PL energy as a function of temperature between 20 and 160 K, together with Varshni fits for the InAs and GaAs band-gap, shifted up and down to account for the

differences in energy due to confinement. The fit for GaAs and one of the InAs fits are shifted to agree with the first data point at low temperatures, while the second InAs fit coincides with the behaviour at higher T. For temperatures below 80 K, the decrease in the energy with temperature is faster than predicted by the Varshni law for both the InAs and GaAs band-gap. At higher temperatures ($T \geq 100$ K) however, the PL energy appears to follow the InAs band-gap dependence. The behaviour can be thought of as a cross-over between two different regimes, each of which follows a Varshni dependence with different $E_g(T = 0)$, as is illustrated in Figure 3.1.

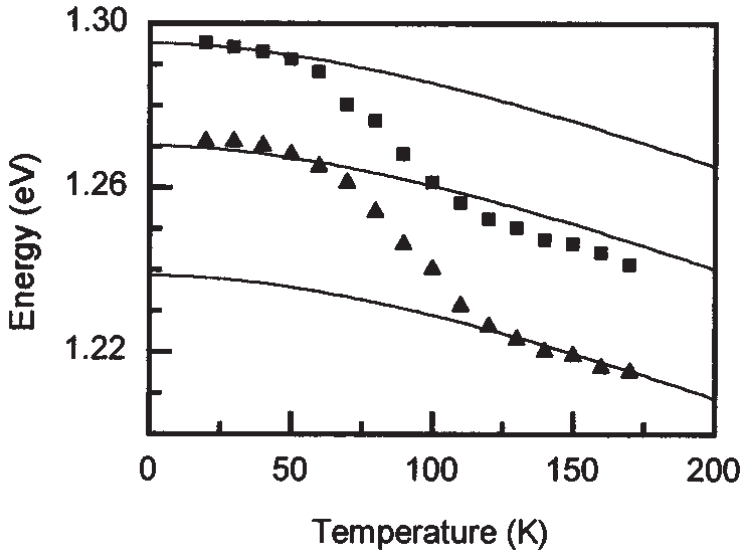

Figure 3.2: Temperature dependence of the PL peak energy for QD samples with 1.8 ML (squares) and 3.0 ML (triangles) of InAs coverage taken from [22]. The sigmoidal behaviour is ascribed to transfer of carriers between different dot families with well defined sizes.

This behaviour was previously observed and attributed to thermal redistribution of electrons from higher- to lower-energy dots via the wetting layer [22–24]. The increase of temperature thus not only activates

the expansion of the lattice and phonon-related effects but also introduces an additional transfer of carriers between the dots via the wetting layer, which favors lower-energy recombination. At higher temperatures, the PL energy nicely follows the changes according to the Varshni law for the InAs band gap. Following Brusaferri *et al.* [22], who reported evidence of families of dots with *remarkably uniform sizes* (see Figure 3.2), we interpret this temperature dependence of the PL energy as suggesting the presence of different dot families with distinct sizes in our sample. We note that at this stage, we cannot explicitly rule out any possible effects of composition fluctuations. However, as we will see in the following section, the results from experiments in pulsed magnetic fields are entirely consistent with the idea of an enhanced transfer of carriers toward lower-energy dots via the wetting layer.

3.2.2 Photoluminescence in magnetic field

In order to gain further insight into the confinement of the carriers inside the dots, we then studied the magneto-PL of the sample at different temperatures and with different orientations of the field with respect to the growth direction. Upon application of a magnetic field, the structure of the exciton is affected mainly through a compression of the wave-function in the plane perpendicular to the applied field[1]. Therefore, when examining the PL shift with $B \parallel z$, the exciton radius in the plane of the sample is measured. On the other hand, with $B \perp z$, we probe the vertical and one lateral dimension of the dots. However, since it is the direction with the strongest confinement (smallest exciton radius) that determines both the size of the shift with field and the crossover field B_c [25] and since the dots are smaller in the growth direction than in the plane of the sample, applying a magnetic field in the plane of the

[1] It should be noted however, that at extremely high fields, a Coulomb-confined ground state wave-function can be elongated *along* the direction of the magnetic field, the latter effect being due to the *lack of space* in the quantised *tubes* of radius $a_{Larmor} = \sqrt{\frac{2\hbar}{eB}}$. For fields up to 50 T however, such effects are negligible compared to the compression in the direction perpendicular to the applied field.

sample probes the vertical extent of the exciton. Indeed, we find that the shift and effective exciton radius are smaller for this field orientation, in agreement with earlier magneto-PL measurements on self-assembled QD nanostructures [26–29].

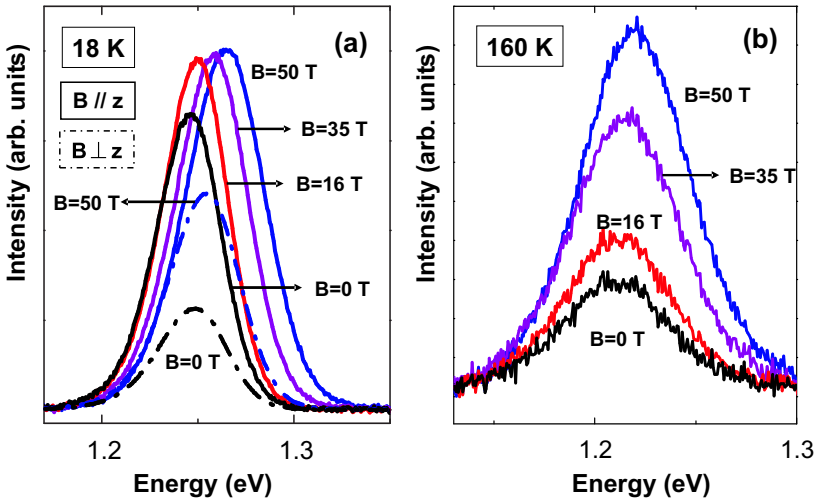

Figure 3.3: PL spectra at different magnetic fields for the $B \parallel z$ (full lines) configuration for (a) 18 and (b) 160 K. Two PL spectra for the $B \perp z$ (dash-dotted lines) orientation at low temperatures are also shown in left panel (a). The PL intensity is enhanced when applying a magnetic field, in particular for the experiments at higher temperatures. The low temperature data have a larger field shift compared to the high temperature data. Additionally, it can be seen that the PL shift with field is larger for the $B \parallel z$ orientation than for the $B \perp z$ configuration.

Figure 3.3 shows PL spectra for different strengths of the magnetic field for 18 and 160 K. From these spectra, it is already clear that the PL energy shift with B is larger at low temperatures and that the intensity of the PL signal is significantly reduced when increasing the temperature due to the activation of nonradiative channels. Furthermore, it should be noted that the increase in PL signal with magnetic field is much more pronounced at high temperatures than at low temperatures. Additionally, it is clear that the shift of the PL centre of mass is much

larger in the $B \parallel z$ direction than in the $B \perp z$ direction.

The dependence of the PL peak energy on magnetic field is summarized in Figure 3.4 for the same two temperatures. The 18 K data are typical of the low temperature regime, which is characterized by a crossover from parabolic to linear field dependence at a certain critical field B_c (see Section 1.3.2), indicated by the arrow. As the temperature increases above 100 K, the shift of the PL energy is reduced, and there is a decreasingly smaller linear regime at fields below 50 T, indicating stronger confinement. Figure 3.5 shows the energy shift with magnetic field (ΔE_{cm}) as a function of temperature for both field orientations. From this figure, it is evident that, for lower temperatures, *i.e.* below 80 K, as the temperature is raised, there is a strong increase in ΔE_{cm} with the magnetic field perpendicular to the growth direction ($B \perp z$), whereas an increase in temperature hardly affects the energy shift for $B \parallel z$. In contrast, for $T > 100$ K, there is a drastic reduction in the size of the shift for both field orientations. Given such different behavior, it seems clear that different mechanisms are at work in the two temperature regimes of our experiment. We will therefore go on to discuss each of these separately.

3.2.3 Low temperature regime ($T < 80$ K)

For the low temperature regime, the dependence of the shift ΔE_{cm} on temperature is substantially different for the two different field orientations, as can be seen in Figure 3.5. While the shift is more or less constant with a magnetic field applied in the growth direction, experiments with $B \perp z$ reveal an increase of the shift with temperature. As mentioned above, when $B \perp z$, we are probing the vertical extent of the exciton, since this is the direction with the strongest confinement with this field orientation. Because the exciton wave-function is so small in this direction, ΔE_{cm} is dominated by the low-field regime where it is proportional to $\frac{\langle \rho^2 \rangle}{\mu}$ (see Equation 1.19a). An increase in ΔE_{cm} is thus either because μ is decreasing or $\sqrt{\langle \rho^2 \rangle}$ is increasing (or both).

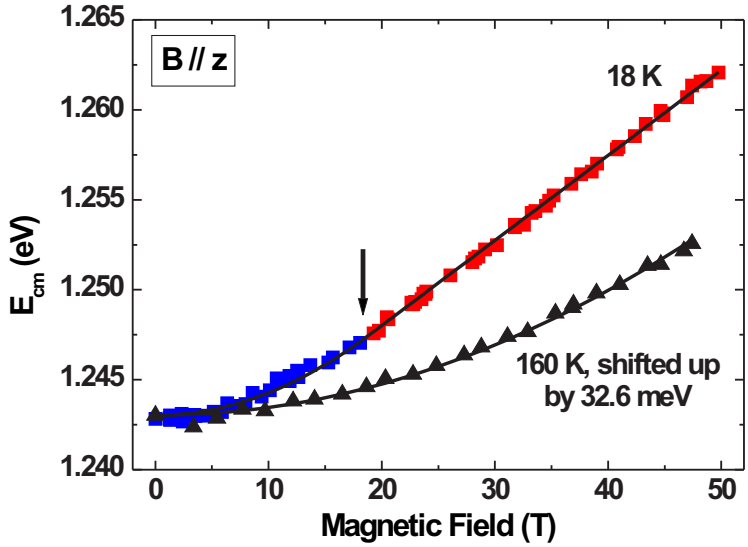

Figure 3.4: The centre of mass PL energy, E_{cm}, versus magnetic field. The data for 160 K have been shifted up for clarity. The solid lines are fits to the data using Equation 1.19. At lower temperatures, a cross-over from parabolic to linear behaviour occurs at 19 T (indicated by the arrow), whereas the 160 K data are parabolic up to 50 T. Note that the energy shift is much larger for low temperatures.

However, if it was only because μ was decreasing, this would also increase the confinement energy, and result in an increase of the zero-field PL energy relative to the change expected from the Varshni law, which is the opposite of what we observe (see Figure 3.1). On the other hand, a decrease in the zero-field PL energy is entirely consistent with an enhanced transfer of carriers toward larger QDs leading to a decrease in confinement. Hence, the increase in ΔE_{cm} with the magnetic field perpendicular to the growth direction indicates an expansion of the exciton wave-function in the growth direction reflecting the increased contribution of larger QDs to the PL emission. In contrast, the energy shift with

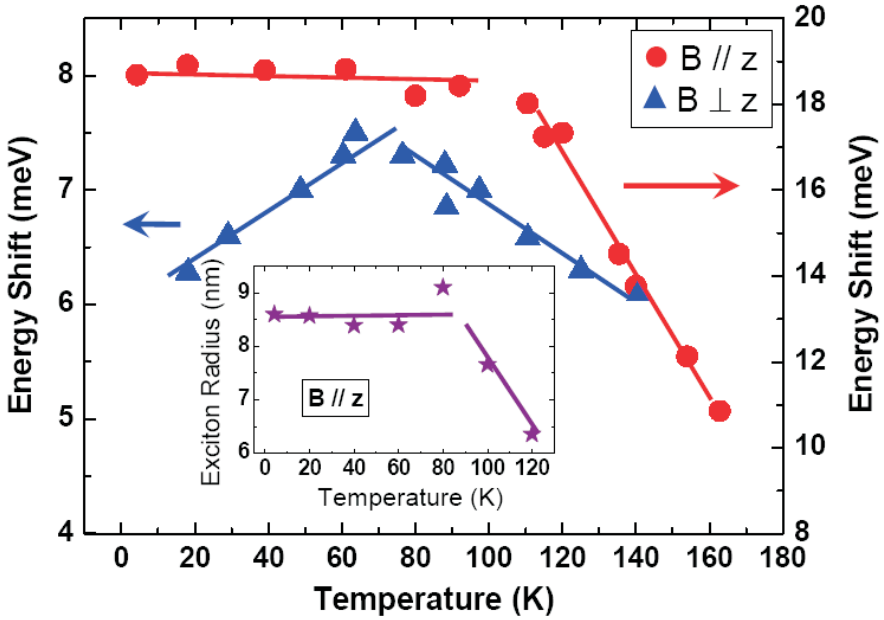

Figure 3.5: Energy shift between 0 and 50 T versus temperature for a magnetic field applied parallel (circles) and perpendicular (triangles) to the growth direction. A strong decrease of the PL shift characterises the high temperature ($T > 100$ K) regime. The inset shows the exciton wave-function extent as a function of temperature following Equation 1.19 for $B \parallel z$ and reveals an apparent wave-function shrinkage at high temperatures. For $T > 120$ K, the lateral exciton radius becomes so small that the crossover to the high-field regime is at too high a field to be determined reliably. The lines are guides for the eyes.

magnetic field parallel to the growth direction remains unaltered at temperatures below 80 K. Thus, the explanation of the data in Figure 3.1 that there is thermal excitation from smaller to bigger dots is indeed supported by our magneto-PL measurements, but the magneto-PL data crucially reveal that *these dots are larger in size only in the growth direction*: there is no indication of a change in the average lateral size of the ensemble of dots in this temperature range.

3.2.4 High temperature regime ($T > 100$ K)

We now turn to the high temperature regime. Here, the field-induced PL shift is characterized by a massive decrease as a function of temperature in both field orientations (Figure 3.5). Applying an analysis to the data following the magnetic field dependence of the peak energy as described in Equation 1.19 would lead us to interpret this as a shrinkage of the exciton radius (or, equivalently, an increase in confinement) as a result of increasing temperature (inset of Figure 3.5). However, if the QDs active at higher temperatures were, on average, smaller than the ones responsible for the PL at low temperatures, their confinement energy should be higher, as would be the corresponding transition energies within the QD. In this case, the zero-field PL energy would not follow the empirical Varshni law for the InAs band gap but show a weaker temperature dependence or even an increase as a function of temperature, *i.e.*, the exact opposite of what we observe at low temperature. However, this is clearly not the case, and we therefore conclude that the decrease of the field-induced PL shift with temperature is not due to a decrease of the (zero-field) exciton radius as a function of temperature, but that it has some other cause.

3.2.5 Field-enhanced confinement

The contradiction is resolved when noting that the energy shift is determined in the presence of a very strong magnetic field, which, we propose, affects the confinement potentials. In general, applying a magnetic field causes the energy levels of bulk GaAs (the barrier material) to be lifted by $\frac{1}{2}\hbar\omega_c$, or about 0.9 $\frac{meV}{T}$[2]. In contrast, the PL energy shift between 0 and 50 T of the InAs QDs with $B \parallel z$ for the considered temperature

[2]Here, we have calculated the increase in barrier height for the electrons, since in GaAs, the hole mass is much larger than the electron mass (0.35 μ_0 and 0.067 μ_0, respectively [21]), which is why the effect is much more pronounced for the electrons and we can approximate the increase in barrier energy for the exciton by that for the electron. However, the total increase in energy for the dots would be the increase for the excitons (holes+electrons), which makes our assessment an underestimate of the effect.

range varies between 10 and 20 meV (see Figure 3.5), resulting in an energy shift of about $0.2 - 0.4\ \frac{meV}{T}$. This means that upon application of a magnetic field, the energy levels of the barrier material are lifted at a much faster pace with respect to the energy levels of the InAs QDs.

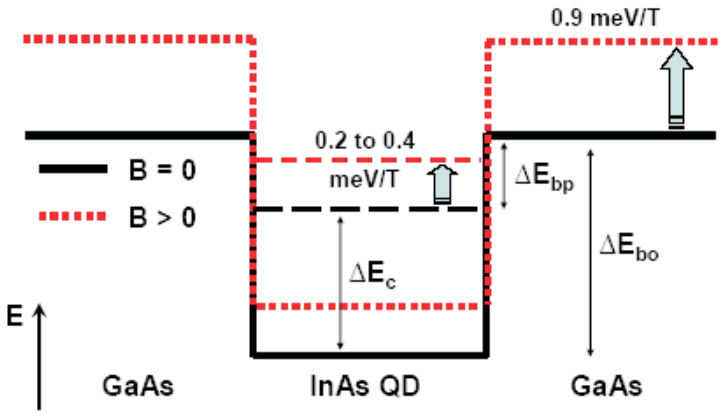

Figure 3.6: Schematic representation of the electron energy levels of the InAs QDs and GaAs matrix material as they are lifted by the magnetic field. The differential rise in energy levels as a function of B increases the effective barrier height by $0.5 - 0.7\ \frac{meV}{T}$. The confinement energy ΔE_c, the barrier potential ΔE_{bp}, and the band offset ΔE_{bo} at B=0 T are indicated.

Figure 3.6 shows a schematic representation of the electron energy levels of an InAs QD in the GaAs matrix and illustrates the fact that the application of a strong magnetic field increases the energy gap between the states in the QDs and the states of the surrounding bulk GaAs material. When applying a magnetic field, the energy levels of the GaAs barrier material are substantially raised, while the increase of the QD levels is rather moderate. Consequently, a strong magnetic field enhances the temperature stability of the system by counteracting the escape of carriers from the dots into the surrounding barrier material. This phenomenon has previously been observed in quantum well laser structures in an attempt to simulate a reduction in dimensionality by

placing the structure in a magnetic field [30,31]. However, the influence of a magnetic field on the energy levels of the QDs is strongly dependent on the degree of confinement present in the dots. Smaller dots have a stronger confinement potential, resulting in a weaker dependence on magnetic field. Therefore, the energy levels of the excitons with strong lateral confinement, *i.e.*, those with a weak energy shift in magnetic field ($0.2\ \frac{meV}{T}$), are lifted much less than the ones with a weak lateral confinement, as the latter have a larger PL shift in field ($0.4\ \frac{meV}{T}$). In both cases, however, the barrier energy is raised by the same larger amount. This results in a field-induced enhancement of $0.7 - 0.5\ \frac{meV}{T}$ of the QD barrier potential. Correspondingly, the extra energy difference between the QD levels and the GaAs barrier material at 50 T is 35 meV (400 K) for the high-energy dots (*i.e.*, the ones with strong lateral confinement), while it is only 25 meV (290 K) for the low-energy dots (*i.e.*, with weaker lateral confinement). In other words, the effect of the magnetic field is to deepen the confinement potentials of the QDs, and counterintuitively, the mechanism is much stronger for smaller, high-energy dots, as the energy levels of these dots are the least affected by a magnetic field.

As a consequence, under the influence of a magnetic field, it becomes increasingly more difficult to excite carriers out of the QDs into the GaAs matrix material, and this effect is much stronger for the high-energy dots. The result is that at high temperatures and high magnetic fields, the contribution of the high-energy dots to the PL relative to the low-energy dots is increased, which, in turn, results in a smaller PL shift in magnetic field. This explanation is supported by the observation that at high temperatures, the PL intensity is strongly increased upon applying a magnetic field, as can be seen in Figure 3.3(b). In contrast, at low temperatures, when there is insufficient thermal energy to excite the carriers entirely out of the InAs dots and wetting layer into the barrier material, the magnetic field has very little impact on the PL intensity [Figure 3.3(a)]. This corroborates the assertion that the excitation between large and small dots at low temperature occurs via the wetting layer [22–24].

3.3 Conclusions

We have studied exciton confinement in self-assembled InAs/GaAs QDs. At low temperatures ($T < 80$ K), we find that the PL energy decreases faster with temperature than predicted by the Varshni law [20] for the InAs band gap. This is attributed to thermal excitation via the wetting layer to dots which are larger only in the growth direction of the sample. At higher temperatures ($T > 100$ K), we observe a strong decrease of the PL shift with field in both directions, which we attribute to field enhancement of the QD barrier potential. As the influence of a magnetic field on the energy levels of the QDs depends inversely on the confinement energy, this mechanism is particularly important for smaller dots.

Chapter 4

Strain-compensated $Ga_{1-x}In_xN_yAs_{1-y}$ multiple quantum wells

Contrary to the general rules of III-V alloy semiconductors where a smaller lattice constant increases the band-gap energy, a famous paper by Kondow *et al.* [32] presented the GaInNAs alloy as a novel wide band-gap material on GaAs substrates [3]. The combination of this unique property with an enhanced temperature stability makes GaInNAs an excellent candidate for the fabrication of long-wavelength telecommunication lasers, and subjected it to intense research in the past few years. In this Chapter, we will study the still poorly understood carrier localisation present in this material.

4.1 The $Ga_{1-x}In_xN_yAs_{1-y}$ system

4.1.1 Nitrogen and indium incorporation

When constructing random semiconductor alloys like $In_xGa_{1-x}As$ the electronic properties of such alloys can, to a first approximation, be described by the *Virtual Crystal Approximation (VCA)*, which gives

the properties of perfectly random alloys as a linear interpolation between the end-point materials [33]. The deviations from the VCA are usually included through a bowing parameter that accounts for the alloy disorder effects. Figure 4.1 shows such an approximation for the $In_xGa_{1-x}As$ material as an interpolation between GaAs and InAs. One would be led to believe that 1.3 and 1.55 μm emission could be achieved by simply using a suitable intermixture between In and Ga, but the increase in emission wavelength is limited to about 1.2 μm due to limitations of the pseudomorphic growth regime when growing on GaAs substrates [34]. However, the addition of only a few percent of nitrogen to the $In_xGa_{1-x}As$ system results in a number of unusual properties, one of which is a giant reduction of the band-gap energy, making the telecommunications window accessible without the need for excessive indium incorporation [32].

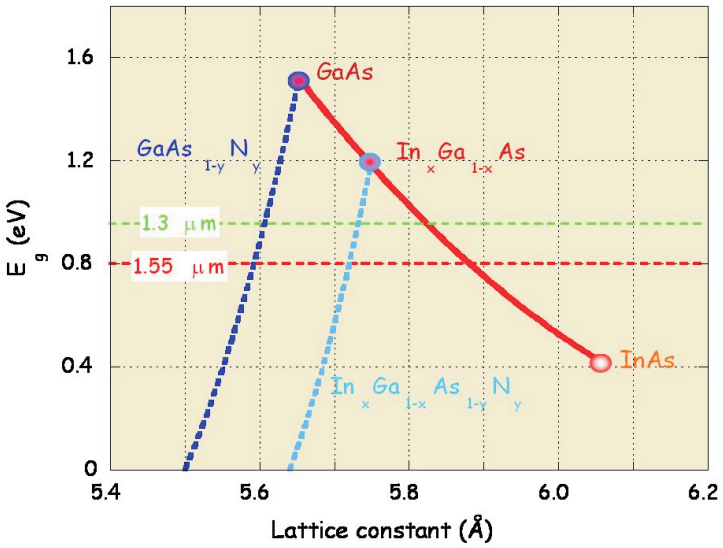

Figure 4.1: Band-gap energy for bulk material as a function of the lattice constant. The virtual crystal approximation interconnects the points for GaAs and InAs. The massive reduction in band-gap energy upon incorporation of N is indicated by the dotted curves [35].

When introducing nitrogen which has a smaller atomic radius and larger electronegativity compared to arsenic in the $In_xGa_{1-x}As$ system, both the structure of the crystal and its charge distribution are altered. These local perturbations result in the formation of a narrow band of nitrogen-induced localised energy levels slightly above the conduction band minimum of the semiconductor matrix. The *band anticrossing model* [33, 36–38] describes the interaction of these localised levels with the $In_xGa_{1-x}As$ band structure in terms of a splitting of the conduction band into two different sub-bands, E_+ and E_-, of which the reduction in band-gap energy is a direct result (Figure 4.2).

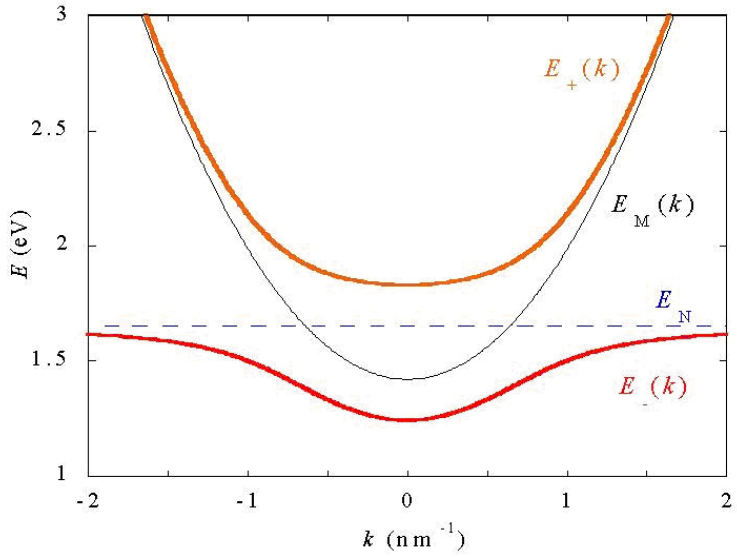

Figure 4.2: Perturbation of the crystal lattice potential through *anticrossing interaction* with the nitrogen-induced localised energy levels in the vicinity of the Γ point in the Brillouin zone. The thin parabolic line in the middle is the conduction band edge $[E_M(\mathrm{k})]$ and the dashed line represents the localised energy levels (E_N). The upper and lower thick lines are the split bands $E_+(\mathrm{k})$ and $E_-(\mathrm{k})$, respectively [35].

Although the presence of a small amount of nitrogen in the $In_xGa_{1-x}As$ alloy causes a dramatic red shift of the host material band-gap and an

increased insensitivity of the band-gap energy to temperature [39], the fabrication of high-quality $Ga_{1-x}In_xN_yAs_{1-y}$-based 1.55 μm devices remains a difficult task. Because of the very steep dependence of the band-gap energy on the nitrogen concentration, small local fluctuations in nitrogen content induce very strong carrier localisation. Additionally, a large miscibility gap results in an increased phase separation tendency [40, 41], even to the extent of forming QD-like compositional fluctuations [42]. In order to keep this degradation of the crystalline quality to a minimum, a higher indium concentration in the quantum well (QW) material has been used. This results in a higher degree of strain at the interface between the $Ga_{1-x}In_xN_yAs_{1-y}$ QW and the $GaAs_{1-y}N_y$ barrier layer, which can, in turn, be offset by the use of quaternary $Ga_{1-x}In_xN_yAs_{1-y}$ material for the barrier layers; this reduces the strain at the interface and improves the optical and structural properties of $Ga_{1-x}In_xN_yAs_{1-y}$/GaAs 1.55 μm multiple quantum wells (MQWs) [41, 43].

4.1.2 Sample characterisation

The UK National Centre for III-V Technologies of the University of Sheffield[1] provided us with two samples, labeled *A* and *B*, grown on (001) GaAs substrates by molecular beam epitaxy, with nitrogen incorporated using a radio-frequency plasma source [41, 44, 45]. The active region for sample A consists of a 52 nm $GaN_{0.007}As_{0.993}$ barrier layer followed by five 8 nm $Ga_{0.65}In_{0.35}N_{0.023}As_{0.977}$ QWs between $GaN_{0.007}As_{0.993}$ spacer layers and another $GaN_{0.007}As_{0.993}$ barrier layer (see Figure 4.3). Sample B has the same structure but has three $Ga_{0.62}In_{0.38}N_{0.03}As_{0.97}$ QWs between $Ga_{0.977}In_{0.023}N_{0.01}As_{0.99}$ barriers.

The $GaN_{0.007}As_{0.993}$ barriers in sample A are tensile-strained and thus act as strain compensating layers to the compressively strained QWs, while the small addition of indium to the barrier material in sample B reduces the strain at the QW/barrier interface. The growth tem-

[1] The samples were grown by Dr. H.Y. Liu in collaboration with Prof. M. Hopkinson.

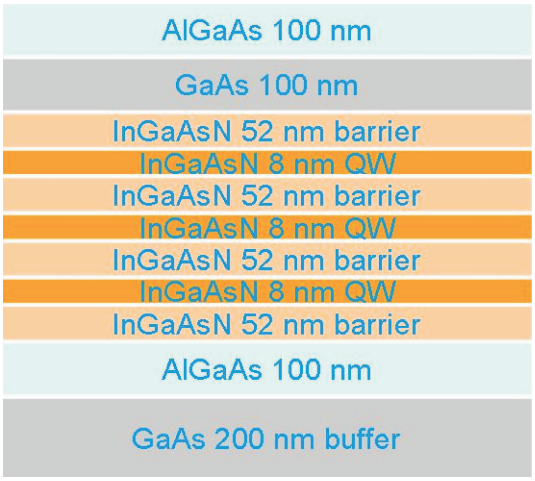

Figure 4.3: Structure of the active region for sample A. Sample B has a similar structure, but with five QWs instead of three.

peratures for the active regions were 460°C for sample A and 325°C for sample B, while the annealing times at 660°C were 40 and 60 minutes, respectively. In general, the recombination energies are rather inhomogeneous across the wafer, possibly due to a nonuniform nitrogen distribution. We have therefore consistently used the same piece of sample for all the experiments.

4.2 Experimental results

There are two main differences between sample A and sample B. First, the growth temperature of sample A (460°C) is considerably higher than for sample B (325°C). In general, the mobility of the atoms is much larger at the surface than inside the bulk material, and so although a high post-growth annealing temperature may be used, the influence of the temperature during growth is much more important in terms of compositional homogeneity [46, 47]. Since it is a well-established result [47–53] that a high growth temperature promotes decomposition of the alloy, we expect the lower growth temperature sample (sample B) to exhibit better optical quality. Second, there is the presence of 2.3 % of indium in the barrier material of sample B, which has been shown to drastically enhance the optical quality of the MQW structure [41, 43].

The addition of indium to the barrier material reduces the strain at the QW/barrier interface. As a result, the PL intensity is enhanced and a reduction of the PL linewidth is observed[2]. These two differences indicate that there should exist a pronounced enhancement of the structural quality when going from sample A to sample B. In the present work we use magneto-PL to study carrier localisation in these two contrasting samples: one sample in which the optical and structural properties are expected to be rather poor, and one sample with optimised growth temperature and sample morphology. In this way we are able to build up a consistent phenomenological picture of the localisation of electrons and holes in the two samples.

4.2.1 Temperature dependence in the absence of a magnetic field

In order to investigate the degree of localisation in our samples, we have examined the temperature dependence of the PL energy for both samples (Figure 4.4).

In agreement with earlier studies [39, 44, 54–57], a nonmonotonic dependence of the PL centre of mass versus T is observed and is attributed to trapping and subsequent detrapping of carriers by localised states. At low temperatures, a slight increase in temperature thermalises the carriers allowing them to reach regions with a higher degree of localisation, recombination from localised states increasingly dominates the PL, and we find a fast red shift with increasing T, which is due to the temperature-induced trapping of carriers by the localised states[3]. At around 100 K for sample A, and 50 K for sample B, carriers have enough thermal energy to escape the localisation, and redistribution toward the

[2] In [41], the introduction of 2.3% indium realises a 150% enhancement of the PL intensity and a decrease of 30% of the PL linewidth with respect to a reference sample without indium in the barrier.

[3] There is a strong analogy to what we have observed in the InAs QDs, where thermal redistribution of carriers from higher- to lower-energy dots induced a decrease of the PL energy with temperature much faster than the band-gap dependence (see Section 3.2.1). Here, the carriers are trapped by local potential fluctuations instead of QDs, and the carrier transfer occurs via the QW.

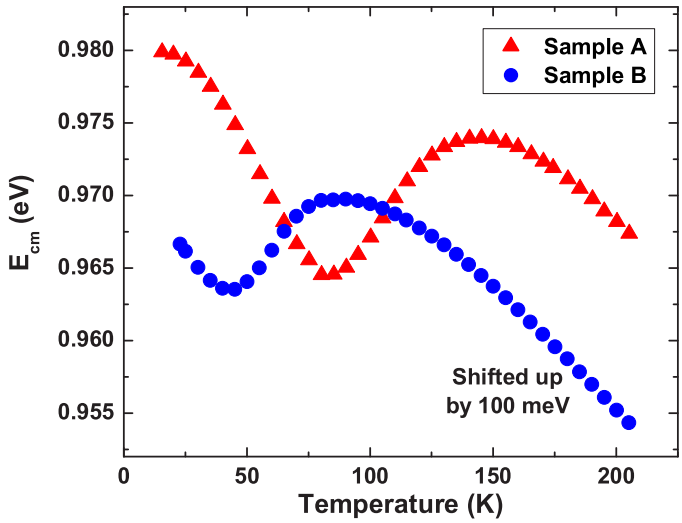

Figure 4.4: Temperature dependence of the PL energy for samples A (triangles) and B (circles). The local minimum, typical for recombination from localised states, is more pronounced and appears at higher T for sample A. The data for sample B have been shifted up by 100 meV for clarity.

higher energy free-exciton levels causes a decrease in the population ratio between localised and free excitons. This progressive carrier detrapping from the localised states shifts the centre of mass of the carrier distribution toward higher energy. Consequently, the PL signal is increasingly dominated by recombination from free excitons, whose energy levels are higher than the localised levels, and a blue shift is observed. At higher T, a band-gap-like red shift of the PL signal is found, showing that radiation from free excitons only contributes to the PL. Hence, the temperature dependence of the PL energy has a sigmoidal form (Figure 4.4). According to previous studies [58], the temperature at which the T-dependence recovers to a band-gap-like behavior gives an indication of the degree of localisation, and in general an increase in nitrogen content increases this temperature. Although the nitrogen incorporation in

sample B is slightly higher than that in sample A (x=0.023 and x=0.03 respectively), the local minimum of the s-shape occurs at higher T for sample A and is about 50 % deeper with respect to sample B, which demonstrates the stronger degree of localisation of the former. Additionally, previous studies have shown that such a difference in nitrogen incorporation should not have dramatic effects on the properties of the alloy [41].

4.2.2 Excitation power dependence of the zero-field PL energy

Figure 4.5 shows the dependence of the PL spectrum on the laser excitation power density for sample A over six orders of magnitude. We observe a clear blue shift when increasing the excitation power density, a phenomenon that is commonly described as a signal of spatially indirect recombination [59, 60].

However, since we are studying two-dimensional structures, a spatial separation of the charge carriers is only possible by means of localised potential fluctuations that can trap electrons or holes. Indeed, the blue shift of the PL energy with increasing excitation power has been attributed to carrier filling of the localised states [39]. The PL peak becomes increasingly more Gaussian at higher excitation powers, indicating that the localised recombination centres tend to saturate at higher excitation power densities [61].

Figure 4.6 depicts the excitation power density dependence of the PL peak energy over 6 orders of magnitude. The blue shift mentioned above is clearly present, and a small kink at powers of about 1 $\frac{W}{cm^2}$ can be noticed. Although it remains unclear what the origin of the change in slope is, we can rule out an excitation power-induced cross-over to two-exciton state emission. The integrated intensity of the PL signal should have a quadratic dependence on the power density for a biexcitonic emission, while a linear scaling is expected for luminescence originating from a single electron-hole recombination [62]. As can be seen in Figure 4.6,

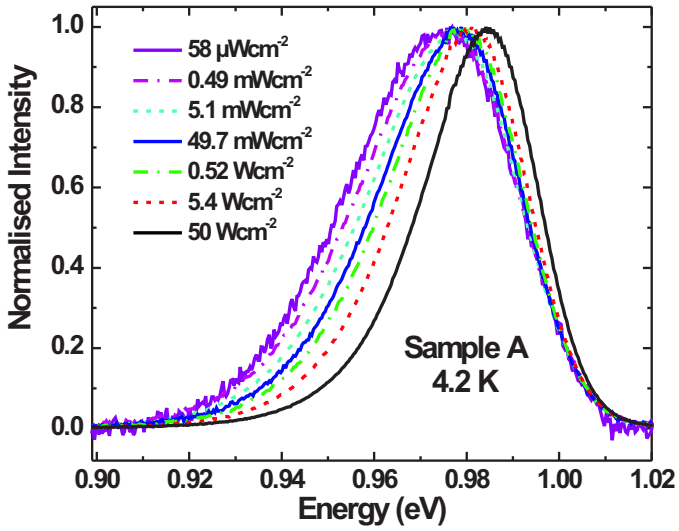

Figure 4.5: Excitation power dependence over six orders of magnitude for sample A. A blue shift, combined with a reduced importance of the low-energy shoulder of the PL peak is clearly noticeable.

the dependence of the integrated intensity on the excitation power density is entirely linear, and no transition to biexcitonic recombination can be distinguished.

PL studies in the absence of a magnetic field with varying excitation powers for sample B reveal a completely different result. Within the experimental errors, there is no detectable shift of the PL peak for laser power densities increasing over five orders of magnitude (see Figure 4.7). Since the integrated intensity is, similar to the situation in sample A, characterised by a linear scaling to the excitation power, we conclude that the recombination in sample B is also excitonic, but that there is a considerable reduction in the localisation of the charge carriers. In order to work out a consistent picture of the exciton localisation in our samples, we have carried out magneto-photoluminescence experiments.

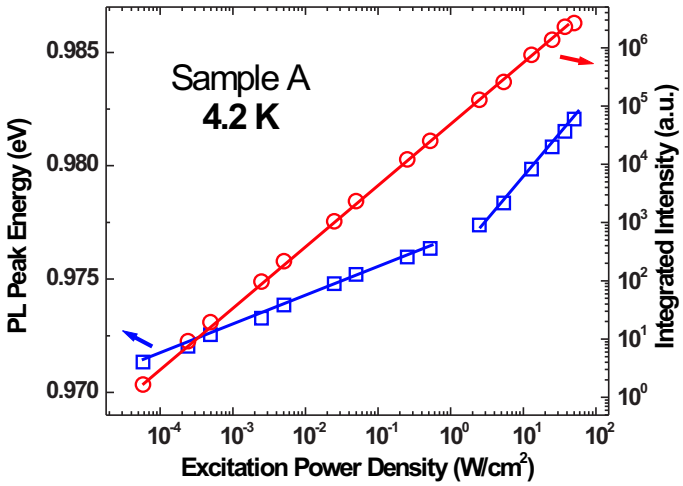

Figure 4.6: PL peak energy (squares) and integrated intensity (circles) as a function of excitation power density. A clear blue shift, with a small kink at $\sim 1\ \frac{W}{cm_2}$ is observed, hinting at spatially indirect recombination. The integrated intensity is linearly dependent on the excitation power, confirming that the recombination is excitonic.

4.2.3 PL centre of mass in pulsed magnetic fields

As was discussed in Chapter 1, PL in pulsed magnetic fields is an excellent technique for studying exciton confinement in low dimensional semiconductors. In particular, it is an attractive approach for studying the degree of localisation in our MQW samples. By analysing the shift of the PL centre of mass energy E_{cm} with magnetic field (using the model described in Section 1.3.2), we can extract important parameters that govern the opto-electronic behaviour of the MQWs, such as the exciton wave-function extent and effective mass.

Figure 4.8 shows the shift of the PL centre of mass energy E_{cm} versus magnetic field for both samples A and B at 4.2 K. The centre of mass of the PL peak of sample B is characterised by a linear dependence on magnetic field right down to the very lowest fields that can be produced

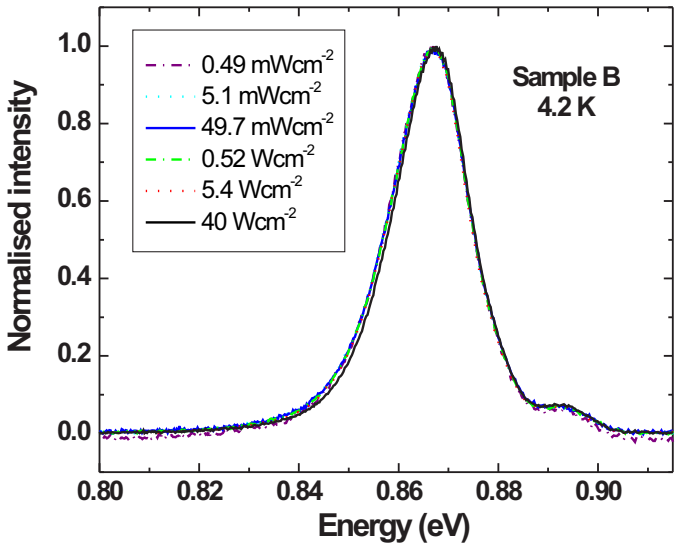

Figure 4.7: Excitation power dependence over five orders of magnitude for sample B. The main PL peak does not shift with changing excitation power.

with our pulsed fields set-up, whereas the data for sample A show a crossover from parabolic to linear behavior at around 8.5 T, indicating that for sample A, a stronger magnetic field is required to reach the high-field regime. This shows that the wave-function in sample B, which has indium in the barriers and is grown at lower temperature, is substantially more extended than for sample A at these low temperatures. The spatial extent of the exciton wave-function is related to the exciton effective mass through the hydrogenic Bohr radius:

$$a_B = \frac{0.529\varepsilon}{\mu/m_0} \text{ [Å]} \tag{4.1}$$

where ε is the relative dielectric constant of the material, μ is the exciton effective mass and m_0 is the mass of the free electron. Thus, the prime candidate to account for the change in exciton wave-function we observe

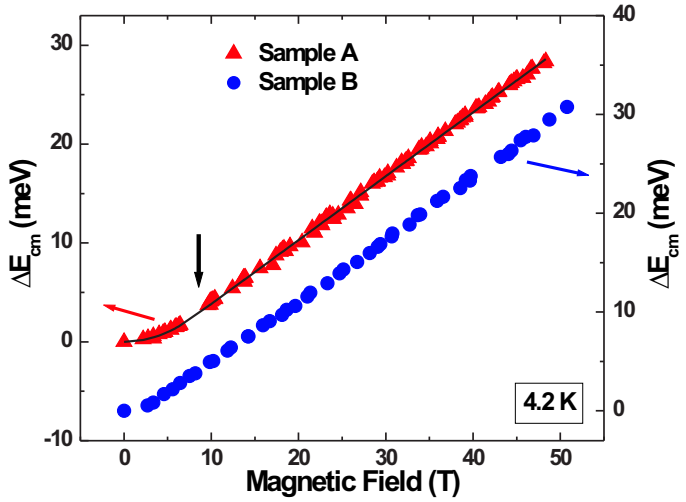

Figure 4.8: The shift of the PL centre of mass, ΔE_{cm}, versus magnetic field. The line is a fit to the data of sample A using Equation 1.19. For sample A, a crossover from parabolic to linear behavior occurs at 8.5 T (indicated by the arrow), whereas the data for sample B are linear down to very low fields.

is a decrease in μ when going from sample A to sample B. However, it can be seen in Figure 4.8 that the slope of the E_{cm} *vs.* B curve in the high field regime is very similar, and indeed an analysis of the high field data gives an exciton effective mass of $(0.090 \pm 0.005)m_0$ and $(0.0924 \pm 0.0003)m_0$ for samples A and B, respectively[4]. Hence, the change in wave-function extent derived from the difference in magneto-PL at the lowest fields cannot be explained in terms of a change in effective mass. Previous magneto-PL studies [39, 44, 54, 55] as well as our temperature dependent measurements have indicated that recombination between carriers of which at least one is localised by potential fluctuations occurs only at low temperatures ($< \pm 150$ K). Given the fact that the magneto-

[4]We note that these values agree with previously reported results for dilute nitrides, *e.g.* 0.116 m_0 by Wimbauer *et al.* [63], < 0.11 m_0 by Fritz *et al.* [64] and ~ 0.09 m_0 by Polimeni *et al.* [65].

PL experiments were performed at very low temperatures, we propose that the reduced wave-function extent measured in sample A is related to the localisation effects identified in the temperature dependence in Figure 4.4. At this stage, the data indicate that the localisation keeps the carriers further apart for sample B than for sample A.

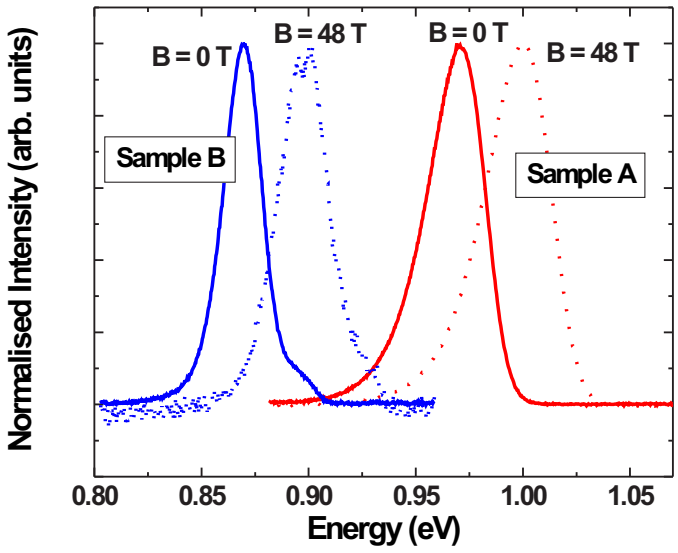

Figure 4.9: PL spectra for both samples A (red) and B (blue) at 0 (full line) and 48 T (dotted line) measured at 4.2 K. The low energy shoulder, typical for recombination from localised excitons, is present only in the data for sample A. The linewidth of the PL peak for sample B is considerably smaller.

A typical manifestation of recombination originating from localised carriers is a low-energy tail in the PL spectrum which has a longer decay time than the main PL peak [57], and is present in $Ga_{1-x}In_xN_yAs_{1-y}$ QWs [39, 42, 43, 55, 56, 66–69], as well as in a large number of other semiconductor alloys [57, 70, 71]. It can be seen in Figure 4.9 that this low-energy broadening, which is typical for localised exciton recombination, is present in the PL spectrum of sample A only, not sample B.

These observations support the idea that low growth temperatures and the incorporation of indium in the barrier material have a significant positive effect on the optical quality of $Ga_{1-x}In_xN_yAs_{1-y}$ MQW structures [41, 43]. We should note that apart from a low-energy broadening in sample A, a high-energy feature is present in the PL signal of sample B only. Very little is known up to now about its origin, but it can be seen from Figure 4.7 and Figure 4.10 that the feature does not exhibit a shift in energy as a function of excitation power or temperature, suggesting that it cannot be due to free exciton recombination. Furthermore, the shift of the high-energy feature with magnetic field as it is observed in Figure 4.9 excludes the possibility that it is a trivial artifact related to the experimental setup.

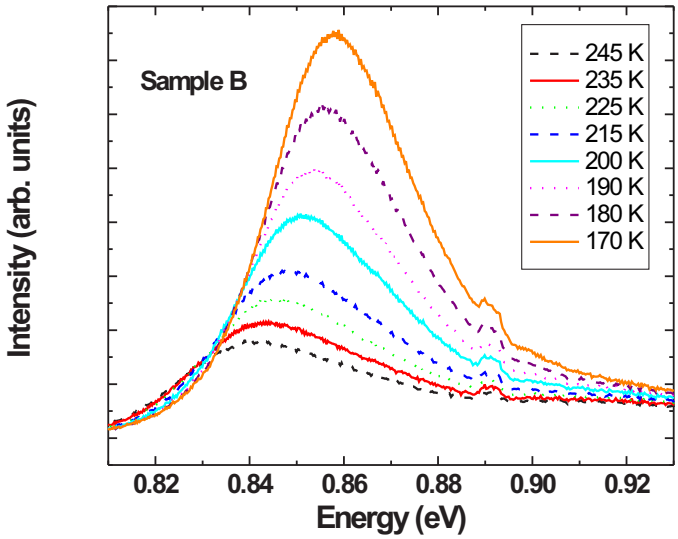

Figure 4.10: Excerpt from the temperature dependence for sample B, illustrating that the position of the high-energy feature, in contrast to the main PL peak, is not sensitive to temperature.

Finally, it can be seen from Figure 4.9 that the linewidth, measured as the full width at half maximum (FWHM) of the PL signal is

considerably larger in sample A than in sample B (32.3 and 17.9 nm, respectively). In general, the inhomogeneous broadening of the excitonic emission is a reliable parameter to qualify the degree of interface disorder in a two-dimensional system. The excitonic transitions in semiconductor multi-component alloys are considerably broader than in their respective binary constituents, and the broadening has been attributed to compositional and structural disorder on the monolayer scale, which is inevitably present in these structures [69]. Although the global composition of the alloy, averaged over the full volume, is fixed, every exciton present in the alloy will probe a different region of the structure, with its own local average composition, that varies slightly throughout the alloy. Additionally, small fluctuations in the amount of material deposited at each position on the wafer result in a position-dependent thickness profile, influencing the transition energies for recombination. The ensemble of fluctuations around a fixed composition, each with its characteristic energy transitions,[5] and the fluctuations due to structural disorder, results in the observed inhomogeneous broadening. Hence, we conclude that the improvement of the optical properties at lower growth temperatures and with indium-incorporated barriers is clearly present in our samples.

4.2.4 Temperature dependence of the magneto-PL

Although the field-dependence of sample B appears linear down to very low fields (see Figure 4.4), a small parabolic regime cannot be excluded. Moreover, the longer integration times (> 5 ms) required at higher temperatures rule out the pulsed field technique to perform magneto-PL experiments at higher temperatures on our samples. Given the low fields at which the cross-over between diamagnetic and free-carrier behaviour occurs, magneto-PL in DC fields of up to 12 T is an excellent candidate to study the carrier localisation into more detail.

From the pulsed field data we have learned that the exciton radius

[5] Within the VCA, the conduction and valence band edges probed by the exciton, and as such its transition energies, are determined by the local composition.

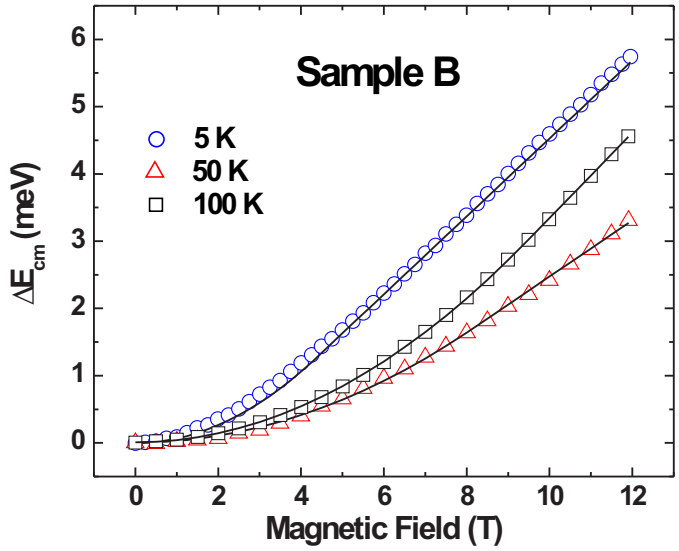

Figure 4.11: PL centre of mass energy shift as a function of DC magnetic field for sample B at 5, 50 and 100 K. In contrast to the pulsed field data, a small parabolic regime can clearly be observed. The lines are fits to the data using Equation 1.19.

at very low temperatures is substantially more extended for sample B than for sample A since we were unable to detect diamagnetic behaviour for sample B. The analysis of the PL centre of mass energy as a function of DC magnetic field however (see Figure 4.11) reveals a small parabolic regime in fields up to about 4 T at 5 K, which yields an exciton wave-function extent of 17.5 nm, which is still substantially larger than in sample A. Upon slightly increasing the temperature, the cross-over between the two regimes quickly shifts to higher fields, but does not change dramatically going from 50 to 100 K. At $T > 100$ K, the high-field limit is no longer reached at 12 T. Correspondingly, the exciton wave-function extent is characterised by a rapid decrease as a function of temperature, followed by an apparent saturation to a value around 12 nm for $T > 50$ K (see Figure 4.12), in agreement with earlier studies [54]. For sample A,

the situation is similar, but less dramatic. At low temperatures, the exciton is more compact compared to in sample B (equivalent to what was found in pulsed fields, see Section 4.2.3), and a gradual decrease toward the common value of 12 nm at 200 K is observed. The activation energy is 7.3 meV (84 K) for sample A, while it is only 2.3 meV (26 K) for sample B (see Figure 4.12).

When discussing the behaviour of the exciton radius inferred from the PL shift in magnetic field, we should bear in mind that we are measuring the average exciton radius from the entire ensemble of recombining excitons. This average depends on the relative weight of free excitons with respect to localised states, which in turn depends on the excitation power and magnetic field. Although the data-set for this analysis remains somewhat limited, we will see in the next paragraphs that our results agree very well with previous studies.

In an effort to understand the behaviour we have just observed, we will briefly discuss the influence of the growth temperature on the structural and optical quality of $Ga_{1-x}In_xN_yAs_{1-y}$ MQWs as it was studied by various groups [45, 47, 48, 50–52]. The Transmission Electron Microscopy (TEM) studies performed by Herrera *et al.* indicate that an increase in growth temperature triggers increased In/Ga interdiffusion during growth, which leads to TEM-observable composition fluctuations in the structure. For samples grown at very high temperatures (460 °C), undulations with a periodicity of 20 nm are observed using the composition-sensitive 002DF reflection. The intensity of the contrasts observed in the strain-sensitive 220BF reflection mode is drastically increased when raising the growth temperature. Since the amplitude of these stress contrasts is directly related to the FWHM of the PL peak in these samples, the TEM-observed degradation of the structural properties is at the origin of the decrease in optical quality when growing at higher temperatures. Additionally, the period of the contrasts observed in TEM is reduced when raising the growth temperature, indicating

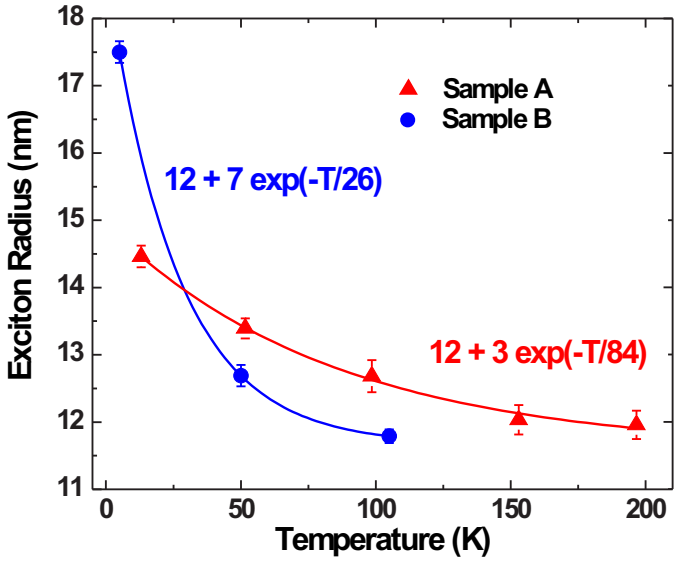

Figure 4.12: Exciton wave-function extent as a function of temperature for the DC measurements. At low temperatures, the exciton radius in sample B is larger than in sample A, but as temperature increases, the relation rapidly reverses. Errors are derived from the uncertainties on the fitting parameters in the analysis of the data using the model described in Section 1.3.2.

that the scale of the disorder is larger in the samples grown at lower temperatures.

This is entirely consistent with our results. Due to the difference in growth temperature also present in our samples, the composition modulation in sample B is reduced with respect to that of sample A, and the disorder scale in sample B is larger than in sample A. The introduction of indium in the barrier material of sample B reduces the strain at the QW/barrier interface, further lowering the inhomogeneity of the $Ga_{1-x}In_xN_yAs_{1-y}$ QWs in the sample [41, 43]. Hence, the effect of carrier localisation is expected to be much stronger in sample A, while the period of the modulation is larger in sample B. The result is that in

both samples the electrons [65, 72, 73] may be trapped by nitrogen-rich or indium-rich regions, while the holes may only be localised in In-rich parts of the sample[6], separating them from electrons in the N-rich regions. Sample B, which was grown at 325 °C , exhibits an excitonic wave-function extent at low temperatures (spatial separation of electrons and holes) that occurs on a longer length scale (∼19 nm from Figure 4.12), but is more rapidly thermally quenched, than for sample A, which was grown at 460 °C (separation of ∼15 nm). Indeed, between 5 and 50 K, the exciton wave-function extent for sample B drops by about 30 %, while it is only about 7 % for sample A, indicating that for sample B, the detrapping occurs at lower temperatures, in agreement with the zero-field PL energy dependence on T (see Figure 4.4). Thermal excitation of the holes from potential fluctuations due to local indium excess into the continuum shifts the nature of the dominant recombination from spatially indirect at low temperature to direct, hence reducing the exciton radius (see Figure 4.12). At even higher temperatures, the PL signal is dominated by recombination from free excitons, and the exciton wave-function extent saturates.

On these grounds and from the observed activation and PL energies, we can then proceed to construct a phenomenological description of the potential landscape in our samples as shown in Figure 4.13. Zero-field PL energies at low temperatures provide a lower limit for the direct transitions between indium-induced potential fluctuations, while we can estimate the transition energy between electrons localised in nitrogen-rich regions and free holes from the local minima in the sigmoidal T-dependence of the PL energy. By extrapolating the band-gap behaviour observed at high T toward 0 K, we estimate the band-gap for free excitons, which amounts to 994 and 880 meV for sample A and B, respectively. The energy difference between this extrapolation and the observed recombination energy at the local minimum of the sigmoidal

[6]The introduction of nitrogen into the GaInAs material affects mostly the conduction band, and has negligible effect on the electronic structure of the valence band [37]. Hence there exist no nitrogen-induced potential fluctuations in the valence band.

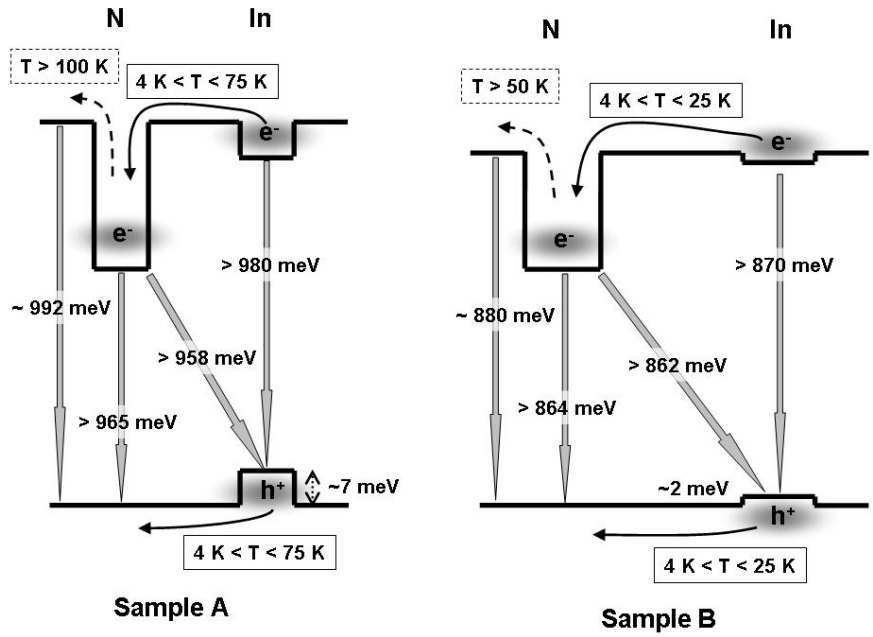

Figure 4.13: Schematic representation of the potential landscape based on our observations. Recombination energies in the figure are derived from PL centre of mass transition energies, and are approximate. The average separation of N-rich and In-rich regions is estimated from our data as being 15 nm for sample A and 19 nm for sample B.

zero-field T-dependence of E_{cm} gives a rough estimate of the electron localisation energy in nitrogen localisation centres. The result is that from our estimations, the localisation energies for the electrons in nitrogen-rich regions are about 21 and 13 meV, while for the indium fluctuations they amount to about 7 and 2 meV (for electrons and holes) for sample A and B, respectively[7]. Thus the localisation energies are about twice as strong for sample A as compared to sample B. This is further supported by the behaviour of the data of Figure 4.4, where the temperatures of the

[7]We emphasise that the activation energies for the holes in indium fluctuations are derived from exponential fits to a few data points, and hence should be considered as rough estimates.

maxima and minima also differ by a factor of two for the two samples.

4.3 Application: GaInNAs laser diodes operating at 1.5 μm

The main reason for the recent interest in the $Ga_{1-x}In_xN_yAs_{1-y}$ material is its potential as active material in long-wavelength telecommunication lasers. Since the group of A. Forchel from the University of Würzburg announced the first GaAs-based laser emitter in the 1.5 μm range using $Ga_{1-x}In_xN_yAs_{1-y}$ QWs in 2000 [74], a number of approaches have been followed in order to reduce the threshold current densities. The use of $GaAs_{1-y}N_y$ strain compensating layers between the QW and the GaAs barriers [75], low substrate temperatures and low V/III ratios during growth [76] and the addition of antimony to the QW [77,78] all result in the realisation of multi-mode continuous-wave emitting devices. However, single-mode emission is required for telecom applications, and only recently room-temperature single-mode continuous-wave operation of a GaAs-based laser diode at 1.5 μm without the need for antimony has been demonstrated [79]. Here, rapid thermal annealing at 700 °C in a mixture of 95 % argon and 5 % hydrogen drastically improved the optical quality of the structures, and PL intensity measurements as a function of annealing time showed that an 8 min anneal produced the best results. Although these results clearly show the potential of antimony-free $Ga_{1-x}In_xN_yAs_{1-y}$ QW laser diodes for continuous-wave and single-mode laser applications in the 1.5 μm wavelength range, a detailed understanding of the mechanisms at work when growing $Ga_{1-x}In_xN_yAs_{1-y}$ laser structures is crucial for future device fabrication, *e.g.* in order to extend the operation to temperatures above room temperatures, as is needed in real device applications.

4.4 Conclusions

We have investigated the behavior of the excitonic emission for two $Ga_{1-x}In_xN_yAs_{1-y}$ MQW samples under the application of a strong magnetic field and have acquired a better microscopic picture of the localisation effects that are known to be present in these samples. All our observations confirm that the addition of a small percentage (2.3%) of indium to the barrier material and the lowering of the growth temperature from 460°C to 325°C in sample B induces a considerable enhancement of the optical quality of the structure. The nonmonotonic temperature dependence of the PL energy is much weaker and occurs at a lower temperature for the higher quality sample, while magneto-PL experiments evidence an increased electron-hole separation at low temperatures, consistent with TEM experiments on similar samples. Thermal quenching of the exciton radius, as observed in the temperature-dependent magneto-PL, is attributed to redistribution of the holes from regions with indium-induced local potential minima into the continuum, allowing them to move to regions where electrons are trapped by an excess of nitrogen. As T is further increased, the electrons become free as well, and the PL is dominated by free-carrier recombination. The situation is similar for both samples, but is less dramatic and occurs on a longer length scale for sample B, which was grown at lower temperature and with strain-relieving indium incorporation in the barrier material. An assessment of the potential profiles for both samples from our data leads to the conclusion that the localisation energies are reduced by about a factor of two in sample B. This assertion is further endorsed by the observation that for the low quality sample only, an excitation power dependence of the PL signal is found.

Chapter 5

Strain-engineered InAs/InGaAs/GaAs quantum dots

As we pointed out in the Introduction, the metamorphic growth of self-assembled InAs/GaAs QDs is a valuable approach for reaching long-wavelength emission for telecommunication applications. The use of an adjustable intermediate layer between the substrate and the QDs enables to control the emission energy of the InAs QDs at will (within certain limitations). In this Chapter, we will discuss exciton confinement as studied by magneto-PL on a series of stain-engineered InAs/InGaAs/GaAs QDs.

5.1 Strain-engineered quantum dots

5.1.1 Long-wavelength emission

For the achievement of long-wavelength emission (at 1.3 or 1.55 μm, the wavelengths of interest for telecommunication applications), the use of GaAs-based materials is preferred over InP substrates due to *e.g.* the lower cost and increased compatibility with current micro-electronic

industries (see Introduction). Although the band-gap of bulk InAs is only 0.417 eV at 0 K [21], confinement effects blue shift the energy to values exceeding the aforementioned telecommunication wavelengths when growing QD nanostructures. There is a 7 % lattice mismatch between the InAs and GaAs semiconductor crystals, requiring modifications to the InAs/GaAs QD structure in order to reach emission at 1.3 or 1.55 μm. A number of methods to red shift the emission wavelength of InAs QDs has been put forward, which can roughly be categorised into two areas related to:

- The increase of the QD dimensions to reduce the quantum confinement effect [80–83], and

- A reduction of the strain and band-offsets between the QD and surrounding material

Reaching 1.55 μm emission following the first approach is considered a hard task since the QD size is limited by the intrinsic strain of the InAs/GaAs system, and extremely low growth rates (as low as 0.003 ML/s) are insuperable [81, 84].

The second approach is based on the use of a metamorphic buffer or confining layer with a band-gap that is still wider than for InAs, but narrower than for GaAs, thereby providing an intermediate 'step' between the InAs and GaAs. The result is that the strain between the QD and the matrix material is relieved, and that the QDs are surrounded by a lower band-gap material compared to GaAs[1]. Materials used to serve as metamorphic buffer layer include AlGaAsSb [87, 88], GaAsSb [89, 90] and an InGaAs cap layer [85, 86, 91] or confining layers [92–98], the last of which will be the topic of this Chapter.

[1] We note that some authors have proposed that aside from the reduction in strain and band discontinuities, increased QD dimensions and/or a changed QD composition due to strain-driven indium migration toward the QDs may also enhance the red shift when overgrowing InAs QDs with an $In_xGa_{1-x}As$ cap layer [85, 86].

5.1.2 Strain-engineering principle

Strain-engineered QDs are grown between $In_xGa_{1-x}As$ metamorphic confining layers, that are optimised to control the optical properties of the QDs at will. In these materials, there exist two independent parameters that can be tuned to achieve emission at the desired wavelength at room temperature.

First, the indium incorporation in the *lower confining layer* (LCL) and *upper confining layer* (UCL) can be varied, which has a direct effect on the band discontinuities between the QDs and the confining layers. A decrease in the band discontinuities lowers the confinement potentials for the carriers in the dots, and the emission shifts to lower energy. Since *Atomic Force Microscopy* (AFM) measurements have shown that a dramatic increase of the QD diameter occurs at indium concentrations exceeding 33 %, the indium molar fraction x (hereafter termed as composition x) was kept at values between 0 and 0.33, keeping the QD diameters almost constant [98].

Second, the thickness d of the LCL determines the amount of residual strain within the LCL, and hence influences the mismatch at the QD-LCL interface. As a result, the QD strain can be modified by tuning the thickness of the LCL, which acts as a metamorphic buffer [99]. However, a careful selection of the LCL thickness is required, since the lattice parameter of an $In_xGa_{1-x}As$ layer grown on top of a GaAs substrate equals that of the GaAs in the pseudomorphic regime, which persists up to thicknesses below the so-called critical thickness t_c [98,100], which is strongly dependent on the amount of indium in the confining layers. For an indium concentration of 15 % it is about 43 nm, while for 18 % indium incorporation t_c is about 25 nm. Beyond this critical thickness, the elastic strain is partially relaxed and the formation of a network of misfit dislocations takes place [101]. Therefore, only thicknesses $> t_c$ should be used.

These considerations indicate that a cautious control of both parameters enables the reduction of the strain in the QDs and the band

discontinuities between the confining layers and the QDs to produce GaAs-based nanostructures that emit at the desired wavelength at room temperature.

5.2 Sample Characterisation

The structures considered in this Chapter were provided by Dr. L. Seravalli from the CNR-IMEM institute in Parma, Italy. On top of a semi-insulating (100) GaAs substrate, a 100 nm thick GaAs buffer layer was deposited. Subsequently, an $In_xGa_{1-x}As$ metamorphic LCL of thickness d was grown at 490°C. After a growth interruption of 210 s to lower the substrate temperature, InAs QDs with a 3 ML coverage were deposited by *Atomic Layer MBE* (ALMBE)[2] at 460°C. Finally, the structure was capped with a 20 nm-thick $In_xGa_{1-x}As$ UCL with the same composition as the LCL and deposited by ALMBE at 360°C[3]. A schematic representation of the sample morphology is given in Figure 5.1.

A total of seven samples was studied, of which three are designed to emit at 1.3 μm, three to emit at 1.4 μm, and a final sample is engineered to emit at 1.5 μm at room temperature. The lattice mismatch (and hence the strain on the QDs) and the band discontinuities are different for all seven samples. Table 5.1 summarises the engineered parameters used to obtain the desired room-temperature emission.

AFM characterisation was used to determine the QD dimensions, and a typical AFM image is shown in Figure 5.2. Since AFM measurements are only possible on uncapped samples, an image from a sample with the exact same growth parameters as one of the studied samples (i1337) has been chosen. Although the image is a good representation

[2] ALMBE is a variant of MBE where group-III and group-V species impinge on the substrate alternatively in monolayer or submonolayer amounts per cycle. It is generally used to obtain larger dots, but without the QDs coalescing into non-coherent structures, a common problem when growing at relatively high coverages [98, 102].

[3] A lower growth temperature for the UCL was chosen to reduce the interaction between confining layers and QDs [94].

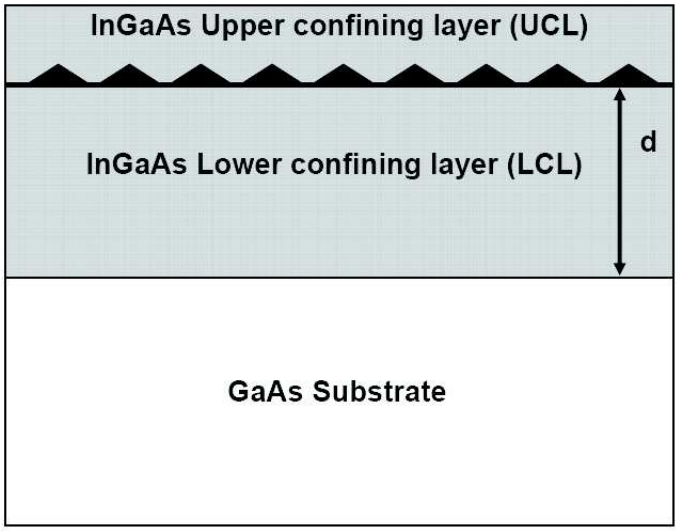

Figure 5.1: Schematic representation of the sample structure. The InAs QDs are grown between an upper confining layer of fixed thickness (20 nm) and a lower confining layer of variable thickness *d*, both with the same composition. The 3 ML-thick InAs QD coverage is indicated by the triangles.

of the samples in the present work, we need to stress that capping of the QDs with the UCL may influence the QD characteristics [98, 99, 101]. However, from statistical treatment of a large number of AFM results, and taking into account various corrections such as baseline adjustment and tip-sample convolution, an average QD diameter of (21 ± 4 nm) and height of (4 ± 1 nm) has been determined[4].

[4]As mentioned in Section 5.1.2, indium concentrations larger than 33 % in the confining layers alter the QD dimensions, and hence these values are valid for samples with lower indium incorporation only. Table 5.1 shows that all our samples fall within that limit, and hence the mentioned QD dimensions are applicable for all the samples in the present work.

Table 5.1: Summary of the growth parameters for the samples under investigation. The concentration x of indium in the LCL (and UCL) and the thickness d of the LCL (along with the resulting lattice mismatch f at the QD/CL interface).

	Sample Name	LCL In Concentration x	LCL Thickness d (nm)	Lattice Mismatch f (%)
1.3 μm	i1341	0.09	1000	6.74
	i1339	0.12	165	6.84
	i1337	0.18	31	7.08
1.4 μm	i1345	0.24	145	5.92
	i1347	0.28	37	6.14
	i1349	0.31	19	6.32
1.5 μm	i1272	0.31	1000	5.04

5.3 Exciton confinement in strain-engineered InAs QDs

The reduction of the QD strain and band discontinuities lowers the band-gap of the InAs QDs enabling long-wavelength luminescence, at the expense of decreasing carrier confinement in the dots, which is a disadvantage for device fabrication. In the present work, we will use magneto-PL to study the lateral exciton confinement in these strain-engineered structures.

5.3.1 Experimental results

PL experiments in high magnetic fields at 4.2 K were carried out for all seven samples. Raw spectra for three typical samples, selected from the sets optimised for emission at 1.3, 1.4 and 1.5 μm (see Table 5.1), are

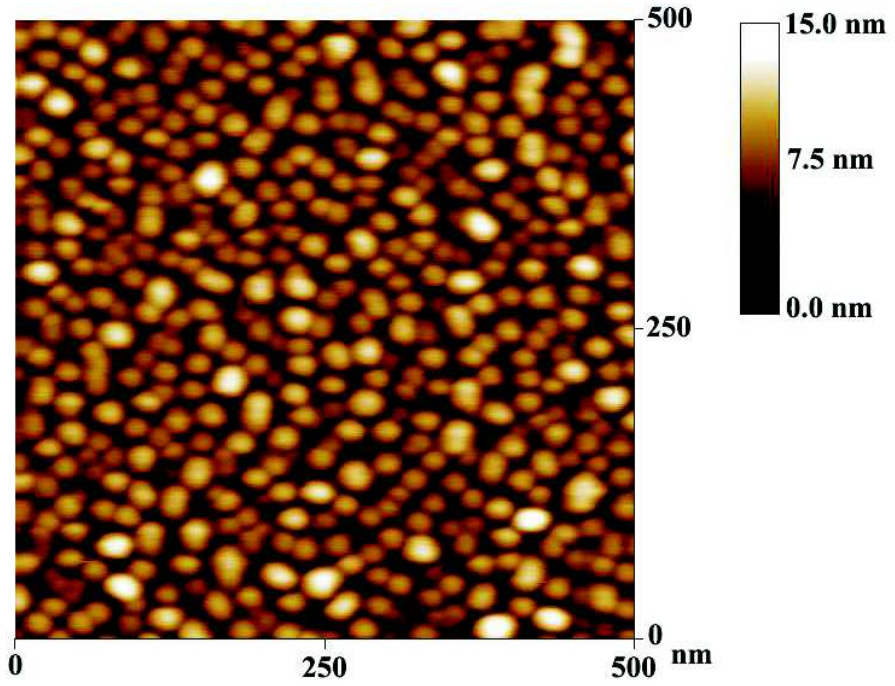

Figure 5.2: AFM image of sample i1338, which has the same parameters as sample i1337. A large majority of the QDs shows heights of about 7-8 nm and diameters slightly larger than 20 nm. Statistical analysis on a large number of AFM results and baseline and tip-sample convolution corrections leads to an average diameter of (21 ± 4 nm) and height of (4 ± 1 nm).

shown in Figure 5.3, illustrating the decrease in emission energy[5]. Although in this plot, the intensity is normalised to facilitate a comparison between the emission energies, we note that the absolute intensity of the signal from sample i1345 is about a factor of 5 lower than for sample i1341, while the intensity decreases again with a factor of about 6 going from sample i1345 to sample i1272.

Figure 5.4 shows the PL energy shift ΔE_{cm} as a function of magnetic

[5]The emission energies at low temperatures deviate from the desired values at room-temperature due to temperature effects, see Section 3.2.1

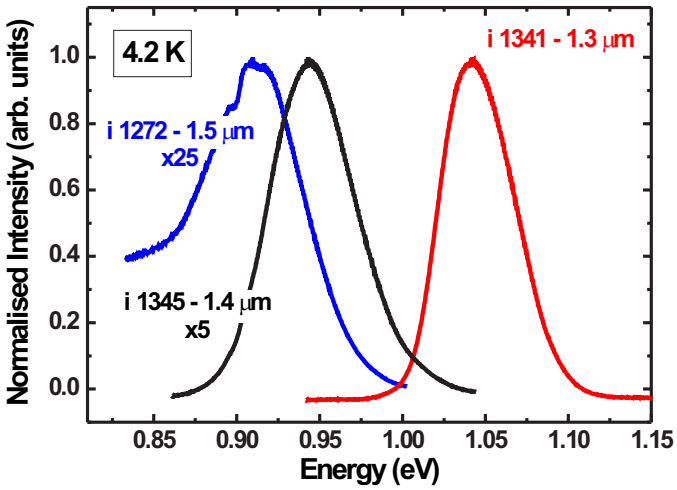

Figure 5.3: PL spectra for three typical samples, chosen from the sets designed to emit at 1.3, 1.4 and 1.5 μm. The intended decrease in emission energy is clearly present in our samples.

field for the same three typical samples. For sample i1272, the luminescence is very weak, and the measurements at low fields were performed in DC fields, to provide longer integration times (see Section 2.4).

When going from sample i1341 (1.3 μm) to i1345 (1.4 μm), the PL energy shift between 0 and 45 T increases by about 5 meV. An analysis of the data using the model described in Section 1.3.2 reveals that the larger energy shift reflects a decrease of the exciton effective mass μ from 0.086 $\pm$ 0.001 to 0.076 $\pm$ 0.003 m_0. Correspondingly, the exciton effective radius $\langle\rho^2\rangle^{\frac{1}{2}}$ increases from 7.06 $\pm$ 0.02 to 8.2 $\pm$ 0.1 nm, or by about 16 %. Since the relation between the exciton mass and the exciton *bulk* radius (*i.e.* in the absence of confinement) is given by:

$$a_B = \frac{0.529\varepsilon}{\mu/m_0}\mathring{\mathrm{A}} \tag{5.1}$$

where ε=14.6 is the relative dielectric constant for InAs and μ is the

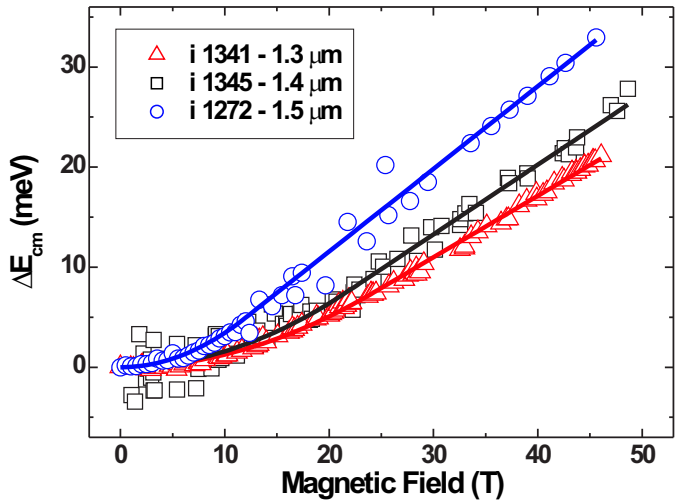

Figure 5.4: Shift of the PL energy as a function of magnetic field for three typical samples, chosen from the sets designed to emit at 1.3, 1.4 and 1.5 μm. For the longer wavelength sample, a combination of pulsed and DC fields has been used.

exciton effective mass, we are able to evaluate the observed increase in exciton extent with respect to the increase in *bulk* radius an exciton with the *measured* mass would have in the absence of lateral confinement. Following this reasoning, the observed decrease in exciton mass from 0.086 ± 0.001 to 0.076 ± 0.003 m_0 would be accompanied by an increase in *unrestricted* exciton radius from 8.98 ± 0.09 to 10.2 ± 0.3 nm, or by about 13 %. Hence the observed expansion of the exciton radius lies within the expectations of the hydrogen model.

The changes for the third sample, i1272 (1.5 μm), are more remarkable. There is a considerable enhancement of the PL energy shift with field, testifying of a decrease of μ from 0.076 ± 0.003 to 0.067 ± 0.008 m_0. The wave-function extent however increases from 8.2 ± 0.1 to 10.6 ± 0.5 nm, or by about 29 %, while the hydrogen model predicts an increase from 10.2 ± 0.3 to 12 ± 1 nm, or only by about 13 %. This

cannot be explained by an increase in the QD dimensions, since AFM experiments have shown that changes in the QD diameter only occur for indium concentrations > 33 %. Additionally, Figure 5.5 shows that the application of a magnetic field of 45 T enhances the PL spectrum by about a factor of 10, while it is only a factor between two and three for the other samples.

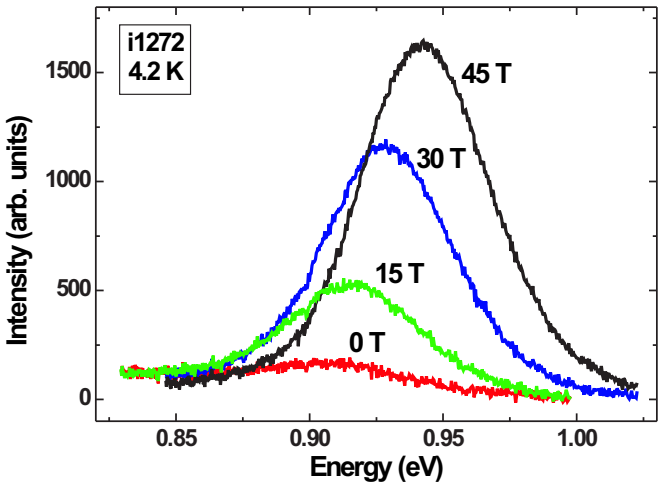

Figure 5.5: PL spectra for sample i1272 at different magnetic fields. At 45 T, the PL intensity is increased by a factor of 10 with respect to the zero-field signal.

Therefore, at this stage the data indicate that the red shift of the PL emission as accomplished by a reduction of the QD band discontinuities and strain, is accompanied by an increase in wave-function extent that is increasingly important at longer wavelengths, a result that is not very surprising considering that the optimisations to reach longer wavelengths essentially reduce the QD band-gap but also weaken the confinement potentials.

Increased lateral confinement

However, the scale of the dramatic changes in confinement becomes more evident when we examine the behaviour of the exciton wave-function extent for all seven samples. The results for all samples, retrieved from a similar analysis as in the previous Section, are summarised in Table 5.2. The table also includes the electron[6] activation energies E_A, as calculated in a single-particle effective mass approximation, for each sample.

In order to consistently characterise the amount of confinement, we have normalised the measured exciton wave-function extent in the plane of the sample by the *bulk* exciton radius. The ratio a_B^0 between the actual measured wave-function extent and the bulk Bohr radius is a measure of the amount of exciton confinement in the structure. A small ratio indicates strong confinement as the exciton cannot occupy the space it would in bulk material, while a value close to 1 suggests very little influence of confinement on the spatial extent of the exciton.

Figure 5.6 shows the dependence of a_B^0 on the electron activation energy for all seven samples. It can be seen that for the 1.3 μm set, which is characterised by high activation energies, there is little change in the normalised exciton radius. For $E_A < 60$ meV however, the region where the samples for the 1.4 μm set are situated, a sudden decrease of a_B^0 with decreasing activation energy reveals an increase in lateral confinement. While the QD strain and band discontinuities are lowered to reach longer wavelengths, the mass of the exciton decreases and its wave-function tends to expand, but is hampered by the spatial limitations of the quantum box it is confined to.

However, it is clear that at a certain stage the decreasing QD confining potentials will no longer be capable of retaining an expanding exciton wave-function, and this is the case for the 1.5 μm sample. Here, a normalised exciton radius of about 0.92 ± 0.09 is found, indicating

[6]Like in GaAs (see Section 3.2.5), the electron effective mass in InAs is much smaller than the hole effective mass. Hence, to a good approximation, the exciton effective mass is about the same as the electron effective mass, and the electron is the relevant carrier to discuss the confinement.

Table 5.2: Experimental results for all seven samples under consideration. The bulk exciton radius is the calculated Bohr radius using the measured effective mass μ. Errors are derived from the uncertainties on the fitting parameters in the analysis of the data using the model described in Section 1.3.2.

	1.3 μm			*1.4 μm*			*1.5 μm*
Sample Name	1341	1339	1337	1345	1347	1349	1272
LCL In Concentration x	0.09	0.12	0.18	0.24	0.28	0.31	0.31
LCL Thickness d (nm)	1000	165	31	145	37	19	1000
Lattice Mismatch f (%)	6.74	6.84	7.08	5.92	6.14	6.32	5.04
Electron Act. Energy (meV)	146.38	135.74	113.75	62.94	53.09	45.92	26.89
PL Energy Shift ΔE_{cm} (meV)	26.04	24.79	25.66	30.66	33.48	48.57	33.52
Exciton Mass μ (m_0)	0.086 ± 0.001	0.083 ± 0.001	0.085 ± 0.001	0.076 ± 0.003	0.070 ± 0.002	0.051 ± 0.006	0.067 ± 0.008
Exciton Radius $\sqrt{\langle\rho^2\rangle}$ (nm)	7.06 ± 0.02	7.28 ± 0.04	7.26 ± 0.04	8.2 ± 0.1	8.21 ± 0.07	9.7 ± 0.5	10.6 ± 0.5
Bulk Exciton Radius (nm)	8.98 ± 0.09	9.31 ± 0.08	9.09 ± 0.08	10.2 ± 0.3	11.0 ± 0.2	15 ± 1	12 ± 1

that the actual wave-function extent differs very little from its value in bulk material. In this sample, the size of the potential barriers provided by the QD has become so small that it cannot overcome the increase in exciton radius. Further evidence for this comes from the observation that in this sample only, the application of a strong magnetic field enhances the PL intensity by a factor of 10 (see Figure 5.5).

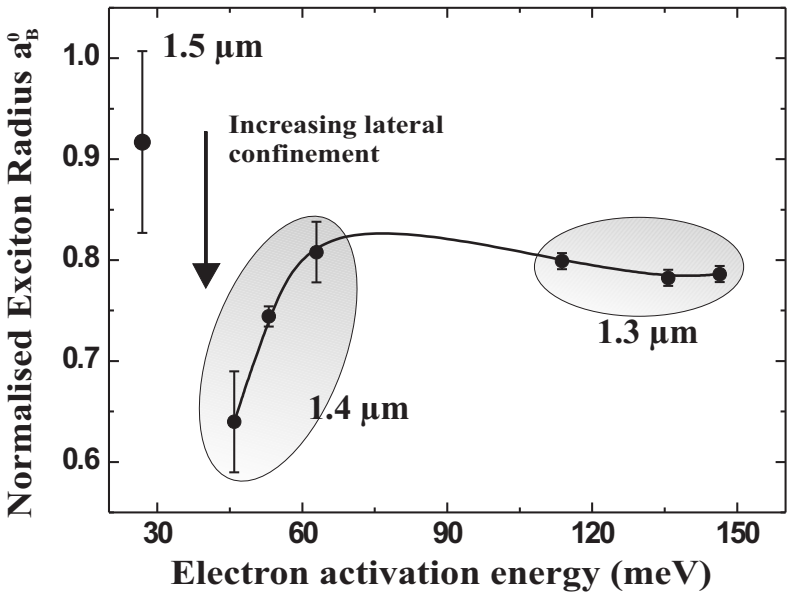

Figure 5.6: Plot of the ratio a_B^0 between the measured lateral exciton wave-function extent and expected bulk radius for the measured mass versus calculated electron activation energy. The lines are guides for the eyes.

5.4 Conclusions

We have studied the exciton confinement in strain-engineered InAs QDs designed to emit at long wavelengths at room temperature. An analysis of the normalised exciton radius reveals an increased importance of lateral confinement when the QD strain and band discontinuities are lowered to reach longer wavelength emission. The process of squeezing a progressively larger exciton in an increasingly shallower quantum box eventually leads to the escape of the exciton from the QD, and the exciton wave-function extent approaches the bulk value for the longest wavelength sample. This assertion is corroborated by the observation that in this sample only, a strong magnetic field enhances the PL signal by a factor of 10.

Chapter 6

Development and implementation of an Optically Detected Magnetic Resonance system in pulsed fields

In this chapter we will illustrate the development, construction and implementation of a new piece of equipment to enable the detection of changes in the PL induced by magnetic resonance in pulsed fields. The system was developed and assembled at our Pulsed Field facility at the KULeuven in the framework of the European EuroMagNET project, and has recently been installed at the Laboratoire National des Champs Magnétiques Pulsés (LNCMP) in Toulouse, France.

6.1 Basic principles

Optically Detected Magnetic Resonance (ODMR) is a sensitive double resonance technique in which transitions between split sublevels are de-

tected by optical means. The first experiment involving the new double resonance method was used to study the $^3P_1$ state of gas phase mercury atoms [103], and since then a number of variants of the technique has been used, *e.g.* ADMR (involving absorption), DFDMR (delayed fluorescence), FDMR (fluorescence) and PDMR (phosphorescence).

The basic idea behind the technique [104] is that the moment at which an optical excitation at fixed energy is resonant with a field-induced energy splitting, can be optically detected. The application of a variable external magnetic field will lift the degeneracy of certain electronic energy levels (such as Landau levels or spin levels) and will create a splitting that is dependent on the strength of the magnetic field. Simultaneously, the sample is excited by a microwave source or infrared laser at a fixed energy. When the energy splitting induced by the magnetic field equals the optical excitation energy, resonance occurs and the distribution of carriers among the split energy levels is altered. Since for instance the PL signal following above-band-gap excitation is strongly dependent on this distribution (*e.g.* at resonance non-emitting states are converted to emitting states), the resonance can be optically detected. While conventional resonance techniques like *e.g.* Electron Spin Resonance [105] are the natural choice for the study of paramagnetic defects, advantages of ODMR may include its sensitivity since it shifts the detection into the visible or near-infrared, enabling the study of thin-layer structures where transmission experiments would be very challenging [106–108], and the fact that the information is specific to the particular part of the light-emission process that is monitored.

Novelty

The strength of the novel equipment is that it enables infrared (IR) spectroscopy on very dilute materials, like QDs or QWs, for which the absorption is very low, and thus traditional IR absorption/transmission is very tedious given the timescales available in pulsed fields. However, since such structures show very bright PL, ODMR is an excellent choice.

The newly designed equipment allows, for the very first time, ODMR experiments in pulsed magnetic fields and enables simultaneous detection of the PL emission above the sample and FIR transmission behind the sample. The system is entirely fibre-based and is designed to achieve maximal sensitivity given the short integration times in pulsed fields.

6.2 Development and Construction

Following discussions with the partners from Toulouse, the design for a sample stick with conical fibre arrangement (see Figure 6.1) was agreed on, and the technical drawings were made at the KULeuven.

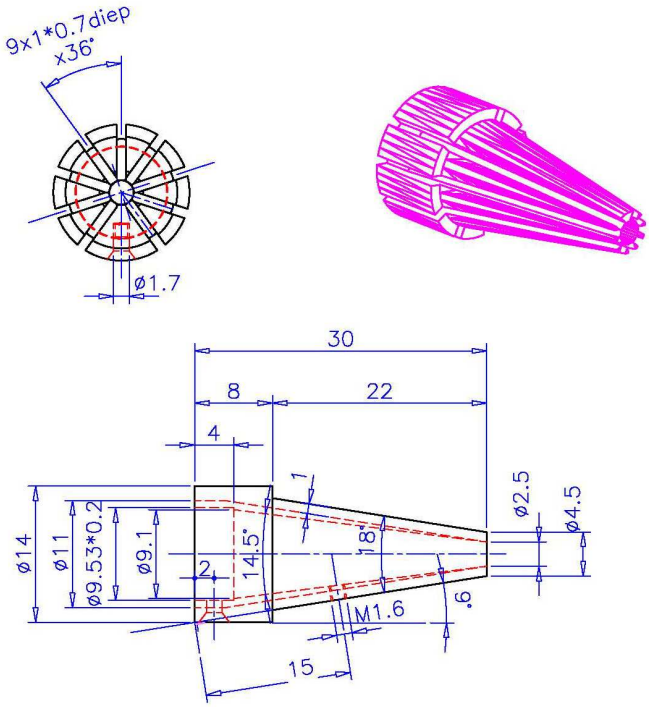

Figure 6.1: Technical drawing of the conical piece designed to guide the excitation and detection fibres toward the sample, and to focus the IR excitation onto the sample surface.

For the purpose of performing ODMR experiments in pulsed fields, a sample stick with a diameter no larger than 19.4 mm (the inner diameter of the bore of the pulsed field coils at the LNCMP) needs to be constructed. Within this very small volume, several components need to be integrated, such as an arrangement for the excitation and detection fibres, a sample mounting system, a heating wire and calibrated diode for temperature control, a pick-up coil for field detection, and a detector for simultaneous detection of the IR transmission. Hence the dimensions of these components are very small, and a larger prototype of some of the key parts was made.

Figure 6.2: Prototype for the conical guiding piece.

Figure 6.2 shows an aluminium copy of the central part which guides the optical fibres toward the sample surface. Using a rudimentary setup, the conical fibre arrangement was tested and considered successful, following which the design was approved to be implemented in the ODMR sample stick.

Figure 6.3 shows the entire sample stick at the final stage of the design with numbering of the constituent components:

1. The cover flange for the sample stick housing is made out of aluminium and has 12 BNC terminals for connection of the electronic equipment.

2, 3. An adjustable brass and O-ring sealing system that allows vacuum in the entire housing of the sample stick. The inner sample stick tube (**12**) is fully adjustable to enable careful positioning of the sample with respect to the centre of the magnetic field.

4, 5, 6. The aluminium housing of the sample stick is designed to allow sufficient bend radius for the optical fibres and the connections of the two outer stainless steel tubes of the stick are made airtight.

7. The conical fibre guide focuses the excitation and collection fibres as well as the IR excitation onto the sample surface. It is designed to hold one excitation fibre and eight collection fibres of 500 μm. Although the use of conducting material should be avoided in pulsed fields, the conical component was made out of brass since the small dimensions made the use of synthetic material too difficult.

8. The peek holder for the conical guiding piece connects the inner part of the sample stick with the sample mount (**9**).

9. Peek sample holder with interchangeable, perforated polyethylene (PE) discs to support the sample. The distance between the fibre terminals and the sample surface is fully adjustable between 0 and 8 mm.

10. Stainless steel mounting for the detector for IR transmission measurements. Since the detector cannot operate in high fields, it is mounted at a distance of 650 mm below the sample.

11. Two NW 40 connections for pumping and flushing of the entire sample stick interior.

12. Brass sealing piece with ZnSe or PE window for IR transmission attached to the inner stainless steel tube.

13. Stainless steel tube to connect the sample mounting with the detector mount.

14. Aluminium vacuum seal for the outer sample stick tube.

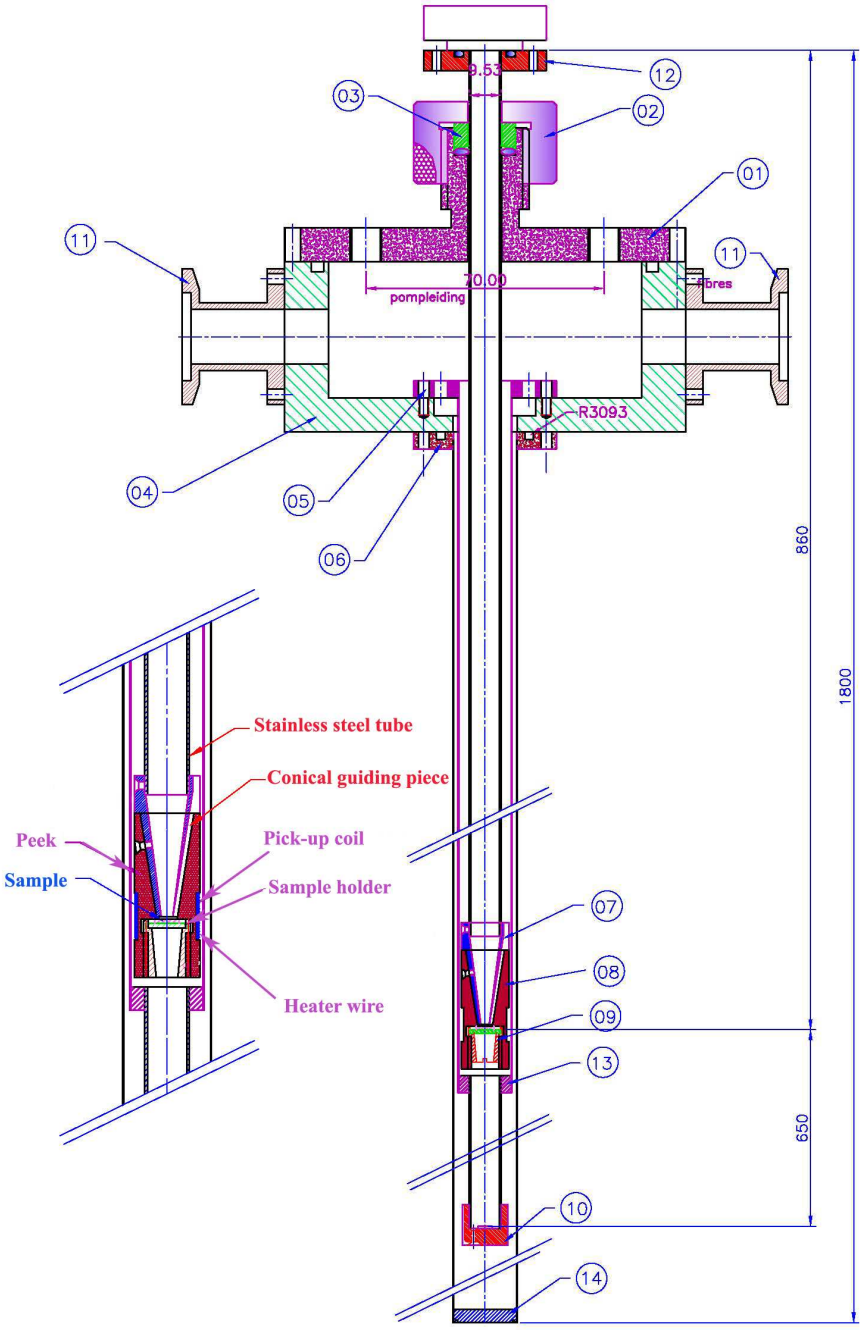

Figure 6.3: Technical drawing of the complete sample stick, with an enlarged view of the sample location in the inset. References to the indicated numbers are given in the text. Scales are in mm.

Figure 6.4 shows detailed photographs of some of the components described above.

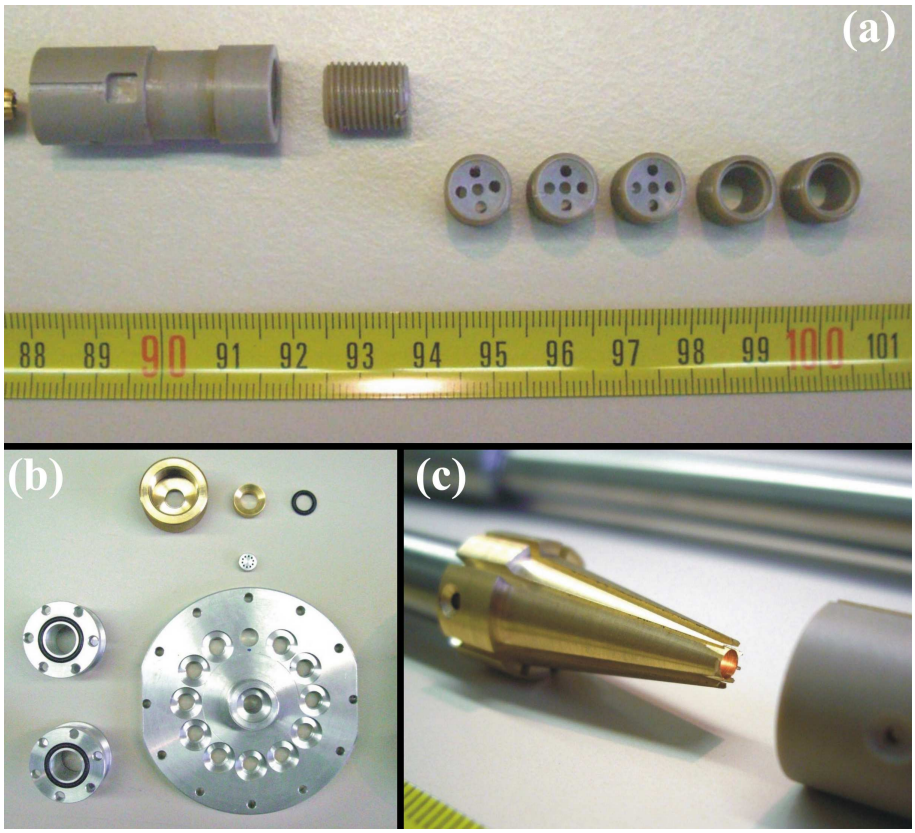

Figure 6.4: Detailed photographs of (a) the sample holder (**9** in Figure 6.3) and conical holder piece (**8**), (b) the sample stick housing cover flange (**1**), sealing system (**2**,**3**) and NW 40 connectors (**11**), and (c) the fibre guiding component (**7**).

6.3 Implementation and first results

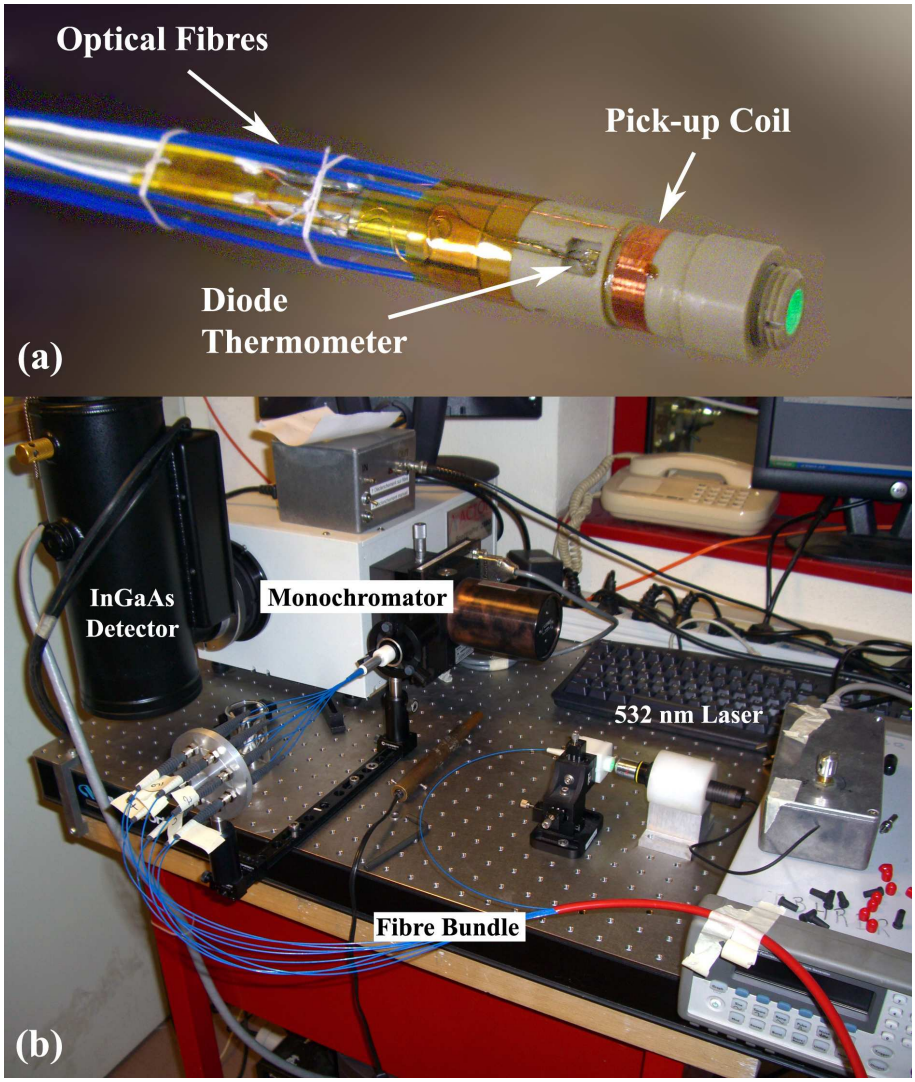

Figure 6.5: (a) Sample location for the finished ODMR sample stick. Arrows indicate the excitation and collection fibres, the pick-up coil and the diode thermometer. The heater wire was wound below the pick-up coil. (b) Detector-end of the ODMR installation. A small 532 nm green laser is exciting the test sample, while the collected PL signal from the eight collection fibres is focused onto the aperture of the monochromator which is connected to an InGaAs diode array detector.

After the sample stick was fully assembled, it was installed at the pulsed field facility of the LNCMP in Toulouse. Here, the 10 m fibre bundle was connected to the sample stick, and the diode thermometer, pick-up coil, IR detector and heater wire were installed (see panel (a) of Figure 6.5). Via a lens the PL signal from the eight collection fibres was focused onto the aperture of the monochromator which was connected to an InGaAs diode array detector (see panel (b) of Figure 6.5).

Preliminary results

As was discussed in Section 6.1, the aim of an ODMR experiment is to detect the changes induced by the IR or microwave excitation by optical means, *i.e.* by comparing the PL signal with and without IR or microwave excitation. This requires either a modulated source or a set of data with and without resonant excitation at corresponding magnetic fields. For the purpose of demonstrating that the newly installed system is fully operational, a simpler test-setup was used. Hence the following description of preliminary results does not depict an actual ODMR experiment, but merely illustrates the functionality of the new equipment.

A few test measurements were carried out on a single 100 μm thick InSe bulk layer under excitation at 118 μm from a far-IR cavity pumped by a CO_2 laser with an excitation power between 1 and 10 mW. The experiment was done at 4.2 K and the PL signal during the 300 ms downsweep of a 32 T pulse was recorded at 7 ms intervals. The PL was excited with a 532 nm laser line at 200 mW, and the resonance was recorded as the voltage across the detector behind the sample (**10** in Figure 6.3).

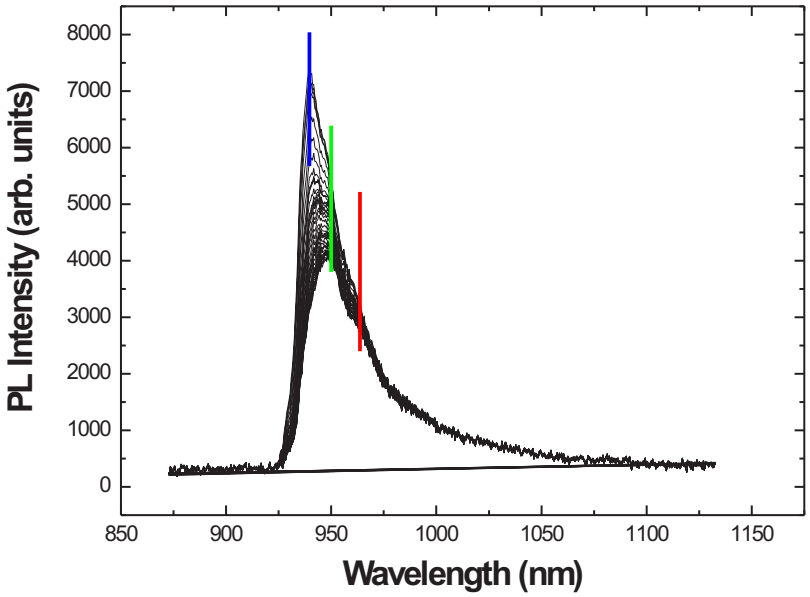

Figure 6.6: PL spectra of the InSe test sample at 7 ms intervals from 32 to 0 T. The decay of the PL intensity is studied at three different wavelengths as indicated by the full vertical lines: 940, 950 and 964 nm.

Figure 6.6 shows PL spectra at 7 ms intervals[1], and the decay of the PL signal with magnetic field is studied at three different wavelengths, namely 940, 950 and 964 nm. Figure 6.7 shows the behaviour of the PL intensity along with the resonance signal from the transmission detector.

The resonances which are know to be present in these InSe thin films are clearly visible, but an optical response seems to be absent in this sample. It is important to stress that although these measurements do not evidence an optical detection of the magnetic resonance, the full

[1]Due to a lack of calibration of the pick-up coil, the exact value of the magnetic field was not know at the time of the experiment, but acquisition started at the peak of the pulse and was recorded for 300 ms, up to the moment where the magnetic field equals zero.

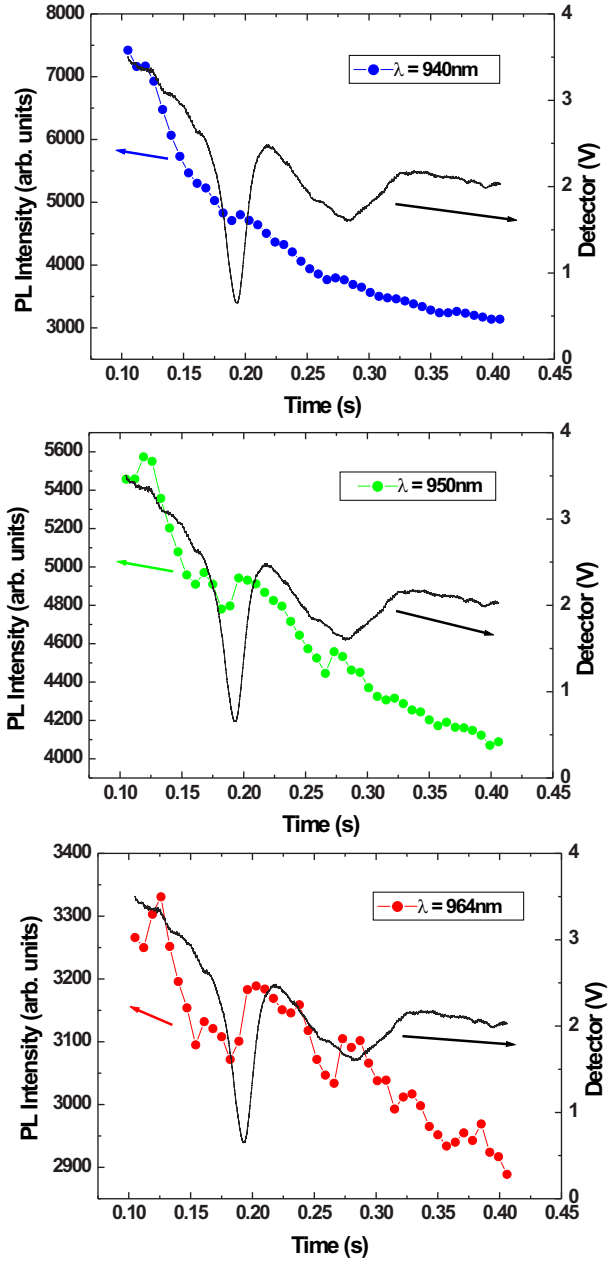

Figure 6.7: PL and resonance signal versus time. Although clear resonances are observed, the optical detection is not yet convincing.

functionality of the sample stick (simultaneous detection of magneto-PL and resonance signal) is clearly demonstrated. The precise effect of resonant excitation of the sublevels on the PL remains largely unclear, and hence a careful selection of samples will be required, but we are confident that the new equipment will provide a unique tool to explore the physics behind the optical response to IR/microwave excitation under strong magnetic fields.

6.4 Conclusions

We have designed, constructed and implemented state-of-the-art equipment for the optical detection of magnetic resonance in pulsed magnetic fields. A fibre-based PL setup together with IR laser excitation was shown to be able to simultaneously record recombination processes and inter-sublevel resonant excitation. The presently installed sample stick will enable unique high field ODMR experiments and therefore provide an excellent tool for spin and Landau level characterisation.

Summary & Outlook

Summary

In the present work we have investigated InAs/GaAs quantum dots (QDs), $Ga_{1-x}In_xN_yAs_{1-y}$ multiple quantum wells (MQWs) and strain-engineered InAs QDs by magneto-photoluminescence (magneto-PL). This is an excellent tool to study the optical and electronic properties of semiconductor nanostructures. In particular, when the quasi-bound particle formed through the Coulomb attraction between an electron and a hole, the exciton, is confined to the nanostructure, the application of a strong magnetic field can overcome the spatial confinement induced by the nanostructure, and the dependence of the exciton recombination energy on magnetic field can provide access to important parameters such as the exciton wave-function extent and effective mass. Information on the excitonic properties is of particular interest for the development of telecommunication lasers that emit at wavelengths of 1.3 and 1.55 μm, where the lowest attenuation in optical fibres occurs. We have therefore studied the exciton confinement in a number of semiconductor heterostructures that are currently considered to be promising approaches in reaching long-wavelength emission.

The implementation of semiconductor lasers in modern technology re-

quires a considerable insensitivity to thermal fluctuations, and hence the occupation of the energy levels of semiconductor nanostructures is ideally temperature (T) independent for $T < 360$ K. However, such ideal behaviour is not observed in practice and hence a thorough understanding of the effect of T is essential for device fabrication. A T-dependent study of the magneto-PL of InAs QDs revealed a clear distinction between two temperature regimes in our samples. For $T < 80$ K, the zero-field PL energy was found to decrease faster than predicted by the empirical Varshni law for the InAs band-gap. This behaviour was previously observed, but our field-dependent measurements showed that this can be attributed to enhanced transfer of carriers via the wetting layer from smaller QDs toward dots which are larger *only* in the growth direction. At higher temperatures ($T > 100$ K) a steep decrease of the PL shift in magnetic field suggests a transition toward increased importance of smaller QDs for the luminescence. The apparent disagreement of this assertion with the decreasing zero-field PL energy is resolved when noting that the PL shift is measured in a very high field, which enhances the QD barrier potentials. Since the influence of a magnetic field on the energy levels of a QD depends inversely on the confinement energy, this mechanism is particularly important for smaller dots, increasing their contribution to the PL signal at high fields and high temperatures.

Dilute nitride MQWs have attracted considerable attention due to the unique property that the incorporation of only a few percent of nitrogen results in a significant reduction of the band-gap energy, making these materials suitable for long-wavelength emission. A disadvantage of the introduction of nitrogen into the semiconductor crystal is the formation of strong carrier localisations and phase separation due to the low miscibility of nitrogen with the other constituent materials. In our study, we have investigated one sample of which the optical properties are deliberately poor, and one sample where optimisations in the growth parameters induce an enhancement of the optical and structural

properties. All our experiments unambiguously confirm the expected improvements, but a T-dependent study of the magneto-PL provides quantitative information on the localisation potentials, which enables a phenomenological description of the potential landscape in both samples.

Emission at long wavelength can also be achieved by growing InAs QDs between confining layers (CLs) whose thickness and composition are carefully controlled. The result is that the strain at the QD-CL interface is relieved, and the QD band discontinuities are reduced, lowering the recombination energy. We have studied three different sets of samples, designed to emit at 1.3, 1.4 and 1.5 μm at room temperature. It is found that the normalised exciton radius, which is the ratio between the measured wave-function extent and the Bohr radius an exciton with the measured mass *would* have in bulk material (*i.e.* in the absence of confinement), decreases when going to longer-wavelength samples, indicating an increased importance of lateral confinement induced by an expanding exciton into a QD with fixed dimensions. However, a reduction of the strain and band discontinuities to reach emission at lower energies is inevitably accompanied by a reduction of the confining potentials, and hence it is clear that at a certain point the QD will no longer be capable of confining the expanding exciton, which is the case for the 1.5 μm sample. Here, a cataclysmic change in the normalised exciton radius and a dramatic sensitivity of the PL signal to magnetic field indicate that the exciton has burst out of its quantum box.

Although magneto-PL is a powerful technique to study exciton confinement in semiconductor nanostructures, additional characterisation is important for the study of these materials. For future resonance experiments, and in the framework of the EuroMagNET project, a new piece of equipment was designed and constructed that allows the optical detection of magnetic resonance in pulsed magnetic fields. The sample stick was developed at the KULeuven and was installed at the Labo-

ratoire National des Champs Magnétiques Pulsés in Toulouse, France. Preliminary results indicate that the system is fully functional, and that it will provide unique access to resonance measurements at very high fields.

Outlook

In the present work we have shown that magneto-PL is a powerful technique to study excitonic properties of semiconductor nanostructures, and that it can be used on a wide variety of systems. The results obtained in this work are promising, and there is room for additional characterisation on some of the systems considered here.

In particular, the magneto-PL on the dilute nitride MQWs showed a dramatic dependence on temperature. The study of the temperature dependent carrier redistributions remains somewhat limited, and it will be interesting to expand the investigation toward higher temperatures and smaller temperature intervals. The challenge of achieving strong luminescence in high magnetic fields could be addressed by performing the experiment at an infrastructure that allows higher DC magnetic fields to be reached, like Lancaster University (17 T) or the High Field Magnet Laboratory in Nijmegen (33 T). A careful analysis of the high-field luminescence as a function of temperature will help to improve the phenomenological model of the potential landscape which was presented in a preliminary form in this work.

We have found that in strain-engineered InAs/InGaAs/GaAs QDs designed to emit at long wavelengths, the exciton eventually escapes from the QD. The exact trend of the normalised exciton radius as a function of electron activation energy will be revealed by studying new samples

that fill the gaps between the current data points. Additionally, theory calculations will help to consolidate the conclusions from the present work. Indeed, preliminary results from 8-band k.p calculations performed by A. Schliwa from the Technische Universität Berlin confirm that the normalised exciton radius decreases with decreasing electron activation energy, driven by an expanding exciton hampered by the spatial limitations of the QD. A precise analysis of the results from an accurate model will undoubtedly provide better insight into the carrier dynamics in these samples.

Finally, the construction and implementation of a state of the art sample stick for ODMR experiments in pulsed fields has opened the path to magnetic resonance experiments on very dilute systems, like semiconductor QDs and QWs, in very high magnetic fields. Although a few improvements of the experimental setup are required to achieve optimal signal quality, the selection of suitable samples to simultaneously study inter-sublevel resonant excitation and exciton recombination will provide unique access to spin and Landau level characterisation, and will widen the research basis for semiconductor nanostructure characterisation.

Nederlandstalige samenvatting

Inleiding

Gestuwd door de groeiende informatisering van onze maatschappij, wordt het belang van een efficiënt en betrouwbaar transport van data steeds belangrijker. Aangezien de absorptie van laserlicht in optische vezels een minimum kent rond golflengtes van 1.3 en 1.55 μm, genieten lasers voor telecommunicatie die licht uitzenden bij die golflengtes de voorkeur. In vrijwel alle lasers die op dit moment instaan voor telecommunicatie wordt gebruik gemaakt van InGaAsP/InP als actief materiaal. Helaas worden deze systemen gekenmerkt door een aantal belangrijke nadelen; het energieverschil voor de conductieband tussen het actief en omliggend materiaal is te klein om een afdoende opsluiting van de ladingsdragers te garanderen, waardoor de kritische drempelstroom-dichtheid[1] heel sterk van de temperatuur afhankelijk is. Daarnaast is het materiaal een slechte temperatuursgeleider, is de electrische geleidbaarheid te laag en bestaat er slechts een klein verschil in brekingsindex tussen de opbouwende lagen, waardoor een optische opsluiting van het gegenereerde laserlicht (de zogenaamde 'cavity') bemoeilijkt wordt. Bovendien zouden struc-

[1] de drempelstroom-dichtheid is de minimale electrische stroomdichtheid benodigd voor het uitzenden van laserlicht door het materiaal.

turen gebaseerd op GaAs substraten in plaats van InP een goedkoper en breder toepasbaar alternatief zijn.

Twee waardevolle benaderingen om, gebaseerd op GaAs substraten, lasing bij lange golflengte te bereiken, zijn (i) de introductie van een kleine hoeveelheid stikstof in het InGaAs materiaal teneinde $In_xGa_{1-x}As_{1-y}N_y$/ GaAs quantum wells (QWs) te fabriceren, en (ii) de metamorfe groei van zelf-geassembleerde InAs/GaAs quantum dot (QD) nanostructuren. Beide technieken zullen in dit werk van naderbij bestudeerd worden. Meer specifiek is het doel van dit werk de verdeling van de ladingsdragers en de opsluiting van het exciton[2] in halfgeleider nanostructuren te onderzoeken. Aangezien temperatuursstabiliteit van het grootste belang is voor toekomstige technologische toepassingen, trachten we een beter inzicht te krijgen in de temperatuursafhankelijkheid van de exciton-eigenschappen.

Experimentele technieken

Voor het onderzoek naar de fundamentele opto-elektronische eigenschappen van de halfgeleider nanostructuren in dit werk werd gebruik gemaakt van fotoluminescentie (FL) in hoge gepulste magneetvelden. De FL-techniek is gebaseerd op het observeren van de recombinatie van een exciton en kan ruwweg in drie stappen worden onderverdeeld: (1) Onder invloed van externe excitatie, bijvoorbeeld door middel van laserlicht, wordt een elektron uit de valentieband van het halfgeleider materiaal ge$\ddot{e}$xciteerd naar de conductieband. Daarbij blijft een positieve ladingsdrager achter in de valentieband (het gat) en door de onderlinge Coulomb-aantrekking kunnen beide ladingsdragers een quasi-gebonden exciton vormen. (2) Door middel van roosterexcitaties kunnen het elektron en het gat zowel energie als impuls overdragen, zodat ze beide naar hun toestand van minimale energie bewegen, respectievelijk het

[2]Een exciton is een quasi-gebonden toestand tussen een negatief geladen (elektron) en een positief geladen (gat) ladingsdrager die onstaat door hun onderlinge Coulomb-aantrekking. Bij de recombinatie van zo'n exciton komt energie vrij die waarneembaar is als luminescentie.

minimum van de conductieband en het maximum van de valentieband. (3) Wanneer het exciton opnieuw recombineert (het elektron neemt opnieuw de plaats van het gat in) wordt het verschil aan energie uitgestuurd onder de vorm van een foton. De detectie en analyse van het aldus uitgestraalde licht levert informatie over de eigenschappen van het halfgeleider systeem.

De metingen werden uitgevoerd in het Pulsveldenlabo van het INPAC-Institute for Nanoscale Physics and Chemistry aan de KULeuven. Het te onderzoeken monster bevindt zich in het centrum van een zelfgemaakte magneetspoel, die verbonden is met de condensatorenbank. Deze 5kV condensatorenbank wordt in een tijdsspanne van ongeveer 20 ms ontladen over de magneetspoel, die is ondergedompeld in vloeibare stikstof om de opwarming ten gevolge van de hoge elektrische stromen te beperken. Tijdens de pulsduur van 20 ms worden magnetische velden tot 50 T gegenereerd, terwijl het geheel van timing en triggering van de overige meetopstellingen door een centraal computersysteem wordt gestuurd. Via optische vezels is het sample gekoppeld aan een excitatielaser en een monochromator en detector voor opname van het signaal. Typisch wordt het gedrag van de FL piek onder invloed van het sterke magneetveld bestudeerd. Onder meer afhankelijk van de grootte van de nanostructuur en het veldregime waarin men zich bevindt, wordt een kwadratische of lineaire verschuiving van de FL piek waargenomen, en de analyse van deze gegevens met behulp van een gedetailleerd model levert waardes voor de exciton-straal en -massa. Wanneer het verkregen signaal te zwak is om in de korte tijdstuur van een magneetpuls te worden onderzocht, wordt gebruik gemaakt van een DC magneetopstelling waarmee velden tot 12 T opgewekt kunnen worden. Hoewel de beperking op de integratietijd bij dergelijke experimenten wegvalt, zijn voor het hoge veld-regime vaak sterkere magneetvelden benodigd, die enkel met behulp van de pulsveldenopstelling toegankelijk zijn.

Temperatuursafhankelijkheid van de fotoluminescentie van zelf-geassembleerde InAs/GaAs quantum dots

Zelf-geassembleerde QDs ontstaan op een natuurlijke manier bij het afwisselend groeien van twee verschillende halfgeleidermaterialen met lichtelijk verschillende roosterconstante, waarbij na de vorming van een dunne 'bevochtigingslaag' driedimensionale eilanden gevormd worden die de opgebouwde spanning helpen te verlichten. Ze zijn een belangrijk concept binnen de halfgeleider nanotechnologie en de temperatuursafhankelijkheid van hun eigenschappen is van het grootste belang voor technologische toepassingen. Een studie van de magneto-FL van InAs/GaAs QDs als functie van de temperatuur (T) wijst op de duidelijke aanwezigheid van twee verschillende T-regimes in onze monsters.

Bij lage T ($T < 80$ K) neemt de FL-energie sneller af dan voorspeld door de empirische Varshni-wet, die de daling van de bandkloofenergie als functie van T beschrijft. Dergelijk gedrag werd eerder al waargenomen, en wordt toegeschreven aan een thermische herverdeling van ladingsdragers van QDs met een hogere energie naar dots met een lagere energie via de bevochtigingslaag. Echter, de verschuiving van de FL-piek tussen 0 en 50 T neemt enkel toe met stijgende temperatuur wanneer het magnetisch veld parallel met de groeirichting van de halfgeleiderstructuur wordt aangelegd. Aangezien de grootte van de magnetische verschuiving van de FL-piek een maat is voor de uitgestrektheid van het exciton in de nanostructuur, betekent dit dat de QDs enkel groter zijn (en dus lagere energietoestanden hebben) in de groeirichting van de structuur, en niet in het vlak van het sample.

In het hoge-T regime ($T > 100$ K) wordt diezelfde FL-piekverschuiving gekenmerkt door een sterke daling, ongeacht de richting van het aangelegde magneetveld, duidend op een verkleining van de exciton golffunctie in de groeirichting *én* in het vlak van het sample. Een daling in de afmetingen van de nanostructuur waarbinnen het exciton is opgeslo-

ten resulteert typisch in een stijging van diens energietoestanden, maar de T-afhankelijke data in de afwezigheid van een magneetveld vertonen juist een daling in de recombinatie-energie bij stijgende temperatuur.

De oplossing voor deze schijnbaar paradoxale vaststellingen schuilt in het feit dat de magneto-FL energieverschuiving bepaald wordt in de aanwezigheid van een sterk magneetveld, waarvan we voorstellen dat het de opsluitingspotentialen binnen de QDs sterk beïnvloedt. Inderdaad, bij de aanleg van een magneetveld zullen de energieniveaus van het halfgeleidermateriaal in het algemeen naar hogere energie verschuiven. Deze verschuiving is constant ($0.9\ \frac{meV}{T}$) voor het omliggende GaAs materiaal maar is, wat de QDs betreft, sterk afhankelijk van de reeds aanwezige opsluiting. Bij relatief kleine QDs met een hoge opsluitingsenergie, is de invloed van een magneetveld veel kleiner ($\sim 0.2\ \frac{meV}{T}$) dan bij grotere dots ($\sim 0.4\ \frac{meV}{T}$) met een lagere opsluitingsenergie. Hierdoor neemt het verschil tussen de energieniveaus van de dots en het omliggende materiaal bij kleine QDs veel sneller toe dan bij grotere QDs. Het resultaat is dat bij hoge magneetvelden en hoge T, de bijdrage van de kleinere QDs (met hogere recombinatie-energie) steeds belangrijker wordt ten opzichte van de grotere QDs (met lagere recombinatie-energie), en de FL-piekverschuiving in hoge magnetische velden op die manier gekarakteriseerd wordt door een daling als functie van de temperatuur.

Strain-gecompenseerde $\mathbf{In_xGa_{1-x}As_{1-y}N_y}$ meervoudige quantum wells

Verdunde nitride meervoudige QWs trekken de laatste tijd veel aandacht vanwege hun unieke eigenschap; de toevoeging van slechts een heel klein percentage stikstof aan het InGaAs materiaal zorgt voor een sterke negatieve bandbuiging, waardoor de bandkloof-energie sterk daalt en deze materialen interessant worden voor de vervaardiging van halfgeleider lasers voor telecommunicatie. Een nadeel van de introductie van stikstof in het halfgeleiderkristal is de vorming van sterke lokalisatiecentra voor de ladingsdragers en een sterk toegenomen fasescheiding

tussen de opbouwende elementen ten gevolge van de slechte mengbaarheid van stikstof met de overige componenten. In dit werk hebben we twee sterk verschillende samples bestudeerd, waarbij het eerste sample moedwillig onder minder ideale condities is gegroeid, en er bij het tweede sample twee belangrijke verbeteringen in de groeicondities zijn doorgedreven. Een kleine hoeveelheid indium in het barrière materiaal zorgt voor roostermatching tussen de QW en het omliggende materiaal, terwijl een groeitemperatuur voor de actieve lagen van 325 °C in plaats van 460 °C de kwaliteit van de nanostructuur ten goede komt.

Alle experimenten bevestigen ondubbelzinnig de beoogde verbeteringen. Een niet-monotone T-afhankelijkheid van de FL-energie in afwezigheid van magneetveld is typisch voor recombinatie vanuit gelokaliseerde toestanden, en wordt waargenomen voor beide monsters. De diepte van het lokaal minimum is echter 50 % groter en vindt plaats op veel hogere temperatuur voor het sample met de minst gunstige groei-omstandigheden. We stellen voor dat het gedrag in afwezigheid van een magneetveld in essentie door de elektronen geregeld wordt, terwijl de magneto-FL in sterkere mate gevoelig is voor de distributie van de gaten. Op lage T nemen we een sterke daling van de excitonstraal als functie van T waar, ten gevolge van een snelle verwijdering van de gaten uit indium-rijke regionen. De metingen van de excitonstraal als functie van T suggereren een sterkere scheiding van elektronen en gaten in het sample van betere kwaliteit, in overeenstemming met resultaten uit transmissie elektronenmicroscopie op vergelijkbare monsters. Op hogere T vinden we eenzelfde asymptotische waarde van 12 nm voor de excitonstraal voor beide samples, hetgeen impliceert dat dit in onze samples de karakteristieke waarde is voor vrije excitonen. Tenslotte zijn we in staat om met behulp van de verschillende gemeten FL-energieën een fenomenologische bespreking van het potentiaal-landschap in onze samples te geven.

Metamorfe groei van InAs quantum dots

Zoals in de inleiding gesteld, kan optische activiteit in het lange golflengtegebied ook bereikt worden door middel van de groei van InAs QDs op een metamorfe tussenlaag. Bij deze strain-engineered QDs worden de dikte en de compositie van de zogenaamde opsluitende lagen waartussen de QDs zich bevinden, zorgvuldig vastgelegd teneinde een bepaalde FL golflengte op kamertemperatuur te bereiken. Wanneer de dikte van de onderste opsluitingslaag aangepast wordt, verandert de residuele spanning in die laag en dus ook de spanning op de QDs, terwijl een verhoging van de concentratie indium in beide opsluitingslagen een verlaging van de band-discontinuïteiten teweegbrengt. Beide aanpassingen verlagen de recombinatie-energie en door nauwkeurige keuze van de beide parameters kunnen optische lagen met emissie op kamertemperatuur op een golflengte naar keuze geconstrueerd worden.

Drie verschillende verzamelingen samples, ontwikkeld voor emissie op 1.3, 1.4 en 1.5 μm werden onderzocht, en voor alle samples werd de genormaliseerde excitonstraal bepaald op lage temperatuur. De genormaliseerde excitonstraal is de verhouding tussen de gemeten uitgestrektheid van de golffunctie en de uitgestrektheid die een exciton met de gemeten massa zou hebben in bulk materiaal, in de afwezigheid van opsluitingseffecten. Een waarde dicht bij één voor de genormaliseerde excitonstraal duidt op weinig invloed van de opsluiting, terwijl een kleine waarde betekent dat het exciton slechts een fractie van de ruimte kan innemen in vergelijking met de niet-begrensde situatie. Op die manier is de genormaliseerde excitonstraal een maat voor de graad van opsluiting aanwezig in de nanostructuur, en deze vertoont een daling wanneer we opschuiven van de samples ontwikkeld voor korte golflengte naar samples voor langere golflengte. Dit betekent dat terwijl de daling in spanning op de QDs en de verlaging van de band-discontinuïteiten een langere golflengte bewerkstelligt, deze ook een uitzetting van het exciton met zich meebrengt, die echter wordt tegengewerkt door de ruimtelijke opsluitingseffecten inherent aan de nanostructuur.

Het is duidelijk dat een verdere uitzetting van de exciton golffunctie in combinatie met een steeds dalende opsluitingskracht onder invloed van de dalende band-discontinuïteiten niet oneindig kan worden verdergezet. Op een gegeven moment moet de uitzettende exciton golffunctie ontsnappen uit een kleiner wordende afgrenzing, en dit is het geval voor het 1.5 μm sample. Hier zijn een enorme verandering in de genormaliseerde excitonstraal en een dramatische gevoeligheid van het FL-signaal voor de aanleg van een magnetisch veld de getuigen van het feit dat het exciton uit de quantum doos is ontsnapt.

Uitrusting voor Optically Detected Magnetic Resonance experimenten

Hoewel in de voorgaande hoofdstukken duidelijk is aangetoond dat magneto-FL een krachtige techniek is voor het bestuderen van exciton opsluiting in halfgeleider nanostructuren, blijft bijkomende karakterisatie steeds belangrijk voor optimaal inzicht in de eigenschappen van deze structuren. Om in de toekomst resonantie-experimenten op dergelijke structuren uit te voeren werd in het kader van het EuroMagNET project een nieuwe meetopstelling ontwikkeld die optische detectie van magnetische resonantie in gepulste magneetvelden mogelijk maakt. De ontwikkeling en assemblage vond plaats in het Pulsveldenlabo van het INPAC-Institute for Nanoscale Physics and Chemistry aan de KULeuven, en de uitrusting werd geïnstalleerd aan het Laboratoire National des Champs Magnétiques Pulsés in Toulouse, Frankrijk. Het belangrijkste onderdeel van de nieuwe sample stick is een conische geleider die zowel het infrarode excitatie-licht als de optische vezels voor de excitatie en registratie van het FL signaal naar het sample brengen. Uit een eerste verzameling test-metingen blijkt dat het systeem volledig operationeel is. Op die manier zal de uitrusting unieke resonantie-experimenten in hoge gepulste magneetvelden mogelijk maken.

Appendix

List of constants and symbols

Constants

Symbol	Name	Value	Unit
e	Electron charge	1.602×10^{-19}	C
h	Planck's constant	4.136×10^{-15}	eVs
$\hbar$	Reduced Planck constant ($h/2\pi$)	6.582×10^{-16}	eVs
m_0	Free electron mass	9.109×10^{-31}	kg
R_y	Rydberg energy	13.6	eV
ε_0	Dielectric constant of free space	8.854×10^{-12}	C^2/Nm^2

Symbols

Symbol	Object	Unit
a_B	Bulk exciton Bohr radius	m
a_B^0	Normalised exciton radius	
B	Magnetic field	T
B_c	Cross-over field	T
d	Confining layer thickness	m
E	Energy	eV
E_A	Electron activation energy	eV
E_B	Exciton binding energy	eV
E_{bo}	Band offset energy	eV
E_{bp}	Barrier potential energy	eV
E_c	Confinement energy	eV
E_{cm}	Centre of mass PL energy	eV
E_g	Band-gap energy	eV
E_M	Conduction band-edge energy	eV
E_N	Nitrogen localised energy level	eV
$E_{n,x}$	n sub-band energy in x-direction	eV
E_+	Upper split sub-band energy	eV
E_-	Lower split sub-band energy	eV
f	Lattice mismatch	
k	Wavenumber	m^{-1}
l_B	Magnetic length	m
l_z	Confinement length	m
m_e^*	Electron effective mass	m_0
S_{eff}	Pick-up coil area	m^2
T	Temperature	K
t_c	Critical confining layer thickness	m
V	Voltage	V
x	Confining layer indium concentration	
z	Crystal growth direction	
ΔE	Energy difference	eV
ε	Dielectric constant	ε_0
μ	Exciton effective mass	m_0
ν	Frequency	Hz
$\langle\rho^2\rangle^{\frac{1}{2}}$	Exciton radius	m
ω_c	Cyclotron frequency	Hz

Bibliography

[1] R. Muis and G.J. Nooren, *Light propagation in optical fibres*, 2000.

[2] H. Temkin, D. Coblentz, R. A. Logan, J. P. van der Ziel, T. Tanbun-Ek, R. D. Yadvish, and A. M. Sergent, *High temperature characteristics of InGaAsP/InP laser structures*, Appl. Phys. Lett. **62** (1993), 2402.

[3] J. S. Harris Jr., *GaInNAs long-wavelength lasers: progress and challenges*, Semicond. Sci. Technol. **17** (2002), 880.

[4] D. Gammon, *Electrons in artificial atoms*, Nature **405** (2000), 899.

[5] M.A. Herman, W. Richter, and H. Sitter, *Epitaxy - Physical Principles and Technical Implementation*, Springer-Verlag, 2003.

[6] J. M. García, D. Granados, J. P. Silveira, and F. Briones, *In segregation effects during quantum dot and quantum ring formation on GaAs(001)*, Microelectronics Journal **35** (2004), 7.

[7] V. Fock, *Bemerkung zur quantelung des harmonischen oszillators im magnetfeld*, Z. Phys. **47** (1928), 446.

[8] C. G. Darwin, *The diamagnetism of the free electron*, Proc. Cambridge Phil. Soc. **27** (1931), 86.

[9] S. Raymond, S. Studenikin, A. Sachrajda, Z. Wasilewski, S. J. Cheng, W. Sheng, P. Hawrylak, A. Babinski, M. Potemski, G. Ortner, and M. Bayer, *Excitonic energy shell structure of self-assembled InGaAs/GaAs quantum dots*, Phys. Rev. Lett. **92** (2004), 187402.

[10] T. Someya, H. Akiyama, and H. Sakaki, *Laterally squeezed excitonic wave function in quantum wires*, Phys. Rev. Lett. **74** (1995), 3664.

[11] S. N. Walck and T. L. Reinecke, *Exciton diamagnetic shift in semiconductor nanostructures*, Phys. Rev. B **57** (1998), 9088.

[12] S. Nomura, L. Samuelson, M.-E. Pistol, K. Uchida, N. Miura, T. Sugano, and Y. Aoyagi, *Landau level formation in semiconductor quantum dots in a high magnetic field*, Appl. Phys. Lett. **71**

(1997), 2316.

[13] K. L. Janssens, F. M. Peeters, and V. A. Schweigert, *Magnetic-field dependence of the exciton energy in a quantum disk*, Phys. Rev. B **63** (2001), 205311.

[14] M. Hayne, J. Maes, S. Bersier, M. Henini, L. Müller-Kirsch, Robert Heitz, D. Bimberg, and V. V. Moshchalkov, *Pulsed magnetic fields as a probe of self-assembled semiconductor nanostructures*, Physica B **346-347** (2004), 421.

[15] R. Provoost, M. Hayne, V. V. Moshchalkov, M. K. Zundel, and K. Eberl, *Magnetophotoluminescence of stacked self-assembled InP quantum dots*, Appl. Phys. Lett. **75** (1999), 799.

[16] J. Vanacken, *The K.U. Leuven pulsed-field facility solid-state physics in high magnetic fields*, Physica B **294-295** (2001), 591.

[17] D. J. Mowbray and M. S. Skolnick, *New physics and devices based on self-assembled semiconductor quantum dots*, J. Phys. D **38** (2005), 2059.

[18] N.N. Ledentsov, V.A. Shchukin, T. Kettler, K. Posilovic, D. Bimberg, L.Ya. Karachinsky, A.Yu. Gladyshev, M.V. Maximov, I.I. Novikov, Yu.M. Shernyakov, A.E. Zhukov, V.M. Ustinov, and A.R. Kovsh, *MBE-grown metamorphic lasers for applications at telecom wavelengths*, J. Cryst. Growth **301-302** (2007), 914.

[19] D. Bimberg, M. Grundmann, and N.N. Ledentsov, *Quantum Dot Heterostructures*, Wiley, London, 1999.

[20] Y. P. Varshni, *Temperature dependence of the energy gap in semiconductors*, Physica (Amsterdam) **34** (1967), 149.

[21] I. Vurgaftman, J. R. Meyer, and L. R. Ram-Mohan, *Band parameters for III-V compound semiconductors and their alloys*, J. of Appl. Phys. **89** (2001), 5815.

[22] L. Brusaferri, S. Sanguinetti, E. Grilli, M. Guzzi, A. Bignazzi, F. Bogani, L. Carraresi, M. Colocci, A. Bosacchi, P. Frigeri, and S. Franchi, *Thermally activated carrier transfer and luminescence*

line shape in self-organized InAs quantum dots, App. Phys. Lett. **69** (1996), 3354.

[23] A. Polimeni, A. Patané, M. Henini, L. Eaves, and P. C. Main, *Temperature dependence of the optical properties of $InAs/Al_yGa_{1-y}As$ self-organized quantum dots*, Phys. Rev. B **59** (1999), 5064.

[24] P. Dawson, E. O. Gbel, K. Pierz, O. Rubel, S. D. Baranovskii, and P. Thomas, *Relaxation and recombination in InAs quantum dots*, Phys. Status Solidi B **244** (2007), 2803.

[25] J. Maes, M. Hayne, M. Henini, F. Pulizzi, A. Patané, L. Eaves, and V.V. Moshchalkov, *Magneto-photoluminescence of stacked self-assembled InAs/GaAs quantum dots*, Physica B **346-347** (2004), 428.

[26] J. Maes, M. Hayne, V. V. Moshchalkov, A. Patane, M. Henini, L. Eaves, and P. C. Main, *Dependence of quantum-dot formation on substrate orientation studied by magnetophotoluminescence*, Appl. Phys. Lett. **81** (2002), 1480.

[27] S. Godefroo, J. Maes, M. Hayne, V. V. Moshchalkov, M. Henini, F. Pulizzi, A. Patane, and L. Eaves, *Magnetophotoluminescence study of the influence of substrate orientation and growth interruption on the electronic properties of InAs/GaAs quantum dots*, J. Appl. Phys. **96** (2004), 2535.

[28] M. Sugisaki, H.-W. Ren, S. V. Nair, K. Nishi, and Y. Masumoto, *External-field effects on the optical spectra of self-assembled InP quantum dots*, Phys. Rev. B **66** (2002), 235309.

[29] Y. Sidor, B. Partoens, F. M. Peeters, N. Schildermans, M. Hayne, V. V. Moshchalkov, A. Rastelli, and O. G. Schmidt, *High-field magnetoexcitons in unstrained $GaAs/Al_xGa_{1-x}As$ quantum dots*, Phys. Rev. B **73** (2006), 155334.

[30] Y. Arakawa and H. Sakaki, *Multidimensional quantum well laser and temperature dependence of its threshold current*, Appl. Phys. Lett. **40** (1982), 939.

[31] T. T. J. M. Berendschot, H. A. J. M. Reinen, H. J. A. Bluyssen,

C. Harder, and H. P. Meier, *Wavelength and threshold current of a quantum well laser in a strong magnetic field*, Appl. Phys. Lett. **54** (1989), 1827.

[32] M. Kondow, K. Uomi, A. Niwa, T. Kitatani, S. Watahiki, and Y. Yazawa, *GaInNAs: A novel material for long-wavelength-range laser diodes with excellent high-temperature performance*, Jpn. J. Appl. Phys. **36** (1996), 1273.

[33] J. Wu, W. Shan, and W. Walukiewicz, *Band anticrossing in highly mismatched III-V semiconductor alloys*, Semicond. Sci. Technol. **17** (2002), 860.

[34] V.M. Ustinov, A.E. Zhukov, A.R. Kovsh, S.S. Mikhrin, N.A. Maleev, B.V. Volovik, Y.G. Musikhin, Y.M. Shernyakov, E.Y. Kondat'eva, M.V. Maximov, A.F. Tsatsul'nikov, N.N. Ledentsov, Z.I. Alferov, J.A. Lott, and D. Bimberg, *Long-wavelength quantum dot lasers on GaAs substrates*, Nanotechnology **11** (2000), 397.

[35] A. Polimeni, M. Capizzi, and A. Frova, *III-N-V alloys: A non conventional material system*, 2004.

[36] W. Shan, W. Walukiewicz, J. W. Ager III, E. E. Haller, J. F. Geisz, D. J. Friedman, J. M. Olson, and Sarah R. Kurtz, *Effect of nitrogen on the band structure of GaInNAs alloys*, J. Appl. Phys. **86** (1999), 2349.

[37] W. Shan, W. Walukiewicz, J. W. Ager, E. E. Haller, J. F. Geisz, D. J. Friedman, J. M. Olson, and S. R. Kurtz, *Band anticrossing in GaInNAs alloys*, Phys. Rev. Lett. **82** (1999), 1221.

[38] J. Wu, W. Shan, W. Walukiewicz, K. M. Yu, J. W. Ager, E. E. Haller, H. P. Xin, and C. W. Tu, *Effect of band anticrossing on the optical transitions in $GaAs_{1-x}N_x/GaAs$ multiple quantum wells*, Phys. Rev. B **64** (2001), 085320.

[39] A. Polimeni, M. Capizzi, M. Geddo, M. Fischer, M. Reinhardt, and A. Forchel, *Effect of nitrogen on the temperature dependence of the energy gap in $In_xGa_{1-x}As_{1-y}N_y/GaAs$ single quantum wells*, Phys. Rev. B **63** (2001), 195320.

[40] S. R. Bank, H. Bae, L. L. Goddard, H. B. Yuen, Wistey M. A., R. Kudrawiec, and J. S. Harris Jr., *Recent progress on 1.55-μm dilute-nitride lasers*, IEEE J. Quantum Electron. **43 (9-10)** (2007), 773.

[41] H. Y. Liu, M. Hopkinson, P. Navaretti, M. Gutierrez, J. S. Ng, and J. P. R. David, *Improving optical properties of 1.55 μm GaInNAs/GaAs multiple quantum wells with Ga(In)NAs barrier and space layer*, Appl. Phys. Lett. **83** (2003), 4951.

[42] A. M. Mintairov, T. H. Kosel, J. L. Merz, P. A. Blagnov, A. S. Vlasov, V. M. Ustinov, and R. E. Cook, *Near-field magneto-photoluminescence spectroscopy of composition fluctuations in InGaAsN*, Phys. Rev. Lett. **87** (2001), 277401.

[43] H. Y. Liu, W. M. Soong, P. Navaretti, M. Hopkinson, and J. P. R. David, *Enhanced optical and structural properties of 1.3 μm GaInNAs/GaAs multiple quantum-well heterostructures with stepped strain-mediating layers*, Appl. Phys. Lett. **86** (2005), 062107.

[44] H. D. Sun, A. H. Clark, H. Y. Liu, M. Hopkinson, S. Calvez, M. D. Dawson, Y. N. Qiu, and J. M. Rorison, *Optical characteristics of 1.55 μm GaInNAs multiple quantum wells*, Appl. Phys. Lett. **85** (2004), 4013.

[45] H. Y. Liu, C. M. Tey, C. Y. Jin, S. L. Liew, P. Navaretti, M. Hopkinson, and A. G. Cullis, *Effects of growth temperature on the structural and optical properties of 1.6 μm GaInNAs/GaAs multiple quantum wells*, Appl. Phys. Lett. **88** (2006), 191907.

[46] N. A. Stolwijk, G. Bsker, T. G. Andersson, and U. Sdervall, *Diffusion of nitrogen in gallium arsenide*, Physica B **340-342** (2003), 367.

[47] M. Herrera, D. González, J. G. Lozano, M. Gutiérrez, H. Y. Liu, R. García, M. Hopkinson, and H. Y. Liu, *An approach to the formation mechanism of the composition fluctuation in GaInNAs quantum wells*, Semicond. Sci. Technol. **20** (2005), 1096.

[48] M. Herrera, D. González, M. Hopkinson, P. Navaretti,

M. Gutiérrez, H. Y. Liu, and R. García, *Influence of growth temperature on the structural and optical quality of GaInNAs/GaAs multi-quantum wells*, Semicond. Sci. Technol. **19** (2004), 813.

[49] E. Tournie, M.-A. Pinault, and A. Guzman, *Mechanisms affecting the photoluminescence spectra of GaInNAs after post-growth annealing*, Appl. Phys. Lett. **80** (2002), 4148.

[50] M. Herrera, D. González, R. García, M. Hopkinson, P. Navaretti, M. Gutiérrez, and H. Y. Liu, *Composition fluctuations in GaInNAs multi-quantum wells*, IEEE Proc.-Optoelectron. **151** (2004), 271.

[51] M. Herrera, D. González, M. Hopkinson, M. Gutiérrez, P. Navaretti, H. Y. Liu, and R. García, *Spinodal decomposition in GaInNAs/GaAs multi-quantum wells*, Phys. Stat. Sol. C **2** (2005), 1292.

[52] M. Herrera, D. González, M. Hopkinson, M. Gutiérrez, P. Navaretti, H. Y. Liu, and R. García, *Composition modulation in GaInNAs quantum wells: Comparison of experiment and theory*, J. Appl. Phys. **97** (2005), 073705.

[53] E. Luna, A. Tampert, E-M. Pavelescu, and M. Pessa, *Nitrogen-enhanced indium segregation in (Ga,In)(N,As)/GaAs multiple quantum wells grown by molecular-beam epitaxy*, New Journal of Physics **9** (2007), 405.

[54] G. Baldassarri Höger von Högersthal, A. Polimeni, F. Masia, M. Bissiri, M. Capizzi, D. Gollub, M. Fischer, and A. Forchel, *Magnetophotoluminescence studies of (InGa)(AsN)/GaAs heterostructures*, Phys. Rev. B **67** (2003), 233304.

[55] A. Polimeni, M. Capizzi, M. Geddo, M. Fischer, M. Reinhardt, and A. Forchel, *Effect of temperature on the optical properties of (InGa)(AsN)/GaAs single quantum wells*, Appl. Phys. Lett. **77** (2000), 2870.

[56] L. Grenouillet, C. Bru-Chevallier, G. Guillot, P. Gilet, P. Duvaut, C. Vannuffel, A. Million, and A. Chenevas-Paule, *Evidence*

of strong carrier localization below 100 K in a GaInNAs/GaAs single quantum well, Appl. Phys. Lett. **76** (2000), 2241.

[57] Yong-Hoon Cho, G. H. Gainer, A. J. Fischer, J. J. Song, S. Keller, U. K. Mishra, and S. P. DenBaars, *S-shaped temperature-dependent emission shift and carrier dynamics in InGaN/GaN multiple quantum wells*, Appl. Phys. Lett. **73** (1998), 1370.

[58] R. Intartaglia, T. Taliercio, P. Valvin, G. Almuneau, P. Lefebvre, T. Guillet, T. Bretagnon, and B. Gil, *Longitudinal-optical phonon broadening due to nitrogen atom incorporation in InGaAsN/GaAs quantum wells*, Phys. Stat. Sol. (c) **2** (2005), 3887.

[59] F. Hatami, N. N. Ledentsov, M. Grundmann, J. Bohrer, F. Heinrichsdorff, M. Beer, D. Bimberg, S. S. Ruvimov, P. Werner, U. Gosele, J. Heydenreich, U. Richter, S. V. Ivanov, B. Ya. Meltser, P. S. Kop'ev, and Zh. I. Alferov, *Radiative recombination in type-II GaSb/GaAs quantum dots*, Appl. Phys. Lett. **67** (1995), 656.

[60] C. E. Pryor and M. E. Pistol, *Band-edge diagrams for strained III-V semiconductor quantum wells, wires, and dots*, Phys. Rev. B **72** (2005), 205311.

[61] Y. Sidor, B. Partoens, F. M. Peeters, J. Maes, M. Hayne, D. Fuster, Y. Gonzalez, L. Gonzalez, and V. V. Moshchalkov, *Exciton confinement in InAs/InP quantum wires and quantum wells in the presence of a magnetic field*, Phys. Rev. B **76** (2007), 195320.

[62] K. Matsuda, S. V. Nair, H. E. Ruda, Y. Sugimoto, T. Saiki, and K. Yamaguchi, *Two-exciton state in GaSb/GaAs type II quantum dots studied using near-field photoluminescence spectroscopy*, Appl. Phys. Lett. **90** (2007), 013101.

[63] Th. Wimbauer, K. Oettinger, Al. L. Efros, B. K. Meyer, and H. Brugger, *Zeeman splitting of the excitonic recombination in $In_xGa_{1-x}As/GaAs$ single quantum wells*, Phys. Rev. B **50** (1994), 8889.

[64] I. J. Fritz, T. J. Drummond, G. C. Osbourn, J. E. Schirber, and E. D. Jones, *Electrical transport of holes in GaAs/InGaAs/GaAs*

single strained quantum wells, Appl. Phys. Lett. **48** (1986), 1678.

[65] A Polimeni, F Masia, G Baldassarri Höger von Högersthal, and M Capizzi, *Magnetophotoluminescence studies of $In_xGa_{1-x}As_{1-y}N_y$: a measurement of the electron effective mass, exciton size, and degree of carrier localization*, J. Phys.: Condens. Matter **16** (2004), S3187.

[66] P. J. Klar, H. Gruning, W. Heimbrodt, J. Koch, F. Hohnsdorf, W. Stolz, P. M. A. Vicente, and J. Camassel, *From N isoelectronic impurities to N-induced bands in the GaN_xAs_{1-x} alloy*, Appl. Phys. Lett. **76** (2000), 3439.

[67] I. A. Buyanova, M. Izadifard, W. M. Chen, A. Polimeni, M. Capizzi, H. P. Xin, and C. W. Tu, *Hydrogen-induced improvements in optical quality of GaNAs alloys*, Appl. Phys. Lett. **82** (2003), 3662.

[68] I. A. Buyanova, W. M. Chen, G. Pozina, J. P. Bergman, B. Monemar, H. P. Xin, and C. W. Tu, *Mechanism for low-temperature photoluminescence in GaNAs/GaAs structures grown by molecular-beam epitaxy*, Appl. Phys. Lett. **75** (1999), 501.

[69] E. D. Jones, A. A. Allerman, S. R. Kurtz, N. A. Modine, K. K. Bajaj, S. W. Tozer, and X. Wei, *Photoluminescence-linewidth-derived reduced exciton mass for $In_yGa_{1-y}As_{1-x}N_x$ alloys*, Phys. Rev. B **62** (2000), 7144.

[70] A. Ait-Ouali, R. Y.-F. Yip, J. L. Brebner, and R. A. Masut, *Strain relaxation and exciton localization effects on the stokes shift in $InAs_xP_{1-x}/InP$ multiple quantum wells*, J. Appl. Phys. **83** (1998), 3153.

[71] Djamel Ouadjaout and Yves Marfaing, *Localized excitons in II-VI semiconductor alloys: Density-of-states model and photoluminescence line-shape analysis*, Phys. Rev. B **41** (1990), 12096.

[72] B. Q. Sun, M. Gal, Q. Gao, H. H. Tan, and C. Jagadish, *On the nature of radiative recombination in GaAsN*, Appl. Phys. Lett. **81** (2002), 4368.

[73] A. Polimeni, F. Masia, A. Vinattieri, G. Baldassarri Höger von Högersthal, and M. Capizzi, *Single carrier localization in $In_xGa_{1-x}As_{1-y}N_y$ investigated by magnetophotoluminescence*, Appl. Phys. Lett. **84** (2004), 2295.

[74] M. Fischer, M. Reinhardt, and A. Forchel, *GaInAsN/GaAs laser diodes operating at 1.52 μm*, Elec. Lett. **36** (2000), 1208.

[75] M. Fischer, D. Gollub, M. Reinhardt, M. Kamp, and A. Forchel, *GaInNAs for GaAs based lasers for the 1.3 to 1.5 μm range*, J. Crys. Growth **251** (2003), 353.

[76] G. Jaschke, R. Averbeck, L. Geelhaar, and H. Riechert, *Low threshold InGaAsN/GaAs lasers beyond 1500 nm*, J. Crys. Growth **278** (2005), 224.

[77] Z. C. Niu, S. Y. Zhang, H. Q. Ni, D. H. Wu, H. Zhao, H. L. Peng, Y. Q. Xu, S. Y. Li, Z. H. He, Z. W. Ren, Q. Han, X. H. Yang, Y. Du, and R. H. Wu, *GaAs-based room-temperature continuous-wave 1.59 μm GaInNAsSb single-quantum-well laser diode grown by molecular-beam epitaxy*, Appl. Phys. Lett. **87** (2005), 231121.

[78] D. Gollub, M. Kamp, A. Forchel, J. Seufert, S.R. Bank, M.A. Wistey, H.B. Yuen, L.L. Goddard, and J.S. Harris Jr., *Continuous-wave operation of GaInNAsSb distributed feedback lasers at 1.5 μm*, Elec. Lett. **40** (2004), 1487.

[79] D. Bisping, S. Höfling, D. Pucicki, M. Fischer, and A. Forchel, *Room-temperature singlemode continuous-wave operation of distributed feedback GaInNAs laser diodes at 1.5 μm*, Elec. Lett. **44** (2008), 737.

[80] Y. Nakata, K. Mukai, M. Sugawara, K. Ohtsubo, H. Ishikawa, and N. Yokoyama, *Molecular beam epitaxial growth of InAs self-assembled quantum dots with light-emission at 1.3 μm*, J. Crys. Growth **208** (2000), 93.

[81] M. J. da Silva, A. A. Quivy, S. Martini, T. E. Lamas, E. C. F. da Silva, and J. R. Leite, *InAs/GaAs quantum dots optically active at 1.5 μm*, Appl. Phys. Lett. **82** (2003), 2646.

[82] L.H. Li, M. Rossetti, G. Patriarche, and A. Fiore, *Growth of InAs bilayer quantum dots for long-wavelength laser emission on GaAs*, J. Cryst. Growth **301-302** (2007), 959.

[83] A. Bosacchi, P. Frigeri, S. Franchi, P. Allegri, and V. Avanzini, *InAs/GaAs self-assembled quantum dots grown by ALMBE and MBE*, J. Cryst. Growth **175-176** (1997), 771.

[84] A. Madhukar, Q. Xie, P. Chen, and A. Konkar, *Nature of strained InAs three-dimensional island formation and distribution on GaAs (100)*, Appl. Phys. Lett. **64** (1994), 2727.

[85] F. Guffarth, R. Heitz, A. Schliwa, O. Stier, N. N. Ledentsov, A. R. Kovsh, V. M. Ustinov, and D. Bimberg, *Strain engineering of self-organized InAs quantum dots*, Phys. Rev. B **64** (2001), 085305.

[86] M. V. Maximov, A. F. Tsatsul'nikov, B. V. Volovik, D. S. Sizov, Yu. M. Shernyakov, I. N. Kaiander, A. E. Zhukov, A. R. Kovsh, S. S. Mikhrin, V. M. Ustinov, Zh. I. Alferov, R. Heitz, V. A. Shchukin, N. N. Ledentsov, D. Bimberg, Yu. G. Musikhin, and W. Neumann, *Tuning quantum dot properties by activated phase separation of an InGa(Al)As alloy grown on InAs stressors*, Phys. Rev. B **62** (2000), 16671.

[87] G. Balakrishnan, S. Huang, T. J. Rotter, A. Stintz, L. R. Dawson, K. J. Malloy, H. Xu, and D. L. Huffaker, *2.0 μm wavelength InAs quantum dashes grown on a GaAs substrate using a metamorphic buffer layer*, Appl. Phys. Lett. **84** (2004), 2058.

[88] Y.-C. Xin, L. G. Vaughn, L. R. Dawson, A. Stintz, Y. Lin, L. F. Lester, and D. L. Huffaker, *InAs quantum-dot GaAs-based lasers grown on AlGaAsSb metamorphic buffers*, J. of Appl. Phys. **94** (2003), 2133.

[89] N. Ohtani K. Akahane, N. Yamamoto, *Long-wavelength light emission from InAs quantum dots covered by GaAsSb grown on GaAs substrates*, Physica E **21** (2004), 295.

[90] H. Y. Liu, Y. Qiu, C. Y. Jin, T. Walther, and A. G. Cullis, *1.55 μm InAs quantum dots grown on a GaAs substrate using a GaAsSb*

metamorphic buffer layer, Appl. Phys. Lett. **92** (2008), 111906.

[91] J. Tatebayashi, M. Nishioka, and Y. Arakawa, *Over 1.5 μm light emission from InAs quantum dots embedded in $In_xGa_{1-x}As$ strain-reducing layer grown by metalorganic chemical vapor deposition*, Appl. Phys. Lett. **78** (2001), 3469.

[92] A.E. Zhukov, A.R. Kovsh, V.M. Ustinov, N.N. Ledentsov, and Zh.I. Alferov, *Long-wavelength lasers based on metamorphic quantum dots*, Microelectronic Eng. **81** (2005), 229.

[93] H. Y. Liu, I. R. Sellers, M. Hopkinson, C. N. Harrison, D. J. Mowbray, and M. S. Skolnick, *Engineering carrier confinement potentials in 1.3-μm InAs/GaAs quantum dots with InAlAs layers: Enhancement of the high-temperature photoluminescence intensity*, Appl. Phys. Lett. **83** (2003), 3716.

[94] L. Seravalli, M. Minelli, P. Frigeri, P. Allegri, V. Avanzini, and S. Franchi, *The effect of strain on tuning of light emission energy of $InAs/In_xGa_{1-x}As$ quantum-dot nanostructures*, Appl. Phys. Lett. **82** (2003), 2341.

[95] L. Seravalli, P. Frigeri, P. Allegri, V. Avanzini, and S. Franchi, *Metamorphic quantum dot nanostructures for long wavelength operation with enhanced emission efficiency*, Mater. Sci Eng. C **27** (2007), 1046.

[96] L. Seravalli, P. Frigeri, M. Minelli, P. Allegri, V. Avanzini, and S. Franchi, *Quantum dot strain engineering for light emission at 1.3, 1.4 and 1.5 μm*, Appl. Phys. Lett. **87** (2005), 063101.

[97] L. Seravalli, P. Frigeri, M. Minelli, S. Franchi, P. Allegri, and V. Avanzini, *Metamorphic self-assembled quantum dot nanostructures*, Mater. Sci Eng. C **26** (2006), 731.

[98] L. Seravalli, M. Minelli, P. Frigeri, S. Franchi, G. Guizzetti, M. Patrini, T. Ciabattoni, and M. Geddo, *Quantum dot strain engineering of $InAs/In_xGa_{1-x}As$ nanostructures*, J. Appl. Phys. **101** (2007), 024313.

[99] M. Geddo, G. Guizzetti, M. Patrini, T. Ciabattoni, L. Seravalli,

P. Frigeri, and S. Franchi, *Metamorphic buffers and optical measurement of residual strain*, Appl. Phys. Lett. **87** (2005), 263120.

[100] P. M. J. Maree, J. C. Barbour, J. F. van der Veen, K. L. Kavanagh, C. W. T. Bulle-Lieuwma, and M. P. A. Viegers, *Generation of misfit dislocations in semiconductors*, J. Appl. Phys. **62** (1987), 4413.

[101] V. Bellani, C. Bocchi, T. Ciabattoni, S. Franchi, P. Frigeri, P. Galinetto, M. Geddo, F. Germini, G. Guizzetti, L. Nasi, M. Patrini, L. Seravalli, and G. Trevesi, *Residual strain measurements in InGaAs metamorphic buffer layers on GaAs*, Eur. Phys. J. B **56** (2007), 217.

[102] F. Briones and A. Ruiz, *Atomic layer molecular beam epitaxy (ALMBE): growth kinetics and applications*, J. Cryst. Growth **111** (1991), 194.

[103] Jean Brossel and Francis Bitter, *A new double resonance method for investigating atomic energy levels. Application to Hg* $^3P_1$, Phys. Rev. **86** (1952), 308.

[104] B. C. Cavenett, *Optically detected magnetic resonance (O.D.M.R.) investigations of recombination process in semiconductors*, Advances in Physics **30** (1981), 475.

[105] Andre Stesmans and Valery V. Afanas'ev, *Characterization of semiconductor heterostructures and nanostructures, edited by Carlo Lamberti*, ch. 13: ESR of interfaces and nanolayers in semiconductor heterostructures, pp. 435–482, Elsevier, 2008.

[106] Matthias Linde, S. J. Uftring, G. D. Watkins, V. Härle, and F. Scholz, *Optical detection of magnetic resonance in electron-irradiated GaN*, Phys. Rev. B **55** (1997), R10177.

[107] H. W. van Kesteren, E. C. Cosman, W. A. J. A. van der Poel, and C. T. Foxon, *Fine structure of excitons in type-II GaAs/AlAs quantum wells*, Phys. Rev. B **41** (1990), 5283.

[108] E. R. Glaser, T. A. Kennedy, K. Doverspike, L. B. Rowland, D. K. Gaskill, J. A. Freitas, M. Asif Khan, D. T. Olson, J. N. Kuz-

nia, and D. K. Wickenden, *Optically detected magnetic resonance of GaN films grown by organometallic chemical-vapor deposition*, Phys. Rev. B **51** (1995), 13326.

List of Publications

1. T. Nuytten, M. Hayne, M. Henini, and V. V. Moshchalkov, *Temperature dependence of the photoluminescence of self-assembled InAs/GaAs quantum dots in pulsed magnetic fields*, Phys. Rev. B **77**, 115348 (2008).

   Selected for publication in Virtual Journal of Nanoscale Science & Technology **17** (14) (2008).

2. T. Nuytten, M. Hayne, M. Henini, and V. V. Moshchalkov, *Temperature dependence of the photoluminescence of self-assembled InAs/GaAs quantum dots studied in high magnetic fields*, Microelectronics Journal **40**, 486 (2009).

3. T. Nuytten, M. Hayne, H. Y. Liu, M. Hopkinson, and V. V. Moshchalkov, *Temperature-dependent carrier distributions in* $Ga_{1-x}In_xN_yAs_{1-y}$ *multiple quantum wells studied by magneto-photoluminescence*, *in preparation.*

4. T. J. Badcock, D. J. Mowbray, E. Nabavi, H. Y. Liu, M. J. Steer, M. Hopkinson, M. Hayne, T. Nuytten, and V. V. Moshchalkov, *Electronic structure of long wavelength (> 1.3* μ *m) GaAsSb-capped InAs quantum dots*, Physics of Semiconductors, AIP Conference Proceedings **893**, 951 (2007).

5. E. Nabavi, T. J. Badcock, T. Nuytten, H. Y. Liu, M. Hopkinson, and D. J. Mowbray, *Magneto-optical study of thermally annealed InAs-InGaAs-GaAs self assembled quantum dots*, J. Appl. Phys., *in press.*

6. M. Ahmad Kamarudin, M. Hayne, Q. D. Zhuang, O. Kolosov, T. Nuytten, V. V. Moshchalkov, and F. Dinelli, *GaSb quantum dot morphology for different growth temperatures and the dissolution effect of the GaAs capping layer*, submitted to J. Cryst. Growth.

7. T. Nuytten, M. Hayne, L. Seravalli, S. Franchi, and V. V. Moshchalkov, *Exciton confinement in strain-engineered InAs/InGaAs/GaAs quantum dots studied in high magnetic fields*, *in preparation.*

Curriculum vitae

Thomas Nuytten
geboren te Kortrijk op 7 april 1982.

1994 - 2000 Algemeen Secundair Onderwijs, Latijn-Wiskunde en Wiskunde-Wetenschappen in Spes Nostra, Kuurne en Sint-Amandscollege Noord, Kortrijk.

2000 - 2004 Studies Licentiaat in de Natuurkunde aan de Katholieke Universiteit Leuven, afgestudeerd met grote onderscheiding.
Licentiaatsthesis: "Magneto-Fotoluminescentie Studie van Zelfopbouwende InAs/GaAs Kwantum Dots als Functie van de Temperatuur", voorbereid in het Laboratorium voor Vaste-Stoffysica en Magnetisme onder leiding van Prof. Dr. V. V. Moshchalkov en Dr. M.Hayne.

2004 - 2009 Doctoraatsonderzoek aan het Institute for Nanoscale Physics and Chemistry (INPAC) van de Katholieke Universiteit Leuven onder leiding van Prof. Dr. V. V. Moshchalkov en Dr. M.Hayne.
Doctoraatsthesis: "Magneto-optical properties of semiconductor nanostructures".